12-15-2021 1:00 PM

Bed particle dispersion and scour in the San Juan (Pacheedaht) River

Meghan Sauro, *The University of Western Ontario*

A thesis submitted in partial fulfillment of the requirements for the Master of Science degree in Geography

Abstract

As part of a larger river restoration project, bed particle dispersion was tracked at pool tailouts where salmon spawning is known to occur in the San Juan (Pacheedaht) River, B.C. Mobility and pathlengths of surface and sub-surface radio-tagged particles was characterized in three reaches over two deployment years in relation to annual channel change, flow magnitude, bar morphology and particle size. Surface particle mobility was high, with results from subsurface tracers indicating high spatial variation of scour at both the reach and local scale. Results also suggest scour can occur up to depths of 0.3m at some locations, even during moderate flood events. Trapping areas of tracer clusters saw consistent annual deposition and can be tied to overall bar development and annual reach-scale channel change. Even during extreme flood events, tracer pathlengths rarely exceeded one riffle-pool-bar unit, further validating the role of channel morphology, along with flow, on particle dispersion.

KEYWORDS: particle tracking, pool tailouts, particle mobility, scour and fill, channel morphology, gravel-bed rivers, wandering rivers, sediment transport, geomorphology

Summary for Lay Audience

Human influences have greatly impaired the ecological health of rivers and has led to a global focus on improving the scientific basis for river restoration, conservation, and management practices. Well-informed decisions on restoration and management plans for a river should include knowledge of the rate at which sediment moves through the river system, also referred to as bedload transport. Bedload transport is of specific importance because it is fundamental to shaping river channels and structuring depositional features (e.g. banks and bars). This can affect flooding risks, in-channel flow velocity and depth, physical habitat, and the river's response to changes in land use and other conditions in the watershed. The goal of this study was to investigate bedload transport processes near salmon spawning habitat through individual particle tracking to better understand the influences of channel morphology, flow, and grain size on particle dispersion. To achieve this, radio-activated tracer stones were deployed along the surface and subsurface (buried) at three study reaches over two deployment years, on the San Juan (Pacheedaht) River, B.C., a large wandering gravel-bed river. In addition, annual change in channel morphology was mapped using aerial imagery. Results show high mobility of surface tracers at known salmon spawning habitat with scour (erosion) at some locations occurring up to, and probably exceeding, 0.3m depths even during years of moderate flood events. Individual pathlength distances of tracer particles rarely exceeded one riffle-pool-bar unit. Areas of high tracer deposition can be linked to bar development and observations of annual channel change. Overall, results indicate that deep scour may be a risk to salmon spawning habitat, as well as implications on the overall stability of banks and bars in relation to flow and sediment supply, providing key information to support ongoing restoration work on the San Juan River.

Acknowledgements

The San Juan River sits on the traditional and ancestral homelands of the Pacheedaht First Nation. I offer my thanks, and acknowledge the Pacheedaht First Nation people, for the opportunity to work and learn on their traditional lands. I would also like to thank the B.C Ministry of Forests, Lands, Natural Resources and Rural Development for their support and funding, that made this project possible. A special thanks to Tom Millard and Neil Goeller, for all the wonderful learning experiences that I was lucky enough to be a part of, out in B.C. To the rest of the San Juan field crew (Ryan McQueen, Jesse Schafer), thank you for all the field assistance, advice, and support, I could not have done it without you!

To my supervisor, Dr. Peter Ashmore, thank you for being such an incredible mentor. I truly appreciate the wisdom and guidance you've shared with me over the past two years. I will forever be inspired by your passion for fluvial geomorphology. To my friends and family, the success of my masters would not have been possible without your kindness and support, and for that I am so grateful. To my B.C hosts, (Rachel, Gareth, Matt, Colleen) thank you, I am so lucky to have been surrounded by such great company for my summer months spent in Nanaimo. To my partner, Carson, thank you for being by my side during this crazy ride, your love and support means the world to me.

Table of Contents

List of Tables

List of Figures

List of Abbreviations

Abbreviation	Definition
DEM	digital elevation model
GPS	Global positioning system
LIDAR	light detection and ranging
PIT	passive integrated transponder
RFID	radio frequency identification
RTK GPS	Real-time kinematic GPS
UAV	unmanned aerial vehicle

List of Symbols

Symbol	Definition	Units
B_m	Median burial depth	m
D_x	grain size (of percentile x)	mm
F_m	fraction of mobile tracers	-
g	acceleration due to gravity	$m\ s^{-2}$
L	pathlength	m
$\bar{L}$	average pathlength	m
L_m	median pathlength	m
p	density of water	$kg\ m^{-3}$
Q	discharge	$m^3\ s^{-1}$
Q_{bf}	bankfull discharge	$m^3\ s^{-1}$
Q_p	peak discharge	$m^3\ s^{-1}$
S	slope	-
Ω_T	total excess energy	$M\ J\ m^{-1}$
Ω_p	peak event excess energy	$M\ J\ m^{-1}$

Preface

This thesis builds on past tracer research (2015-2018) on the San Juan River and is part of a larger scope restoration project led by the San Juan Round Table. Grain-size distributions and tracer fabrication for use in this study were completed in 2015 by the BC Ministry of Forests, Lands, Natural Resource Operations, and Rural Development (FLNRORD) (Ryan McQueen and Tom Millard). Real-time kinematic (RTK) surveying was done by Griffin Fisk, a B.C. Ministry FLNRORD employee. The author did not participate in the October 2020 and 2021 deployment of tracers on the San Juan River because of feasibility reasons, and the specific locations of pool tailout seeding sites were chosen by B.C Ministry of FLNRORD employees (Ryan McQueen, Tom Millard, Jesse Schafer). The author did provide input during meetings prior to actual deployment on the general location of seeding sites at the three study reaches. The author participated in both seasons of tracer recovery that spanned the entire month of July 2020 and 2021. All data collection, interpretation, and analyses were done by the author, unless otherwise stated. All figures were made by the author using R software.

1 Introduction

The San Juan (Pacheedaht) River is a large wandering gravel-bed river on the southwestern coast of Vancouver Island, British Columbia, located on Pacheedaht territory (Pacheedaht First Nation Treaty Information, 2020). A report conducted by Northwest Hydraulic Consultants Ltd. (1994) investigating the impact of forest harvesting on channel morphology in the San Juan River found that an increased sediment supply to the main channel reach during the second half of the 20th century correlated to an increase in the total bar area and an increased channel width over this period. Coincident with these morphologic changes, salmon stocks in the river declined (Burt and Palfrey, 2011). These findings extended through the recent four-year investigation conducted by McQueen et al. (2021), studying individual particle tracking and topographic surveys on the San Juan River with particle displacement patterns reflecting downstream migration and lateral bar accretion. However, there is an identifiable knowledge gap, with little information on particle displacement patterns at different seeding locations, specifically pool tail-outs, which limits current understanding of the link between sediment transport processes, channel change, and physical salmon spawning habitat in large wandering gravel-bed rivers.

Knowledge of bed sediment transport is key to understanding river channel morphology and change; it is the erosion (scour), transfer and deposition (fill) of individual grains of sediment that shape a river channel, including the depositional features (i.e. banks and bars). Importantly, changes in sediment transport regimes can affect morphology, flow distribution, flooding risks, and physical habitat. The travel distance of an individual grain from initial entrainment to final deposition over a specified time period (flood season or flood event) is termed the “pathlength”. Since the transport of bed sediment is the result of the cumulative movement of individual grains, tracking individual particles and examining controls on movement and pathlength distance such as flow and grain size have been used to gain insight on transport processes, improving estimates of bed sediment transport rates and developing theoretical models to explain particle dynamics and a river’s bedload (Ferguson and Wathen, 1998; Haschenburger, 2013). Research has led to the development of functional relationships for both flow strength and grain size on particle dispersion and average pathlength distance, with flow seen as the primary control on particle movement (Vasquez-Tarrio et al., 2019). However, the majority of these studies have been done either in

controlled flume experiments or relatively small rivers and streams, and over short timescales where bar development and the role of channel morphology is less evident.

In a flume channel with alternate bars, Pyrce and Ashmore (2003a) found that individual particle pathlengths coincide with the spacing of bars and that most tracers move from the upstream pool to the next bar downstream and so movement is constrained by, and develops, the bar morphology independent of hydraulic control. Pathlengths tied to the scale of pool-bar morphology has been further verified by flume experiments examining braided channels (Kasprak et al., 2015; Peirce, 2017; Middleton et al., 2019). In a recent meta-analysis, Vasquez-Tarrio et al. (2019) also found that the strength of correlation between stream power (flow strength) and particle pathlengths increase when distances are normalized by the morphological length of the channel, further validating the idea of morphological control. To examine this relationship, McQueen (2019) and McQueen et al. (2021) coupled aerial imagery and particle tracking using RFID technology seeded at the head of gravel bars in the San Juan River, B.C. Results showed that particle pathlengths rarely exceeded one riffle-pool-bar unit, even during years of higher magnitude and longer duration flood events, highlighting strong morphologic control. Furthermore, particle deposition and burial was focused along bar margins at the bend (apex) of the bar which mimicked the larger-scale downstream migration and lateral bar accretion observed from aerial imagery analysis. These results provide further validation for the need to also consider morphologic controls in addition to flow strength and particle size when examining the relationship between particle dispersion and overall channel change in large complex rivers.

The idea that particle seeding locations may be a strong influence on particle pathlength distributions has been examined in flume experiments for braided rivers (Kasprak et al., 2015) but, less is known on particle dispersion at different seeding locations for large wandering rivers in a natural setting. Morphological complexity within a reach site leads to variation in erosional and depositional patterns. Particles seeded at different locations along the longitudinal channel will have unique pathlengths, depending on the morphological characteristics in the area of initial entrainment. Both field and flume experiments have shown that particles seeded at the bar head are mobilized and trapped in the subsequent bar downstream (Pyrce and Ashmore, 2003b; McQueen et al., 2021). However less is known about particles seeded at other sites where distance to the likely depositional site is different, which may influence where particles will become trapped.

Particle seeding locations relative to the immediate downstream depositional area (trap) will influence pathlength distances and may lead to misrepresentative bedload transport rate estimates, especially for non-uniform river channels with complex morphology (McDowell et al., 2021). It is imperative for tracer studies to have particles seeded at varying longitudinal locations to capture the full extent of sediment dynamics.

Understanding particle mobility, and scour and fill near pool-riffle transitions, otherwise known as pool tail-outs, has important ecological implications as these locations are known to be preferred salmon spawning habitat (Baxter and Hauer, 2000; Moir and Pasternack, 2008). During winter high flows, salmon eggs are at risk of being eroded because of the increasing number of particles being mobilized, leading to both increased scour and fill and consequent decreased embryo survival rates. Scour and fill depends on individual particle mobility and the depth of exchange of the active bed layer during flood events, with flow and grain size known to be dominant controls. Both modelling and field studies, primarily using scour chains (Montgomery et al., 1996; Haschenburger, 1999, Lapointe et al., 2000) and wiffle-ball monitors (Rennie and Millar, 2000), have been done to evaluate and predict scour and fill. These studies have led to the current understanding that the depth of the active exchange layer and thus the depth of scour and fill increases with local bed shear stress (flow velocity), and is ~$2D_{90}$ (90^{th} percentile of the coarsest grain size) in gravel-bed rivers. However, these assumptions are based on relatively small streams and rivers with simple morphologies (Haschenburger and Church, 1998; Haschenburger, 1999; Devries, 2002). A recent meta-analysis done by Vasquez-Tario et al. (2021) highlighted the role of morphology on active layer depths, finding that dominant macro-bedforms exert a strong control on the relationship between peak flows and both depths of erosion of the active layer and particle pathlength distances, but empirical field evidence is lacking. Furthermore, in larger, more complex rivers, there may be greater spatial variation in the active layer depth where deep scour is restricted to zones of high velocity in the thalweg (path connecting lowest bed elevation along the channel), although this has yet to be shown in the field. Field studies that examine the spatial pattern and variation in particle mobility and scour and fill processes in large complex gravel-bed rivers are needed to better understand the relationship to channel morphology and the implications for salmon spawning habitat.

Therefore, this thesis is focused on the following objectives related to bed particle motion using the San Juan River as a case study in gravel-bed wandering channel types:

1. Quantify particle mobility and scour depths in the vicinity of salmon spawning habitat (pool tailouts)
2. Observe particle pathlengths at pool tailout seeding sites in relation to bar morphology and development
3. Evaluate the controls of flow, grain size, and morphology on particle dispersion

To satisfy these objectives, data was collected through tracking of buried and surface particles using RFID (Radio Frequency Identification) technology, along with topographic surveys and acquired aerial imagery from LIDAR data, over a two year period. Results of tracer mobility and scour depths at known salmon spawning pool tail-out locations will provide much needed information for ongoing restoration work in the San Juan River, with the overarching goal to improve and restore physical habitat conditions for salmonid species in the river.

2 Background

2.1 Characteristics of Wandering Gravel-bed Rivers

River channel classification systems are not definitive, rather they are used to identify basic differences between spatial patterns (i.e., river patterns, in-channel features, floodplains) and differences in associated fluvial processes and channel pattern development (Kondolf et al., 2016). This is seen in the early classification of river patterns proposed by Leopold and Wolman (1957) identifying a continuum from low-energy meandering to high-energy braiding and citing many factors affecting channel pattern such as grain size, sediment load, riparian vegetation, and channel dimensions (roughness, width, depth). This theory led to the present definition of wandering channels as a transitional type between meandering single-thread reaches and braided morphologies (Church, 1983; Brierley and Hickin, 1991; Buffington and Montgomery, 2013). Knowledge of the processes and underlying factors that control the functioning of wandering river channels is key to understanding and predicting morphologic response to future disturbances, necessary to watershed management and restoration. Furthermore, the morphology of wandering river channels has ecological implications, as it provides diverse physical habitat for many organisms (Buffington et al., 2003). Unfortunately, there is a lack of process-based understanding that highlights the need for empirical field evidence to provide necessary input on the functioning of wandering channel types (Buffington et al., 2013; Hassan et al., 2017).

The three gravel bar reaches of interest in this study are located in the mainstem of the San Juan River which is classified as a wandering, or low-sinuosity, meandering channel (Church and Rice, 2009; Buffington et al., 2013). Wandering channels are irregularly sinuous displaying characteristics of both meandering single-thread channels, and low-sinuosity braided or anabranching channels (Neill, 1973; Church and Jones, 1982; Church, 1983). They have a complex channel planform with long sections diverging from a single identifiable mainstem channel into braiding or splitting around channel islands, with seasonal side-channels also common (Desloges and Church, 1987; Burge, 2005; Church, 2006). Wandering channels are typically characterized by a moderate channel gradient, complex bar development, and display some degree of lateral instability (Desloges and Church, 1987; Buffington et al., 2003). They are distinguished by a pool-riffle-bar macro-bedform unit, with the most common bar morphology being a lateral bar (bar

attached to one bank) with deposition by lateral accretion (Church and Jones, 1982; Desloges and Church, 1987).

Bar development is a key indicator of river behavior, providing information on the active processes and sediment regime dictating channel change at the reach scale, and has been the focus of many studies regarding wandering rivers. This was addressed by Ham (2005) studying wandering reaches of the Fraser River B.C, finding a pattern of regular morphologic development over decades with bed sediment transport occurring as migrating unit bars (gravel sheets) with compensating erodible sediment providing new source material for new unit bars propagating downstream. To further understand bar development, Church and Rice (2009) assessed the morphology and evolution of bars using historic aerial imagery and topographic surveys in the lower Fraser River, B.C., a large wandering gravel-bed river. Findings showed that vertical growth is limited by the height at which the sediment can be elevated, while the lateral growth of bars is limited by the length-scale of the channel, resulting in the latter being the primary control on bar development. Furthermore, Church and Rice (2009) were able to demonstrate that unit bars, similar to braid bars, were built by multiple depositional and erosional events linking sediment transport dynamics to the long-term morphological evolution of bars.

Recently, sediment supply and flood activity were found to be the dominant controls on the morphologic evolution of braided and wandering reaches in a study by East et al. (2017) using 74 years of aerial photographs to analyze four gravel-bed rivers in the Olympic National Park, Washington, USA. Significant channel widening and increased braiding on three of the four rivers studied were strongly linked to high magnitude winter storm activity in recent decades, whereas years with lower peak flows corresponded to narrowing and reduced braiding. They also found that channel changes were associated with changes in sediment supply, leading to aggradation and greater channel width and braiding.

Chapuis et al. (2015) were the first to directly study individual particle displacement and channel change in a large wandering gravel-bed river using particle tracking and topographic surveys. Their results from the Durance River, France, showed particle displacement patterns linked to downstream lateral bar accretion. Although this provided primary evidence of the link between sediment transport processes and long-term morphologic change in large wandering rivers, the

study was limited to a low recurrence interval flood (4-year return period) and had low recovery of tracked particles.

Research on wandering gravel bed rivers has also provided insight on the influence of bed sediment movement on physical habitat at the reach scale. Local variation in sediment transport rates creates transitional areas that are depositional zones and often associated with the formation of bars (lateral, mid-channel, point) and islands (Hanrahan, 2007). These transitional areas, specifically the area between pools and riffles (pool tail-outs) in depositional reaches, are known salmon spawning habitat (Montgomery et al., 1999; Moir et al., 2004; Moir and Pasternack, 2008). Projects on salmon habitat restoration are abundant, including attempts to restore physical processes such as sediment transport regimes and flow (Wohl et al., 2015) although the net benefits are unclear (Harrison et al., 2019). Sediment transport processes, morphologic change, and physical salmon spawning habitat are inherently related, yet there is a lack of field evidence to provide process-based information necessary to watershed restoration and management, especially in large wandering gravel-bed rivers.

2.1.1 The Case of the San Juan River

A report conducted by Northwest Hydraulic Consultants Ltd. (1994) investigating the impact of forest harvesting on channel morphology in the San Juan River, B.C., found that an increased sediment supply to the main channel and tributaries during the second half of the 20th century correlated with an increase in the total bar area and an increased channel width over this period, agreeing with the literature (Church and Rice, 2009; East et al., 2017). Coincident with these morphologic changes, salmon stocks in the river declined (Burt and Palfrey, 2011). These findings extended to the recent four-year investigation conducted by McQueen et al. (2021), studying individual particle tracking and topographic surveys on the San Juan River with particle displacement patterns reflecting downstream migration and lateral bar accretion. However, there is an identifiable knowledge gap, with little information known on particle displacement patterns at different seeding locations, specifically pool tail-outs, which limits current understanding of the link between sediment transport processes, channel change, and physical habitat for species in large wandering gravel-bed rivers.

2.2 Bed Sediment Transport Dynamics

Bed sediment transport is defined as the movement of sediment particles along the river bed in a rolling or saltating mode under the tractive force exerted by flowing water (Hicks and Gomez, 2016). The functional relationship between flow strength and bed sediment transport regimes and a river's transport capacity is well established and commonly used to calculate bed sediment transport rates. Knowledge of bed particle dynamics is necessary to understand and predict the erosional and depositional processes that develop and modify river channel morphology and functioning, important to river engineering and restoration. However, the processes that disperse sediment within a river and the factors that influence sediment supply go beyond flow strength, and involve substantial spatial and temporal variation in bedload transport rates. In large rivers, bed sediment transport can become even more complicated due to elevation and roughness differences associated with complex channel morphology (Hicks and Gomez, 2016; Vericat et al., 2017).

Traditionally, to calculate bedload transport rates for a specific river, short term sediment fluxes at a given cross-section are measured using in-channel samplers or traps, although these measurements are labour intensive and only capture rates at a very limited temporal and spatial scale (Lambert and Walling, 1988). To improve estimations of bedload transport rates, theoretical or semi-empirical predictions are used to calculate a river's transport capacity using mean flow characteristics (typically bed shear stress or stream power) as well as grain size characteristics (Hassan et al, 2013). However, these transport equations represent conditions of uniform flow and relatively uniform grain size characteristics found in smaller streams and rivers. Transport rate measurements have also been calculated from laboratory (Einstein, 1937) and field experiments (Hassan, 1991) using individually marked particles in smaller streams with uniform conditions. For large gravel-bed rivers, characterized by non-uniform grain-size distributions and highly variable flow across and along the channel, that are governed by the river's complex morphology, these equations are inadequate because of the underlying assumption of relatively uniform channel morphology and bed particle size that are representative of small streams and rivers.

Thus, there is a need to theorize bedload transport rates based on characteristics of large gravel-bed rivers taking into account the spatial variation in bed topography, flow and particle size typical of more-complex morphology. This first requires direct observational knowledge of particle

dispersion in relation to larger scale erosional/depositional processes that dictates a river's morphology. Through individual particle tracking, the 'morphological' approach has been developed which is based on the idea that if particle pathlength distances are proportional to the dominant macro bedform (i.e. bar length), with knowledge of the volume of sediment displaced within that unit (virtual velocity), then a rough estimate of transport rates can be made (Neill, 1987; Ashmore and Church, 1998; Milan et al., 2002; Chapuis et al., 2015; Papangelakis and Hassan, 2016; McQueen et al., 2021). This approach captures the spatial variation seen in large rivers with morphologically complex bar development that cannot be observed from bedload trapping or flume experiments using uniform plane-bed flow. Morphological approaches are also usefully tied to the spatial and temporal scale of channel geomorphology and physical habitat, rather than the instantaneous flow conditions of conventional trapping and bedload transport equations. Additional knowledge on particle entrainment and mobility (Hassan et al., 1992) and scour and fill depths (Haschenburger, 1999; Rennie and Millar, 2000) via individual particle tracking has also been used to further understand the relations between particle movement, morphologic change, and active layer depths. However, the morphological method relies on knowledge and prediction of particle dispersal seeded in different morphological units, which currently is supported by limited field evidence (Ashmore and Church, 1998; Mao et al., 2016).

2.3 Particle Mobility

The fraction of particles entrained, or mobilized, during flood events is most often referred to as particle mobility and is a key factor in determining bed sediment transport rates and understanding transport dynamics in gravel bed rivers. Early studies showed that particle mobility is governed mainly by particle mass (diameter) and applied fluid force (shear stress) (Shields, 1936), and such studies have been validated through field and flume studies, with flow and grain size strongly established as primary controls on particle mobility (Hassan et al., 2017; Hassan and Bradley, 2017). Studies suggested size-selective entrainment, with bed sediment only reaching full or 'equal' mobility of all grain size classes during the highest flows, which are at or above bankfull (Ashworth and Ferguson, 1989; Wathen et al., 1995). This led to the idea of partial transport within grain-size classes, where some particles on the bed remain immobile during a transport event, and where a state of full mobility is seen only when all particles of a certain grain size class are mobilized. Partial transport is also defined relative to the bed as a whole and has been documented

in both laboratory and field settings. Pierce et al. (2018) used physical modelling experiments to observe the evolution of mobility across a range of flow velocities and found that mobility increases with discharge and full mobility only occurs when large areas of the bed are active at peak channel-forming discharge. Pierce et al. (2018) also used physical modelling of braided channels to assess the lateral extent of bed material displacement (mobilization) also known as the morphological active width, and found high spatial and temporal variability as a result of complex channel morphology in multi-threaded channels. The results showed an average percent of active width ranging from 6-45% generally increasing with stream power. High spatial and temporal variability of the active width has also been documented for more stable, single-threaded channels (Haschenburger and Wilcock, 2003). Using magnetically tagged stones, Haschenburger and Wilcock (2003) studied partial mobility in a small stream and found that 25-50% of the bed remained in a state of partial mobility during a 2-year return period flood event. Furthermore, during a 7-year return period flood event, surface mobility was near full, indicating the persistence of spatial variation in partial mobility over most flow conditions.

Many field and laboratory studies have examined the relationship of flow variables and particle mobility, beginning with the identification of critical threshold values of entrainment in relation to shear stress (Ashida and Michiue, 1972; Ashworth and Ferguson, 1989; Wong et al., 2007). Individual particle tracking is useful as it can provide an estimate of the discharge at which partial and full mobility begins and the flow conditions at which bedload may occur. Particle mobility from tracer data has been shown to increase with other flow variables such as peak discharge (Haschenburger and Wilcock, 2003; Papangelakis and Hassan, 2016; McQueen et al., 2021) and excess stream power (Hassan et al., 1992, Lenzi, 2004). However, in a recent meta-analysis of tracer data, Vasquez-Tarrio et al. (2019) found large scatter and no clear link between particle mobility and stream power for flow events in riffle-pool channels, suggesting other factors such as flow duration as well as the role of bed texture, and shortcomings of using channel-wide average flow in rivers with complex morphology at the reach scale to analyze mobility in relation to flow conditions.

Complexity arises in the relationship between flow and mobility due to non-uniformity of sediment size mixtures in river beds. It is well established that for a given flow, mobility is similar for smaller particles but quickly decreases with grain size for larger particles, thus the entrainment threshold

for a particle is size dependent (Hassan, 1992; Ferguson and Wathen, 1998). Uncertainty in bed mobility is expected in channels with complex morphology, particularly, in riffle and pool channels and larger rivers, where bar-induced sorting processes (downstream fining of bars) create high-heterogeneity in elevation, roughness, and surface grain size that lead to greater spatial variability in shear stress distributions (Lisle et al., 1991; Wilkinson et al., 2008; Venditti et al., 2012). Using painted particle tracking, Mao et al. (2009) studied mobility in a relatively large gravel-bed river and found that full mobility was frequent in main and secondary channels, however on high topographical bars, partial transport conditions were observed even after the largest monitored flood. In large wandering gravel-bed rivers such as the San Juan River, the overall relationship between event peak discharge, duration and the spatial variability in particle mobility is not yet fully understood. Results from a four-year tracer study on the San Juan River showed that particle mobility at bar heads at three different study reaches was relatively insensitive to increases in total excess flow energy, a commonly used metric that captures both duration and peak discharge measurements (McQueen, 2019; McQueen et al., 2021). Studying particle mobility at different seeding sites within the reach may improve our understanding on the complex relationship between particle mobility, flow, and channel morphology.

2.3.1 Particle Mobility Near Salmon Spawning Habitat

During baseflows, typically in the fall or late summer, salmon utilize areas of the gravel bed, commonly at pool tailouts to bury their eggs prior to winter flooding (Figure 1). Gravel-bed rivers and streams are vulnerable to large winter flood events that can lead to high mobilization of the bed which can directly impact salmon spawning (DeVries, 1997, Harrison et al., 2019). Hydrodynamic modelling has been used to assess the risk of flow during high mobilizing flood events, however the extent of scour is difficult to predict due to the complex spatial variability and interacting factors on flow strength at the local scale. May et al. (2009) studied the viability of salmon spawning areas using modelling and field measurements in a large regulated gravel-bed river and identified a zone of full mobility that was limited to a central core that expanded with increasing flow strength. They concluded that preferred salmon spawning sites were located in areas away from the thalweg (channel centre) and in close proximity to channel margins, so they were less likely to be at risk of mobilization and scour from high flow events. Studying mobility near salmon spawning habitat in a gravel bed mountain stream, McKean and Tonina (2013) also

found little risk to salmon survival with limited particle mobility (<20%) even during bankfull 2-year return period flood events. In contrast, some studies have found that salmon spawning sites are located in zones of highest velocity, near the channel thalweg and thus are potentially at risk of mobilization and scour during high winter flood events (Moir et al., 2002; Hamann et al., 2014; Harrison et al., 2019). Although the current empirical evidence indicates that high bed mobilization from flood events appears to present minimal risk to salmon spawning habitat, little is known about large rivers subject to extreme flood events that can result in substantial bed activity. The San Juan River provides the opportunity to study the risks of particle mobility on spawning viability at known salmon spawning habitat across multiple reaches.

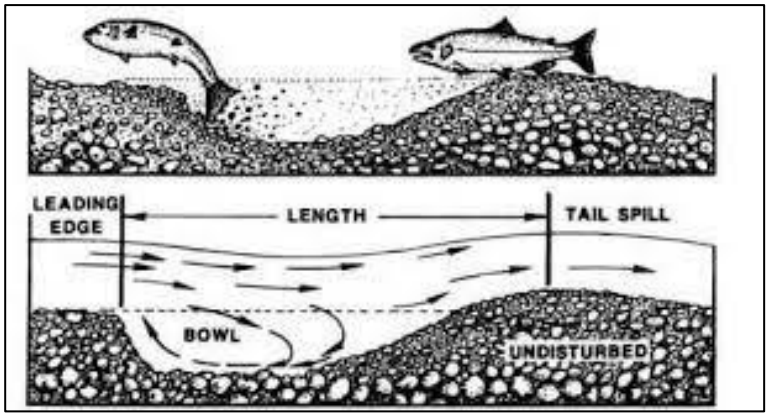

Figure 1. Depiction of salmon spawning at pool tail-out.

Visual depiction of salmon spawning at pool-riffle transitions (also known as pool tailouts), where salmon remove gravel to create a bowl and bury their eggs in pockets (redds) (sourced from Lorenz and Eiler, 1989).

2.4 Particle Pathlengths

Determining pathlengths is fundamental to understanding bedload processes because when combined with the quantity (volume) of material mobilized over a given time period, an estimate of the bedload transport rate can be made (Pyrce and Ashmore, 2003). Particle pathlengths also directly relate to the development of river bed topography through the net erosion and deposition of individually displaced particles which has important implications for both river engineering applications and physical habitat.

Controls on particle pathlengths are similar to that of bed mobility and have been well studied, with power law relationships developed between mean pathlength distance and shear stress (Klosch and Habersack, 2018), peak and cumulative excess stream power (Hassan et al., 1992; Bradley, 2017; Haschenburger, 2013; Schneider et al., 2014) and excess flow expenditure (Haschenburger, 2013; Papangelakis & Hassan, 2016; McQueen et al., 2021). It is also known that particle size influences individual pathlength distances, with larger particles moving shorter distances. However, this relationship is generally weak, unless scaled to the relative size of the bed particles within the mixture of sizes typical of the gravel-bed (Church and Hassan et al., 1992; Ferguson and Wathen, 1998; Schneider et al., 2014). There are large amounts of scatter in the data attributable to the neglect of the possible relationship between individual pathlengths and channel morphology. Most pathlength distributions are positively skewed (e.g. gamma, exponential), with the majority of tracers moving very short distances or not moving at all (Hassan et al., 1991). However these distributions are only representative of low-intensity transport events, which is the dominant transport type seen in small plane bed streams, which are most often represented in the literature (Hassan and Church, 1992). At larger discharges with higher particle mobility, and over longer time scales, individual particle displacement is modulated by the channel morphology and thus will have a different path length frequency distribution, especially in channels with well-developed bars and more complex morphology (Ferguson et al., 2002; Haschenburger, 2013).

The inference of individual pathlengths relating to channel morphology was first developed from the idea that the pathlength is equivalent to the spacing of the principal erosion and deposition sites (Neill, 1971; Ashmore and Church 1998). More specifically, that particle transfer is directly from pool to bar (Neill, 1971). Pyrce and Ashmore (2003a) conducted a re-analysis of the literature which confirmed that positively skewed path lengths were associated with moderate discharge events in smaller more simple channels, and that in bar-dominated channels subject to high magnitude flood events, pathlengths tended to have bi- or multimodal distributions. Flume experiments on an alternate bar channel were also conducted by Pyrce and Ashmore (2003b) and further validated the influence of bar morphology, showing that during high mobilizing flows, tracers were deposited on the first bar downstream from the upstream pool in which tracers were seeded. Building on this foundation, more recent flume experiments have linked individual particle pathlengths to the spacing of erosion and depositional sites, which is directly tied to key bar

development processes in both single thread and braided channels (Pyrce and Ashmore 2005; Kasprak et al., 2015).

More recently, a synthesis and re-analysis of tracer data by Vazquez-Tarrio et al. (2019) studied the influence of both hydraulic and morphologic controls on particle dynamics in a variety of channel types. Importantly, they found that the relatively weak, positive correlation between stream power and average travel distance was corrected, in other words the scatter was reduced, when the travel distance was scaled by a morphological length within each channel type (i.e spacing of macroscale bedforms). Channel bar width has also been an identified predictor of particle pathlength, as it is proportional to the longitudinal spacing of bars, further strengthening the idea that bar spacing exerts significant control in bar-dominated channel types (Beechie, 2001; Vasquez-Tarrio and Batalla, 2019). Identifying the influence of bar-spacing and morphological control on particle displacement contributes to the development of morphological methods for predicting bedload transport rates, however the majority of studies have been on relatively small, simpler rivers and streams such as plane-bed and step-pool channels, where the morphological constraints are less evident.

The San Juan River wandering characteristics, bar-dominant channel reaches and high morphological complexity, allows for a direct case study on the influence of both hydraulic and morphological control on particle displacement in a large river subject to high intensity flow events. McQueen et al. (2021) conducted a four-year tracer study on the river and found that even during years of greater peak flows and longer duration of flow events, the pathlengths of most particles were restricted to one riffle-pool-bar unit. Additionally, the study was able to directly tie particle deposition that focused at bar margins and near the bar apex to overall bar development processes in the river. Although the relationship between particle pathlength dynamics and both hydraulic and morphological control is becoming more clear, additional knowledge gaps need to be filled. Due to the highly variable bed morphology in a complex channel, such as in the San Juan River, discrepancies may exist between transport dynamics seeded at different macro-bedform units (gravel bar vs. pool tail-out) within the same gravel bar reach. Furthermore, examining particle dispersion at three different gravel bar reaches subject to the same high flow events provides for unique insight into the role of channel morphology and contributes to improvements in the morphological methods to estimate bedload transport rates.

2.5 The Active Layer Depth

Vertical sediment mixing in gravel-bed rivers is the exchange of particles between the surface and subsurface through the process of scour and fill during transport events. The active layer, or active layer depth is the limited top-most layer of the riverbed that experiences vertical mixing (Hassan and Bradley, 2017; Vasquez-Tarrio et al., 2021). The active layer depth is an important parameter that controls the estimated bedload flux, coupled with particle pathlength distances, the active channel width, and fraction of the bed entrained (Haschenburger and Church, 1998; Liebault and Laronne, 2008). The extent of the active layer governed by the process of scour and fill is also a major driver for physical habitat distribution and dynamics in gravel-bed rivers (Rice et al., 2012). For these reasons, controls on the active-layer have been well studied with both flow magnitude (Hassan et al., 1992; Haschenburger and Church, 1998; Schneider et al., 2014) and grain size (Wilcock et al., 1996; Haschenburger and Church, 1998; Devries, 2002) being linked to active-layer depths. It is not until recently, that channel morphology has been noted as an important modulating factor when examining active layer depths (Ashmore et al., 2018; Vasquez-Tarrio et al., 2021).

Data from field observations has shown that the active layer depth is relatively thin and heavily controlled by the size of the bed grains, ranging from smaller than the surface layer equal to the D_{90} (90^{th} percentile of grain-size) (Hassan, 1990; Haschenburger, 1999) and typically limited to depths equivalent to 2 times the D_{90} (Haschenburger and Church, 1998; Devries, 2002). There is also compelling evidence that burial depths increase with flow strength correlated to metrics such as discharge (Gottesfield et al., 2004) and peak stream power of the flow event (Mao et al., 2016), although some studies have found no relationship to flow parameters (DeVries 2002; Papangelakis and Hassan, 2016). The uncertainty in the current literature may in part be due to the lack of consideration of channel morphology.

Most empirical evidence on active layer depths has been collected in small plane bed streams with uniform bed texture and lack any influence from macro-bedforms and complex morphological features. Particle entrainment is known to be spatially variable, with variability in cross-sectional shear stress distributions that can influence the spatial and vertical extent of the active layer depth (Habersack et al., 2008). Furthermore, macro-bedforms (i.e riffle, pools, bars) can influence the spatial distribution of particle entrainment as well as the cross-sectional extent of mobile sediment

patches in morphologically-complex channels, such as single-thread wandering or multi-thread braided channels (Vasquez-Tarrio et al., 2021). This suggests that the current knowledge of active layer dynamics, may not hold true for larger rivers with high morphological complexity. The idea that morphology may play a more dominant role in larger rivers motivated the term 'morphological active layer' which describes the bed sediment layer mobilized during transport events related to large-scale channel forming processes such as channel avulsion, bend and confluence scour, bar migration and overall channel pattern reconfiguration (Leduc et al., 2015). In theory, particles that make up the active layer are responsible for these morphological processes over longer time-scales and thus should in turn be in some way controlled by the maximum vertical extent of the macroform features in the channel.

In a recent meta-analysis by Vasquez-Tarrio et al. (2021), they found that dominant channel macroforms modulated the relationship between flow strength and active-layer depths, with major differences between different channel morphology types, which suggests a morphological influence on active layer depths. Burial data from the four-year tracer study on the San Juan River by McQueen et al. (2021) support the findings of Vasquez-Tarrio et al. (2021), with tracer burial being tied to patterns of bar-scale topographic change. Importantly, McQueen et al. (2021) also found that active layer depths from tracer burial data exceed the maximum grain exchange depth of $2D_{90}$ that is suggested throughout the literature and commonly used in bedload transport modelling.

With increasing capabilities of tracer data collection in large rivers from advancements in technology, empirical evidence of the processes of scour and fill and active layer depths in relation to channel morphology is needed. In the case of the San Juan River, and for many other rivers around the world, scour and fill also has direct implications on the quality of physical salmonid spawning habitat and is a major constraint when considering factors involved in large-scale river restoration programs.

2.5.1 Scour Implications at Salmon Spawning Habitat

During low flows, typically in the fall or late summer, salmon utilize areas of the gravel-bed for spawning, commonly at pool tail-outs, to bury their eggs prior to winter flooding (Figure 1). High flows producing bed mobilizing events may lead to scour depths of the bed beyond the depths of

egg burial, putting salmon populations at risk (Montgomery et al., 1996). Devries (1997) conducted a comprehensive review of egg burial depth data which included primary egg burial depth criterion on the five Pacific salmonid species found in the San Juan River. Results suggest egg burial depths for these species may range from 10 – 50cm below the streambed surface, however high variability due to a number of factors such as sampling methods, and spawning behaviour, was identified as a limitation to the data.

Scour chain monitors have been a common technique to study scour depths near salmonid spawning sites in many streams and rivers (Rennie and Millar, 2000; May et al., 2009; Dusterhoff et al., 2017; Meredith et al., 2018). The cross-sectional and longitudinal spatio-temporal variability of scour depths attributable to entrainment potential and shear stress values has been well studied in the literature (Rennie and Millar, 2000; May et al., 2009; Meredith et al., 2018) with some areas of the channel experiencing no bed activity, while other areas undergo maximum scour depths that can extend to values as high as 8 times the surface layer (Haschenburger, 1999).

At the local scale, Rennie and Millar (2000) found no spatial autocorrelation in scour depths at closely spaced (~1m) scour chains in a small gravel-bed creek in B.C, which they attributed to variable bed roughness and topography. Interestingly, at the same magnitude of shear stress, Meredith et al. (2018) measured 4cm differences in scour depths along a longitudinal gradient in a mountain river in Utah, U.S.A. In a recent study, Dusterhoff et al. (2017) found that maximum scour depths in salmonid spawning habitat was negatively correlated with flow shear stress and potentially more controlled by coarse particle exposure to flow. Furthermore, many studies have shown that scour depths can vary even during years of similar peak flow events, from the influence of flood duration (Shellberg et al., 2010; Meredith et al., 2018). The vast majority of these studies have not found substantial scour depths in areas of salmon spawning habitat, at channel margins where much shallower scour depths occur compared to channel centreline (thalweg) depths (Montgomery et al., 1996; Rennie and Millar, 2000; May et al., 2009; Meredith et al., 2018) however, scour depths in large rivers with complex cross-sectional morphology has not been well-studied.

The role of morphology and bed texture has been largely responsible for the difficulty in predicting scour and fill processes, even at an extremely localized scale (Cienciala and Hassan, 2013). There is an evident gap of empirical evidence on scour depths for large salmon-rearing rivers that are

subject to intense winter flood events, that overlap with incubating salmonid eggs buried in the subsurface, with the potential of entire cross-sections to be at risk of deep scour. Moreover, the complex relationship between channel morphology, and salmon spawning habitat, indicates a need for further understanding of the contributing factors on the processes of scour and fill in large gravel-bed rivers. The utilization of tracer particles at varying burial depths coupled with surface tracer deployment at highly-mobilized pool-tailout areas in the San Juan River can provide empirical insight on the role of bed morphology in relation to bed mobility and scour.

2.6 Particle Tracking Techniques

Earlier tracer studies used a variety of techniques including painted and magnetic particles. Recent technological advances have led to the use of passive integrated transponders (PIT tags) that track individual particles by radio frequency identification (RFID) technology using radio antennas and has shown promising results for applications in large gravel-bed rivers (Nichols, 2004; Lamarre et al., 2005; Schneider et al., 2010; Bradley and Tucker, 2012; Phillips et al., 2013). PIT tag technology is relatively inexpensive, resistant to breakage, and long-lasting, with studies generating high recovery rates in streams (78%-100%) (Macvicar and Roy, 2011; Biron et al., 2012; Milan et al., 2013) capturing sediment dynamics over multiple years and travel distances on the scale of 10^2, even 10^3m depending on search capacity. Furthermore, the small size of the PIT tag allows for a larger range of grain size classes to be studied leading to an improved understanding of sediment dispersion in gravel-bed rivers (Hassan and Roy, 2016).

PIT tag technology, when coupled with other bedload monitoring techniques, has seen increasing use in larger, more complex rivers (channel width > 80m), although limitations still exist. Rollet et al. (2008) first tested the use of PIT tags in the Ain River, a large wandering gravel-bed river in France, and saw a recovery rate of 36%, finding that shallow detection ranges (up to 25cm) limited recovery in areas of deep burial as well as deep pools. Chapuis et al. (2015) and Arnaud et al. (2017) also noted the shallow detection range of PIT tags as a key limitation to their recovery rates (40% in the Durance River, France; 11-43% in the Old Rhine River, Switzerland, respectively). However, developments in PIT tag technology continue. Chapuis et al. (2014) studied the effects of tag orientation on detection ranges and found optimal detection using vertical cylinder tags, which motivated the design of artificial “wobblestones” (Papangelakis et al., 2019) that automatically orient the tag in the optimal orientation for detection. Technological improvements

have also led to increased read ranges of antenna devices (Arnaud et al., 2015; McQueen et al., 2020). McQueen et al. (2021) used an innovative “mega-antenna” that resulted in recovery rates exceeding 65% which is a considerable improvement when compared to tracer searching in similar large gravel-bed rivers such as Chapuis et al. (2015). Low recovery in large gravel-bed rivers supports the need to develop and test alternative recovery strategies to improve the validity of tracking studies and our overall understanding of particle dynamics in large, complex river systems.

Improved detection ranges of RFID technology has also been used advantageously to better understand the depth of exchange of the bed active layer during flood events, also known as the active layer depth. Primarily, scour chains developed by (Leopold et al., 1966) are used to monitor scour and fill depths providing knowledge on active layer depths (Haschenburger, 1999, Lapointe, 2000; Montgomery et al., 1996), however harsh conditions and large flood events can remove scour chains or bury them making recovery and relocation difficult. Papanicolaou et al. (2014) adapted conventional scour chains with passive RFID tags to monitor bridge scour but this method requires a fixed antenna with continuous power, thus not transferable for monitoring the active layer in the natural environment and over a large area of river-bed. Recently, Brousse et al. (2018) developed a new active RFID scour chain device used in two braided mountain streams which was proven to be successful for the measurement of active-layer depths, although this device is limited to the use of large particles (b-axis >70mm). To the author’s knowledge, no other studies have been done using buried RFID tracer methods to assess the controls on the active layer depth in large, complex, gravel bed rivers subject to large flood events, leading to a need for further work on the potential use of RFID tracers for scour and fill monitoring.

2.7 Research Rationale

Understanding the factors that drive the governing processes behind sediment transport in gravel-bed rivers is important knowledge to better inform modelling and accurately predict bedload transport rates. Studying sediment transport at the individual grain-scale has provided useful insight over the past few decades, with grain size and flow being cited as primary controls of both particle mobility, pathlength distances, and scour and fill processes (Hassan and Bradley, 2017; Vasquez-Tarrio, 2019). However, the majority of theories and empirical-based evidence from field and flume experiments have been derived from small, simple streams and rivers.

Importantly, large wandering rivers have complex channel morphology with bar development being a key erosional and depositional process that is governed by individual particle movement (Ham, 2005; Church and Rice, 2009). Therefore, it is reasonable to suggest that the role of channel morphology may be more significant, however this has not been well studied. Flume experiments have shown that even during high-magnitude flood events, channel morphology is the primary control on particle pathlengths in bar-dominated rivers (Pyrce and Ashmore, 2003a), although field evidence to support the theory is lacking. Coupling topographic change and tracer data has led to direct observations of individual particle displacements tied to bar development in a large wandering gravel bed river, with tracers seeded at bar heads depositing at the nearest downstream depositional area (i.e. gravel bar) (Chapuis et al. 2015; McQueen et al., 2021). Using burial data and topographic change, McQueen et al. (2021) also found compelling evidence to suggest the maximum grain exchange depth of twice the D_{90} may not hold true in larger rivers.

Although knowledge on sediment dynamics in large complex rivers has improved, gaps still exist. Little is known on particles seeded at varying locations at the reach scale. Particle seeding locations in large wandering rivers can influence entrainment due to variable bed morphology, grain size, and flow within the reach and even within the dominant macro-bedform (riffle-pool-bar) (McDowell et al., 2021). This variation also creates transitional areas, known as pool-riffle transitions, or pool tailouts, an important morphologic feature as they are preferred salmon spawning habitat (Montgomery et al., 1999; Hanrahan, 2007; Moir and Pasternack, 2008). Studying sediment dynamics, particularly particle mobility and scour and fill processes, at pool tailouts can add insight to bedload transport rates as well as identify the risk of scour to salmon egg burial.

Scour chains have been used to assess scour risks near salmon spawning locations in small streams (Montgomery et al., 1996; Rennie and Millar, 2000; Dusterhoff et al., 2017; Meredith et al., 2018) and rivers (May et al., 2009). Results from these studies suggest non-uniform lateral (cross-sectional) distributions of scour, with the greatest extent near the channel centre, away from channel margins where spawning commonly occurs. However, the spatial extent of scour has rarely been assessed in large rivers that are subject to extreme winter flood events. Furthermore, the complex cross-sectional bed morphology may play a large role in scour distributions, although this currently lacks empirical evidence.

The objective of this study is to examine individual particle dispersion, with a focus on determining the key factors that influence particle mobility and scour depths in a large wandering gravel-bed river near salmon spawning locations. Specifically, this study aims to address the role of channel morphology, in conjunction with grain size and flow, on overall pathlength characteristics, particle mobility, and scour, using data from deployed surface and buried tracers. To meet these objectives, PIT-tagged tracer stones were deployed on the surface and subsurface at pool tail-out locations at three study reaches in the San Juan River, B.C for two winter flooding seasons (Oct-July). Data from a previous four-year tracer study on the San Juan River will also be used to compare sediment transport dynamics at differing seeding locations and characterize the influences of flow, grain size, and morphology over a longer temporal scale.

Therefore, this thesis is focused on the following objectives related to bed particle motion in San Juan River as a case study in gravel-bed wandering channel types:

1. Quantify surface and subsurface particle mobility and scour and fill processes in the vicinity of salmon spawning habitat (pool tailouts)
2. Observe and identify pathlength characteristics of particles seeded at pool tailout locations in relation to reach-scale morphology and bar development
3. Compare and contrast pathlength dispersion between surface and subsurface particles
4. Evaluate the controls of flow, grain size, and morphology on particle dispersion

3 Study Area

3.1 The San Juan River

The San Juan River is a large wandering gravel-bed river located on southern Vancouver Island with a drainage area of ~730km^2 and an approximate bankfull discharge (Q_{bf}) = 650m^3 s^{-1}. The river flows westward, ends in an estuary and drains to the Pacific Ocean at Port San Juan on the Juan de Fuca Strait (Figure 2). The rivers native name is Pacheedaht, translating to "*Children of the Sea Foam"* and is situated on Pacheedaht territory (Pacheedaht First Nations Treaty Information, 2020). The San Juan River mainstem is ~50km long, the upper river is constrained by a narrow valley that widens with the final 16km in a wide alluvial valley (Northwest Hydraulic Consultants Ltd., 1994).

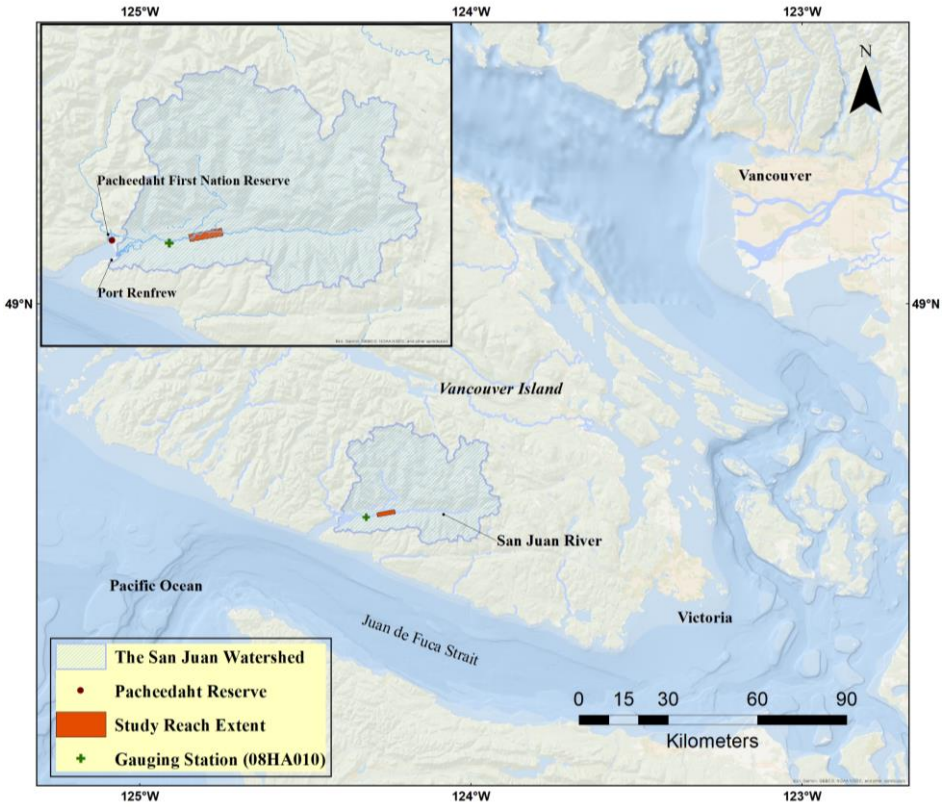

Figure 2. Depiction of the San Juan watershed area.

3.1.1 Climate and Hydrology

The San Juan watershed is actively logged with roughly 98% of the San Juan Watershed managed for forest harvest, with ~25% of the total watershed area cut between ~ 1950-1990s (NHC, 1994). The Watershed experiences a maritime or coastal climate, situated in the Coastal Western Hemlock Zone (CWH), the wettest biogeoclimatic zone, on average, in British Columbia (Moore et al., 2010). Climate data is taken from the nearby Port Renfrew station (1016335), located at the mouth of the river (48°35'30''N, 124°19'35''W) (Table 1) (ECCC, 2021). Total annual precipitation is rainfall-dominated with only 1% as snowfall. Nearly the full extent of precipitation is rainfall at the valley bottom, but there is some snowfall at higher elevation in the interior watershed. Normal (1981-2010) annual precipitation is ~ 3505mm (Table 1) (ECCC, 2021). The west-facing coastal valley is subject to mid-latitude cyclonic storms that span from October until March. In consequence, this winter storm season experiences on average ~78% of total annual precipitation (Table 1); features of these rainstorm events include their prolonged duration and high amounts of total precipitation (NHC, 1994). In consequence, the majority of precipitation in the watershed occur during this time period, with November being the wettest month (579.7mm) and July the driest (50.5mm) (Table 1) (ECCC, 2021). Normal (1981-2010) annual average temperature is 9.3°C, with the warmest daily temperature on average occurring in the month of August (15.6°C) and the coldest in December (3.8°C) (Table 1) (ECCC, 2021).

Table 1. Climate normals extracted from the Port Renfrew climate station data (1016335) (ECCC, 2021).

	Jan	Feb	March	April	May	June	July	Aug	Sept	Oct	Nov	Dec	Annual
Daily Average Temperature (°C)	4.1	4.6	6.2	8.4	11.1	13.4	15.3	15.6	13.4	9.6	6.1	3.8	9.3
Precipitation (mm)	555.7	376.6	362.3	258.7	154.7	107.9	50.5	82.4	123.9	371.2	579.7	481	3504.6

The Water Survey of Canada (WSC) has operated the 'San Juan River Port Renfrew' hydrometric gauging station (08HA010) located ~2km downstream of Bar 15 near the mouth of the river at Port Renfrew since 1959 (4834'38''N, 12419'02''W) (Figure 3.1) (Water Survey of Canada, 2021). Water level data is collected by the station at five minute intervals, discharge data is then calculated

by using a stage-discharge model (Water Survey of Canada, 2021). The San Juan River experiences highest flows, and thus most extreme bedload movement and morphological change, during the fall and winter flooding periods, attributable to the monthly trends in precipitation from storms. On average, highest flows occur in January with an average daily discharge of $99.7 m^3 s^{-1}$ and drops to an average of $4.5 m^3 s^{-1}$ in August which experiences the lowest flow levels for the historical record (1960-2020) (Figure 3; Figure 4).

During the 2019-2020 deployment year, the largest flood ever recorded on the San Juan occurred from January 31st - February 1st 2020 with maximum peak discharge (Q_p) reaching ~$1360 m^3\ s^{-1}$ and a return period of ~100 years. Maximum peak discharge (Q_p) above $1000 m^3\ s^{-1}$ has only been exceeded nine times since 1959, prior to this flood (Figure 3; Figure 4). This flood was supplemented by two other events (early and mid-January) during the period of study that reached discharge levels near bankfull (Figure 3). Overall, seasonal flows for the study period align with annual historical flow trends, with January having an abnormal mean discharge of $170.8 m^3\ s^{-1}$ influenced by the three flood events while August had a typical mean discharge of $4.5 m^3\ s^{-1}$.

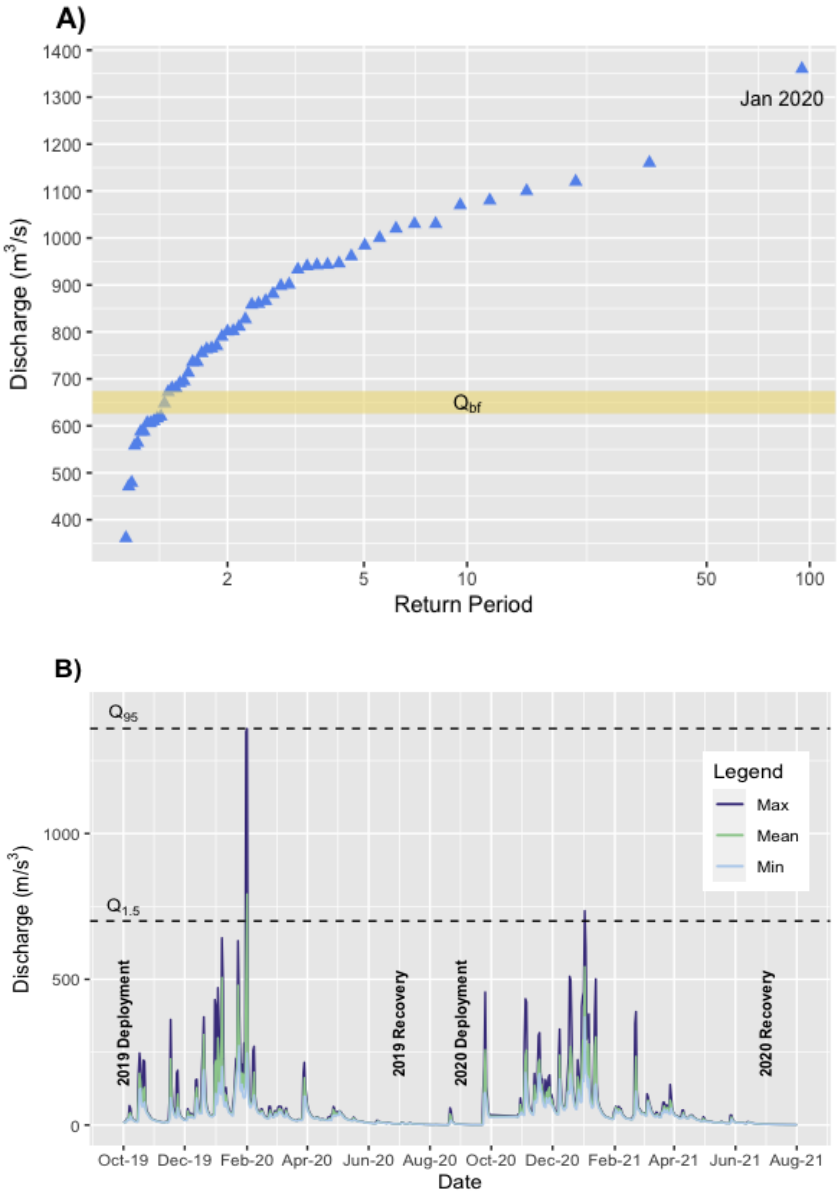

Figure 3. A) Flood frequency plot. B) San Juan River hydrograph for the two year study period.

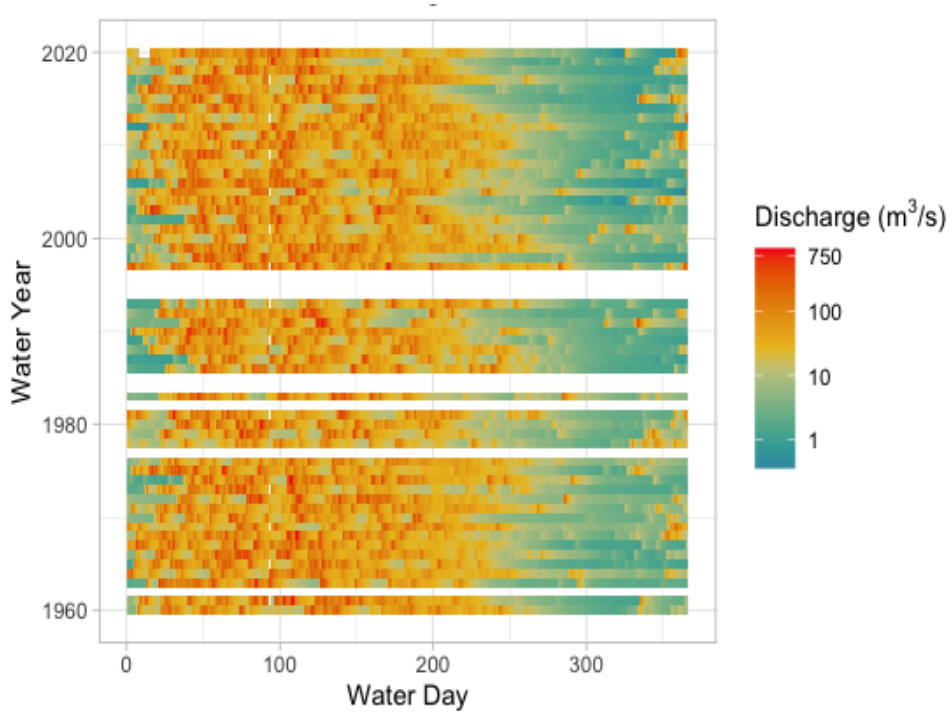

Figure 4. Discharge 'heat' map.

Discharge 'heat' map of historical mean daily discharge levels for the San Juan River (1960-2020).Gaps represent missing data due to gauging station malfunction (Water Survey of Canada, 2021). Water day '0' represents October 1st.

3.1.2 Study Reach Characteristics

The study reach is in the mainstem of the San Juan River which is characterized as an alluvial channel with both the bed and banks composed of erodible material deposited by the river with the exception of a few locations that have exposed bedrock outcrops. The mainstem is classified as an active wandering channel displaying characteristics of a low sinuosity single thread channel with occasional mid-channel bars (Church, 1983). There are frequent, regularly spaced gravel point bars, which are growing laterally in the downstream direction and are associated with erosion and retreat of the outer bank in bends (Figure 5) (McQueen, 2019). This is consistent with known lateral instability and overall channel widening since 1995, linked to an increased sediment supply from a surge in landslide occurrences due to logging activity in the watershed in the latter half of the twentieth century (NHC Ltd, 1994).

Figure 5. Erosion of the left bank at the Bar 6 study reach.

Erosion of the left bank (looking downstream) at the Bar 6 study reach, near the tracer deployment location (July 2020).

Consequently, stocks of all five salmonid species in the river declined, including Pink salmon (*Oncorhynchus gorbuscha*), Chinook Salmon (*Oncorhynchus tshawytscha*), Coho salmon (*Oncorhynchus kisutch)*, Chum salmon (*Oncorhynchus keta)*, and Sockeye salmon (*Oncorhynchus nerka)* (Burt and Palfrey, 2011). In response to these findings, the San Juan Stewardship Roundtable (composed of stakeholders and rightsholders in the watershed including provincial and federal government, First Nations, and industry) began restoration efforts in the watershed to re-establish past river conditions and revitalize salmonid habitat, which includes recent vegetation plantings of willows from 2015-2017 (NHC Ltd, 1994).

At present, only Chinook, Coho, and Chum occur as major runs in the San Juan watershed and therefore are the focus of restoration work on the San Juan River (Burt and Palfrey, 2011). With annual salmon escapement estimates as high as 7,000, 3,500, and 6,000 in the 1950s, for Coho, Chinook, and Chum, respectively (Burt and Palfrey, 2011). The most recent escapement estimates (2010) are 1,000, and ~100 for Coho and Chum, respectively, with no observations of Chinook escapements (Burt and Palfrey, 2011). Salmon spawning occurs at baseflows in the fall, but vary between species (Table 2). Unfortunately, egg burial depths for spawning salmonid species in the

San Juan River is unknown. Although, they can assumed to be similar to egg burial depths of Pacific salmonid species in other rivers, ranging from 10cm – 50cm (Devries, 1997).

Table 2. Spawning Times for Chinook, Coho, and Chum salmon in the San Juan Watershed (Burt and Palfrey, 2011).

Common Name	Scientific Name	Peak Spawning Time
Chinook Salmon	*Oncorhynchus tshawytscha*	Late September - Early October
Coho Salmon	*Oncorhynchus kisutch*	Late August – Late September
Chum Salmon	*Oncorhynchus keta*	Late August – Late October

The active channel width (portion of the channel actively altered by floods) varies between 50-150m, with a reach-averaged slope of 0.0011 in the mainstem with local variation (Figure 6). The mainstem and study reach is composed of riffle-pool sequences associated with large gravel point bars (Figure 7). Bars are a major storage site of sediment and are composed of gravel pebbles, cobble, and sand. Pools are topographically low and slow-moving with riffles at higher elevation and fast-flowing water; the transitions between pools and riffles are known as pool-tailouts and are a common location of salmonid spawning habitat (Figure 7; Figure 8) (Hogan and Luzi, 2010).

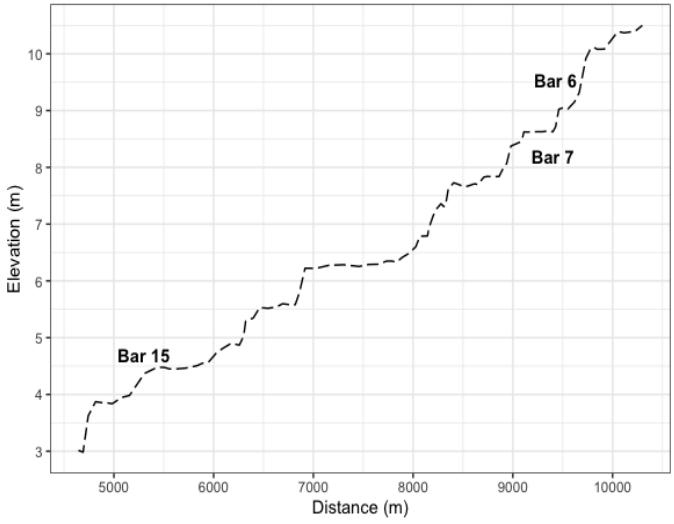

Figure 6. Elevation profile of the mainstem of the San Juan River. Elevation data collected and provided by Tom Millard (B.C. Ministry).

The three gravel bar study reaches are located in the lower alluvial reach (Bar 6, Bar 7, Bar 15) (Figure 7). There is a pre-existing numbering system for gravel bars in the lower San Juan that follows a downstream sequence, with Bar 6 being farthest upstream and Bar 15 ~3km downstream of Bar 6 and 7 (Figure 7). The study reach includes three individual riffle-pool-bar sequences (Figure 7). These three gravel bar sites were chosen as they are of particular interest to the San Juan River Roundtable, being identified as known salmonid spawning locations by local Pacheedaht biologists with previous restoration work being done on the bars as well through the planting of willows. They are also the location of previous particle tracking work, which provides additional background information on the river (McQueen, 2019).

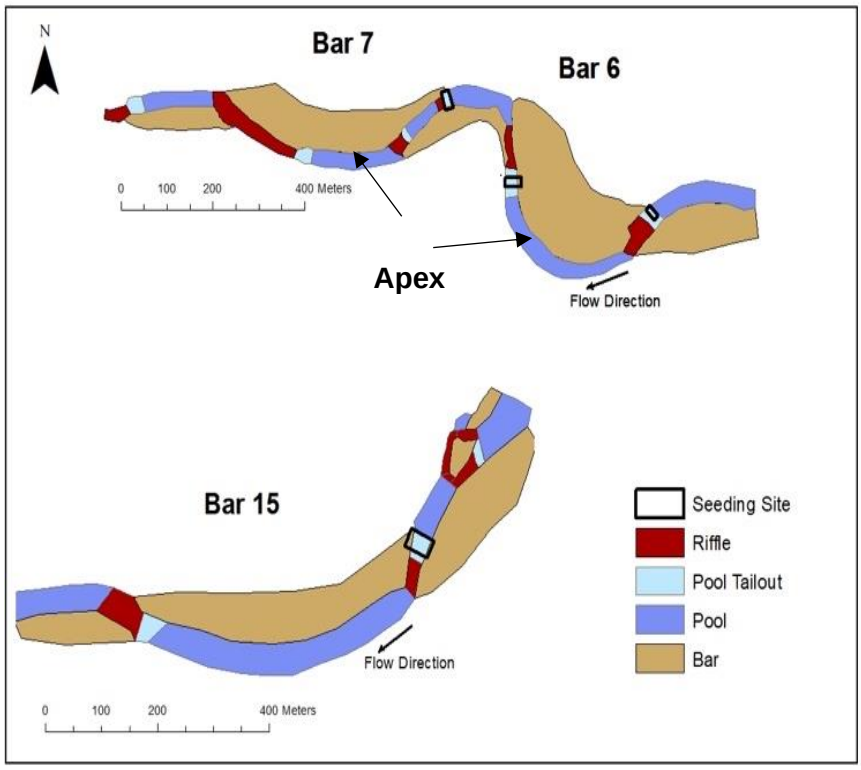

Figure 7. Map of the three San Juan River Study Reaches (Bar 6, 7, and 15).

Depiction of macro-bedform morphological units: riffle, pool tailouts, pool, and bar. Pool tail-outs (location of seeding site) occur at the transition of pool to riffle. The bar apex, which is defined as the bend, or most laterally-extended section of the gravel bar, is also labelled for Bar 6 and Bar 7.

Figure 8. Salmon spawning nests (redds) at the Bar 15 study reach.

Salmon spawning areas at the Bar 15 study reach (September 2021).
Redds can be seen in the lower left of the image (areas of clean gravels).

The gravel point bars in the three study reaches are representative of the typical length, width, overall appearance, and grain size distributions of gravel bars found in the mainstem alluvial reach. Characteristics of the three gravel bars involved in this study are presented in Table 4. Measurements of individual bars were extracted from 2015 digital elevation models (DEMs). Measurements of bar length were taken from the head to the tail of each bar, following the centreline of the bar. To extract the slope, using the polygon tool in ArcGIS, an average elevation from DEM cells was extracted at the head of the gravel bar and differenced from an average elevation at the tail of the bar and then divided by the length of the bar between them.

Table 3. Characteristics of the three gravel bar study reaches.

Gravel Bar	Length (m)	Average Width (m)	Slope	D_{50} (mm)	D_{84} (mm)	D_{90} (mm)
Bar 6	550	100	0.0038	50	84	95
Bar 7	540	55	0.0031	43	87	103
Bar 15	585	45	0.0009	28	67	88

4 Methods

Two primary datasets were collected for use in this study: particle tracking data to observe particle dispersion and scour, and aerial surveys to capture grain size and topography. Individual particle tracking data using RFID technology was collected for two seasons (2019-20, 2020-21) spanning the winter flooding period (Oct-July). Repeat annual aerial surveys were collected by way of uncrewed aerial vehicle (UAV) and aerial LIDAR technology for the two tracer deployment seasons, using the imagery to assess morphologic changes in the mainstem channel at the study locations.

4.1 Individual Bed Particle Tracking

Individual particles were tracked through the use of RFID low-frequency PIT (Passive Integrated Transponder) tags, commonly used in fluvial environments for bedload tracking (Arnaud et al., 2015; Cassel et al., 2016; Chapuis et al., 2014; Lamarre et al., 2005). Tags were purchased from Oregon RFID (Oregon RFID, 2021). Once activated, tags transmit a unique identification code that is communicated to the reader via radio waves that can be read at a short distance that depends on tag size and antenna design. Tracer stones were fabricated by drilling and inserting the PIT tags into natural grains collected from the field in 2015, then sealed with epoxy resin (Figure 9). To optimize tracking and recovery, tracers were also painted and numbered with an ID distinct from the unique ID of the PIT tag. An inventory database was created, with records of both RFID and written ID numbers for all tracer stones prior to deployment. A detailed description of tracer fabrication can be found in McQueen (2019).

Figure 9. Example of a prepared 64-90 mm tracer stone, with 32 mm PIT tag (right).

4.1.1 Tracer Tracking and Deployment

Tracers were deployed in October 2019 and 2020 at three gravel bar study reaches (Bar 6, Bar 7, Bar 15), prior to winter high flows when bed mobilization and morphologic change to the channel are expected to occur (Table 5). Over two years, 611 tracers were deployed on the riverbed surface as well as 216 tracers deployed that were buried in the subsurface (Table 5). The number of tracers chosen for deployment is based on previous recovery results for tracer work in the San Juan River (McQueen, 2019). Furthermore, buried tracers are limited in the number deployed (N = 36), because of feasibility issues. It takes ~30 min of digging to bury each tracer, with subsequent recovery digging taking even longer due to the unknown recovered buried location.

Table 4. Tracer deployment dates for the two deployment years.

Location	Deployment Date	Deployment Type	# of Tracers seeded
Bar 6	October 28th, 2019	Surface	106
		Buried	36
	October 20th, 2020	Surface	100
		Buried	36
Bar 7	October 28th-29th, 2019	Surface	100
		Buried	36
	October 20th, 2020	Surface	100
		Buried	36
Bar 15	October 29th, 2019	Surface	98
		Buried	36
		Coarse Rocks	7
	October 22nd, 2020	Surface	100
		Buried	36

Grain size distributions for surface tracers aimed to be representative of the natural riverbed and were based on Wolman counts (Wolman, 1954) conducted for the three seeding sites in 2015 (Figure 10). Additionally a set of seven coarse tracers were deployed at bar 15 to analyze coarse particle mobility and their role in controlling channel dynamics (MacKenzie et al., 2018) and bed scour depth (Dusterhoff et al., 2017) using binned groups of 91-128mm and 128-180mm. Particles used for buried seeding were selected from the same binned groups that were used for surface deployment: 22-32mm, 32-45mm, 45-64mm, and 64-90mm. PIT tags are too large to be inserted

in particles less than 22mm, leading to an under-representation of fine grained material, which is common in RFID studies (Chapuis et al., 2015; Lamarre et al., 2005; Vazquez-Tarrio et al., 2019).

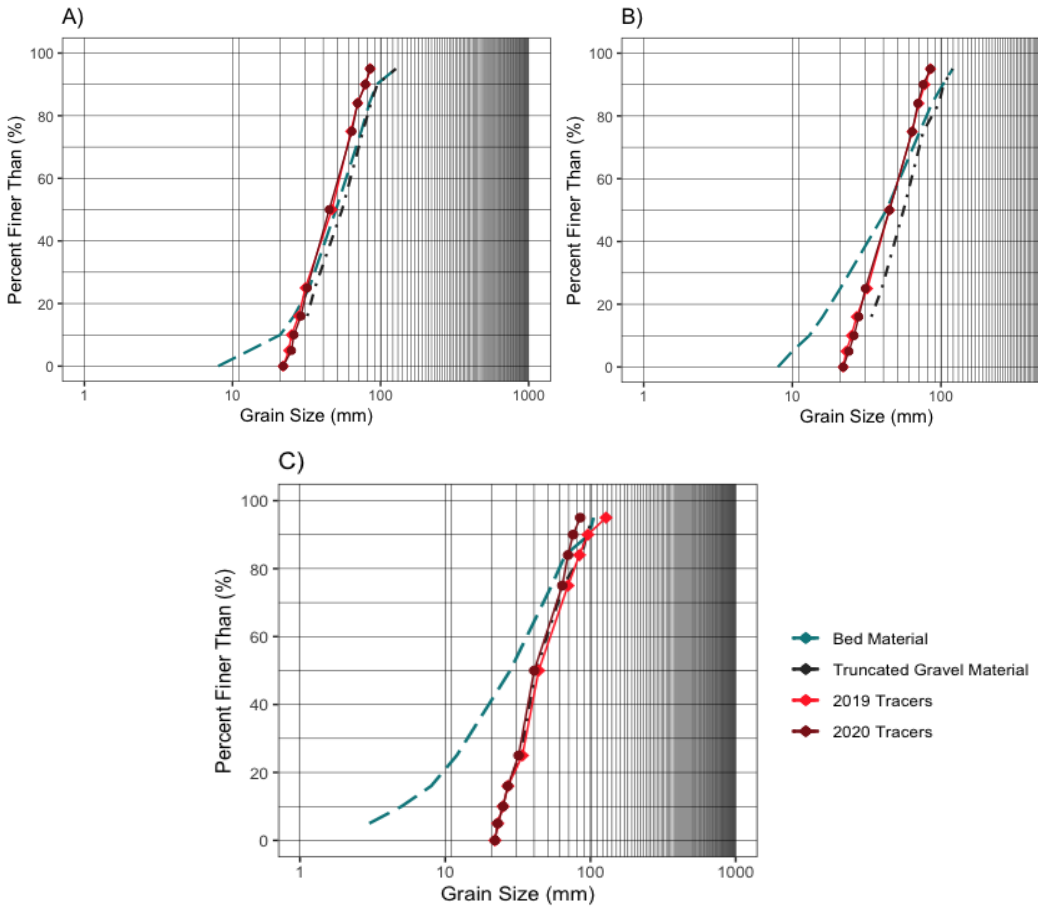

Figure 10. Grain size distribution of the bed material, truncated gravel material (>22mm), tracers for A) Bar 6, B) Bar 7, and C) Bar 15.

Surface tracers were deployed at pool-riffle transitions, also known as pool tail-outs, to assess particle mobility and pathlengths at three gravel bar study reaches. The tracers (~100 per site) were seeded in clusters grouped by grain size, spanning the entire width of the wetted-channel along lines perpendicular to the direction of flow at the three sites of deployment (Figure 11). Lines were spaced at ~1m intervals to reduce the risk of RFID signal collision (Chapuis et al., 2014). Due to channel changes, the deployment location at the Bar 6 reach was moved 10m downstream for the

2020-21 year and the Bar 7 deployment location moved ~20m upstream for the 2020-21 deployment year.

In addition to surface tracer deployment, tracers were also buried to assess scour. Buried tracers (36 per study reach) were deployed in the subsurface at the gravel bar margins in parallel lines; tracers could not be buried in the wetted channel, because wading depths even at low flows are too high, thus the bar margin was the most proximal location to assess scour near pool tail-outs (Figure 11). Buried tracers were deployed perpendicular to the surface launch lines and parallel to the channel flow direction and spaced ~1m apart (Figure 11). An equal number of tracers (n = 12) were buried at either 10, 20, or 30cm depths with the same proportion of grain size classes buried at each depth. Chosen burial depths are representative of average burial depths for all five Pacific salmonid species (ranging from 10cm – 50cm). This study design of unfixed vertical burial of RFID tracers can provide further knowledge on the relationship of active layer depth and subsequent pathlength travel distance. Only one previous study conducted by Brousse et al. (2018) has used stationary active RFID columns to assess active layer depths, to the author's knowledge.

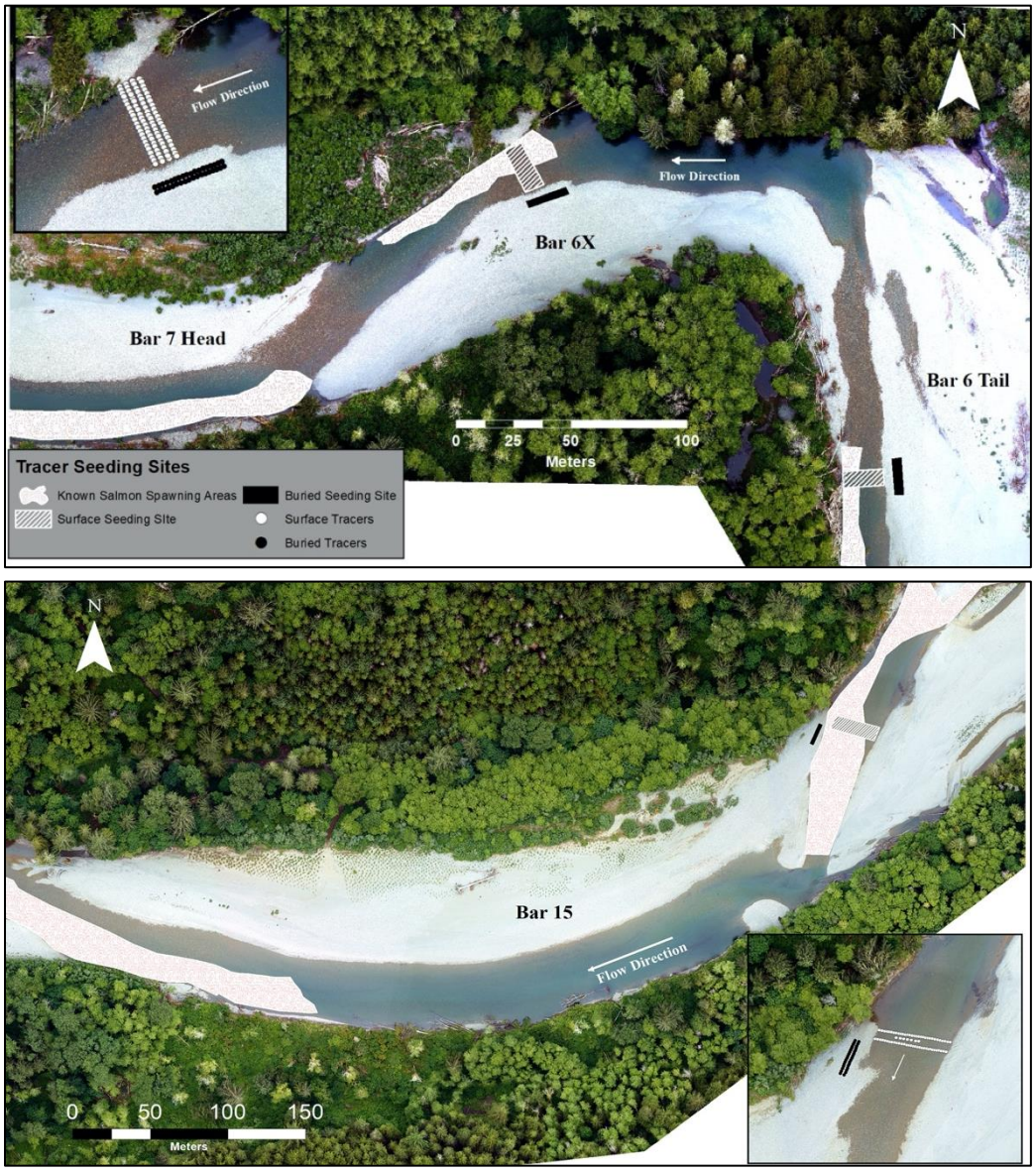

Figure 11. Depiction of tracer deployment locations and study design for A) Bar 6 and 7; B) Bar 15. Insets show close up of deployed transects. Flow right to left.

4.1.2 Tracer Stone Recovery

Recovery of tracers was done after the winter flood season, beginning in July during the low-flow season to maximize searchable areas (pools). Areas that were too deep to wade even at low flow (deepest portions of pools) were searched using a small boat. Two antennas were used to find tracers in the recovery process; a smaller hand-held antenna used to locate immobile and buried tracers as well as a large more complex antenna system used to search large areas, both purchased

from Biomark® (Biomark, 2019) (Figure 12). The antennae detect the RFID tags and simultaneously buzz a reader (digital screen) with the associated unique identification number of the RFID tag. The smaller antenna has a read range of ~45-50cm for 32mm PIT tags, while the larger antenna has a read range of up to 1.75m, however read range varies depending on tag orientation (Arnaud et al., 2015; Chapuis et al., 2014). The maximum extent searched using the antenna systems differed for each bar, but generally the first two bars downstream of the seeding site were searched. Tracer recovery was labor-intensive and took approximately three weeks with a team of three to four people.

Figure 12. Large antenna cord system with backpack fastened to PVC pipe frame using ropes, pulleys, and cams.

The searching process involved an initial sweep of the launch lines with the hand-held antenna followed by the use of the large antenna frame system to search large areas of both the dry exposed bars and wetted channel, searching in a downstream direction. The search method involved 50m path lines, parallel to the channel that were then marked with flagging tape. Search lines had ~1.5m overlap to ensure all areas were searched thoroughly. Once a tag was identified by the reader, an accurate location of the tracer was determined using triangulation methods; the user would walk forward, backward, and at varying angles, to determine the detection limits of the tag. The verified location was then marked with a small yellow peg and labelled with the unique RFID number. Once a full section was searched, the hand-held antenna was then used to pinpoint and refine the location (if possible) of the detected tracers. In the deeper water the backpack component of the

antenna-cord system was stationed in the middle of the boat, with the antenna-pipe frame draped off the back of the boat. Once the reader identified a tracer, the boat was stalled and a GPS averaged-waypoint was recorded.

Once recovered, tracer positions were recorded as a GPS averaged waypoint using a handheld Garmin GPS with typical error in the range of < 1m but up to 3m on overcast days. Average pathlengths of mobile tracers were ~150-200m thus resulting in less than 5% error (initial and final GPS points) (Garmin, 2019). To account for instrument error the threshold to deem a tracer mobile was set to 10m. Once located, the burial depth, grain size, RFID number, written number and morphology were recorded in a written notebook. Burial depth for both buried and surface tracers recovered was measured using a shovel handle to represent bed surface levels, and a hand-held measuring tape to measure from the bed surface to the top of the tracer stone, to the nearest 5mm (Figure 13). Not all tracers could be physically recovered as some were deposited in the wetted channel or buried too deeply. Tracers that were buried too deep for detection using the hand-held wand antenna were assumed to be deeper than 30cm, which is a conservative estimate of the maximum detection range of the wand antenna (~50cm).

Figure 13. Measuring tracer burial depth from top of the bed surface (shovel handle) to the top of the tracer stone.

4.2 Pathlength Analysis

GPS waypoints of initial and final tracer positions were uploaded to ArcGIS and stored in a geodatabase as a point feature class. Field notes of tracer characteristics (morphology, burial depth, grain size) were imported as attribute data to the point feature class of tracer recovery locations. Orthoimages of the gravel bars collected from aerial surveys during the low flow period of July 2020 were used for mapping and subsequent pathlength analysis. Pathlengths of mobile tracers (>10m) were measured by delineating a longitudinal profile along the channel centreline (thalweg) and projecting tracer positions along the profile which is the common method of pathlength analysis seen in the literature (Arnaud et al., 2017; Liebault et al., 2012; MacVicar et al., 2015) as well as the method used for past tracer data on the San Juan (McQueen et al., 2021).

4.3 Hydrological Analysis

To understand the influence of flow characteristics on tracer particle movements, discharge data from the WSC hydrometric station was used to calculate multiple metrics describing hydrological conditions for the 2019 and 2020 study period as well as to compare with three years of previous tracer data on the San Juan (2015-2018) (McQueen, 2019). For this study, bankfull discharge (Q_{bf}) of 650m^3 s^{-1}, with a recurrence interval of 1.5 years ($Q_{1.5}$), is taken to represent the threshold of mobilizing flow events at which sediment mobility is initiated (Q_c). In other studies, the critical discharge (Q_c) has been assessed more precisely, especially in smaller rivers, based on tracking mobility for individual events for which discharge and mobility data are available (Haschenburger, 2013; Hassan et al., 1992; Pfeiffer et al., 2017). Variability of grain size and multiple mobilizing events per season between tracer development and recovery, precludes this approach in the San Juan River. Alternative discharge thresholds were investigated and saw minor changes to the number of potential mobilizing events in a season (McQueen, 2019).

Hassan et al. (1992) helped elucidate the idea that since the majority of mobilization occurs during the largest events, the largest measured discharge during these events, termed the maximum peak discharge (Q_p), is thereby a dominant control on sediment transport. However, sediment mobilization occurs for all flows above bankfull and thus, for a hydrograph that has multiple mobilizing events, a metric to incorporate both the magnitude and duration of flows above the threshold discharge is needed to investigate the effect of flow magnitude on tracer dispersal. Previous studies on tracer dispersal and channel morphodynamics have used the total excess flow

energy (Ω_T) (Haschenburger, 2013) as a metric that captures both magnitude and duration of flows for multiple mobilizing events (Wheaton et al., 2013; Papangelakis & Hassan, 2016). To use this metric, knowledge of the critical discharge (Q_c) is needed, therefore a modified Ω_T was used in analysis for each flow season whereby the total flow above estimated bankfull, assumed to be similar to Q_c, was integrated over the period between tracer deployment (t_d) and recovery (t_r):

$$\Omega_T = \rho g S \int_{td}^{tr} (Q - Qbf) dt$$

where ρ = the density of water (1,000 kg/m^3), g = the acceleration due to gravity (9.81m/s^2), and S = the gravel bar reach slope. Discharge data from the WSC gauging station is collected in 5 minute intervals and therefore was integrated at 5 min intervals. The Ω_T, was also used to calculate excess flow energy for the peak mobilizing event (Ω_P) (flood event with the maximum peak discharge) for each season, as well as maximum peak discharge (Q_p). This allows for further analysis of differences in annual tracer movement that might be explained by differences in annual hydrologic conditions such as the magnitude or duration of flows. Differences are further explored in relation to morphologic control, at the scale of the dominant channel morphology.

4.4 Channel Change (Aerial Surveying) Analysis

To observe annual channel changes during the tracer deployment period, repeat aerial surveys were conducted to collect aerial imagery at the three study reaches. To capture topographic changes for the first deployment year, aerial surveys were collected by uncrewed aerial vehicle (UAV), or drone, in July 2020, as well as the collection of supporting topographic data using total station and real-time kinematic (RTK) surveying at the three study reaches. For the following 2020-21 deployment year, an aerial lidar survey was made available by the B.C. Ministry (FLNRORD). The lidar survey was conducted in March 2021 by Terra Remote Sensing Inc. To clarify, only aerial imagery extracted from the lidar data was used in the analysis for this study, as well as aerial imagery from a previous lidar survey in the summer of 2019, to plot tracer recovery locations. This section will provide an overview of the methods used for the 2020 drone survey collection and analysis.

4.4.1 Data Collection

Imagery was acquired over three days during the week of July 13th 2020, using a DJI Phantom 4 Advanced uncrewed aerial vehicle (UAV). The weather was sunny, with moderate to high winds. Approximately ~400 images, which varied slightly between reaches, were captured from an altitude of 60m with an 80% overlap between consecutive photos. Camera specifications for the Phantom 4 Advanced camera can be found in Appendix A. Accuracy of the Phantom 4 Advanced's image georeferencing was increased by RTK surveying of three reference ground control points (GCP's) collected by Griffin Fisk (B.C Ministry employee). At each study reach, 17 ground control points (GCPs) were surveyed with a total station and accurately georeferenced by triangulating the position of each GCP with the position of the three reference RTK GCPs. The coordinate system used was NAD 83(CSRS)/UTM Zone 10N. GCPs were evenly distributed across the gravel bar and at a variety of elevations.

4.4.2 Data Processing

The collected UAV imagery was subsequently analyzed using AgiSoft Metashape software (AgiSoft, 2021). Prior to processing, the image quality function was used to ensure all images had a quality value above 0.5 (the recommended value by AgiSoft). All imagery had a quality above 0.80, therefore no images had to be excluded. An initial sparse point cloud was generated using the 'Align Photos' function with accuracy set to 'Highest' and pair pre-selection set to generic; no point or tie limit was used. The gradual selection tool was used with the 'Reconstruct Uncertainty' criterion set to 10 and 'Reprojection Error' criterion set to 0.5 to identify and remove tie points with a high degree of uncertainty. The 'Optimization tool' was then used to optimize photo alignment and camera locations.

Georeferencing was done by going through each image and locating individual GCPs. Once located, a GCP marker was created and placed at the centre of each GCP in all images, this was done by using the 'Filter Photos by Marker' tool and repeated for all 17 GCPs. The GCP markers were then associated with their real-world coordinates that were collected during the total station surveying. GCP coordinates and precision (error) for the three study reaches can be found in Appendix A. Following georeferencing, a dense point cloud was built with quality set to 'Ultra-high' and 'Aggressive' depth filtering. Finally, a digital elevation model (DEM) and orthomosaic (orthoimage) was built and exported as a .tiff file.

5 Results

5.1 Introduction

Firstly, section 5.2 discusses results of channel changes, as well as changes to the gravel bar at the three study sites (Bar 6, 7, and 15) that occurred between the 2019-2021 study period. The following section 5.3 describes bar size sorting characteristics at each study site from Wolman counts conducted in 2020. Section 5.4 and 5.5 provide surface and buried tracer results, respectively.

5.2 Changes in Reach-scale Channel Characteristics

Changes to the channel boundaries and gravel bars at the three study reaches (Bar 6, 7, 15) from 2019-2021 were broadly observed, to better understand particle dispersion and the link to overall channel change and bar development. Aerial imagery from July 2019 and March 2021 collected LIDAR data, was used to delineate channel boundaries, and were plotted using the ArcGIS polygon tool. The bar 6 channel boundaries could not be delineated from the 2021 March LIDAR because of the limited extent, specifically the left bank boundary of Bar 6 that wasn't captured in the imagery. Aerial images of Bar 6 and Bar 15 from July 2020 UAV surveys were also used to delineate channel boundaries, however imagery for Bar 7 could not be used due to the limited extent of the image. Channel boundaries were then plotted over the 2021 imagery for each study reach. The gravel bars at the three study reaches could not be properly delineated for the 2020-21 winter flood period as the aerial imagery was collected in March at higher flows, when the gravel bars were more inundated.

Channel and gravel bar boundaries were difficult to delineate, particularly where riparian vegetation overhangs the river on the left bank and areas where vegetation growth on the gravel bars transitions into bank vegetation. Furthermore, an accurate estimate of the error from manual delineation of channel boundaries cannot be made However, areas of most significant change (greatest bank retreat) are the focus of this analysis and were precisely delineated by referencing DEM's which helped reveal the cut off between the active channel and floodplain areas. Channel boundary areas that were more ambiguous will be further discussed with specific reference to each gravel bar study reach in the following section 5.2.1.

5.2.1 Channel Change Boundaries

Bar 6

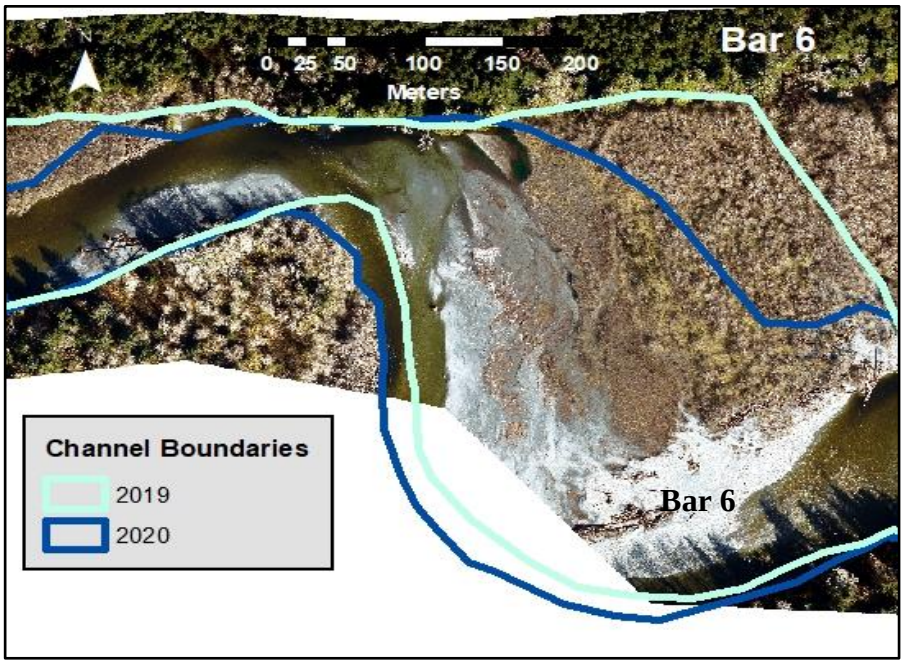

Figure 14. Annual change to channel boundaries (2019-2020) at the Bar 6 study reach. Flow right to left.

The right bank boundary on the inside of Bar 6 (attached to the gravel bar) could not be properly delineated from the 2020 orthoimagery and instead represents the extent of the 2020 orthoimagery, not the channel boundary (Figure 14). However, previous channel boundary assessments by the BC Ministry (FLNRORD) indicate that the right bank channel boundary has been relatively stable since 2011 (McQueen, 2019). The left bank channel boundary at Bar 6 shows significant bank retreat occurring during the 2019-20 winter flood period, with the most significant change at the bend of Bar 6X, opposite the Bar 6 tail (Figure 14). The channel is locally constricted by exposed bedrock on the right bank at the Bar 6 tail, which can explain the significant bank retreat occurring at the opposite bend (left bank bend at the Bar 6X head) (Figure 14). Furthermore, the annual left bank retreat (erosion to the left bank of the channel) that occurred during the 2019-20 period at Bar 6 is significantly greater than the observed annual left bank retreat that has occurred since 1995 (McQueen, 2019). High rates of channel change can be attributed to the extreme flood event during that year with similar observations seen in the literature (Lisenby et al., 2016; Gervasi et al., 2021).

The left bank of Bar 6 has been retreating significantly since 1995 (first year of channel boundary assessment), and has continued despite the right bank remaining relatively stable since 2011 (McQueen, 2019). This suggests that in-channel deposition related to the lateral development of Bar 6 has forced the channel towards the left bank causing erosion. Lateral development of Bar 6 will be discussed further in section 5.2.2.

Bar 7

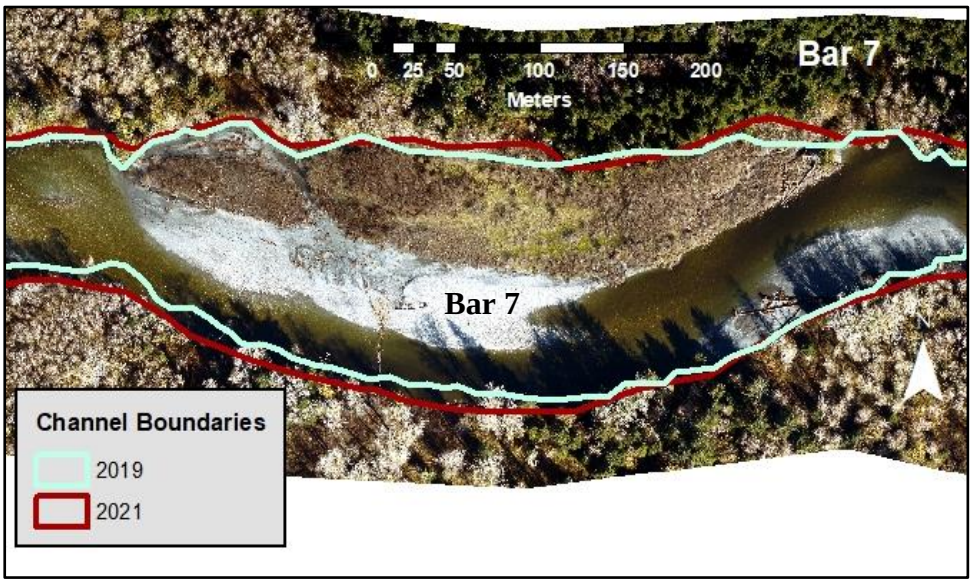

Figure 15. Channel boundary changes (2019-2021) at the Bar 7 study reach. Flow right to left.

Bar 7 channel boundaries were delineated from 2019 and 2021 aerial imagery and are plotted on the 2021 aerial imagery (Figure 15). The right bank channel boundary at Bar 7 has some error due to the difficulty distinguishing the cut off between bar vegetation and bank vegetation, however there appears to be minimal channel changes to the right bank, which is consistent with channel boundary changes since 1995 (Figure 15) (McQueen, 2019). Similar to Bar 6 processes, almost all bank retreat is occurring at the left bank opposite of Bar 7, although significantly less retreat relative to the left bank opposite Bar 6 (Figure 15). The greatest area of bank retreat that occurred between 2019 - 2021 at Bar 7 appears to be opposite the bar apex and near the bend at the Bar 7 tail (Figure 15). Furthermore, channel widening at Bar 7 has been attributed to the retreat of the left bank since

1995, with evidence that the rate of bank retreat opposite of Bar 7 has declined in recent years (McQueen, 2019).

Bar 15

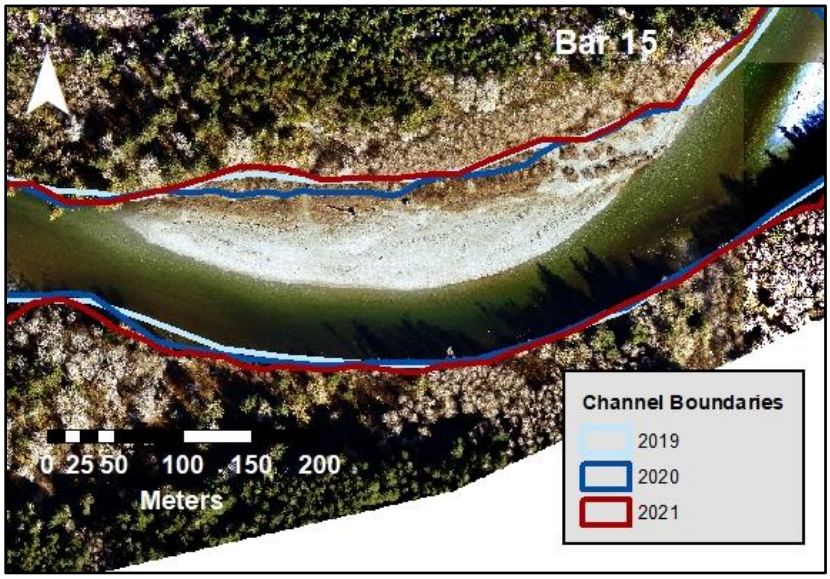

Figure 16. Channel boundary changes (2019-2021) at the Bar 15 study reach. Flow right to left.

Bar 15 channel boundaries were delineated for all three years using 2019 and 2021 aerial imagery as well as 2020 aerial imagery from UAV surveying (Figure 16). The right bank channel boundary at Bar 15 also has some error due to the difficulty distinguishing the cut off between bar vegetation and bank vegetation, however, similar to Bar 7 there appears to be negligible change to the right bank (Figure 16). Bar 15 has experienced significantly less change to both the left and right bank channel boundaries since 1995 compared to the other two study reaches, which is consistent with channel boundary changes for this study period between 2019 and 2021 (Figure 16) (McQueen, 2019). However, for the 2019-2021 period, some change has occurred, with the most evident bank retreat near bends, specifically at the left bank opposite the tail of Bar 15 as well as to the right bank at the head of Bar 15 which is typical for gravel-bed meandering rivers and indicates gradual down valley migration of bends (Clayton, 2008) (Figure 16). Overall bank retreat at the reach-scale appears to occur at a much slower rate at the Bar 15 seeding site, relative to both Bar 7 and Bar 6.

5.2.2 Gravel Bar Changes

Bar 6

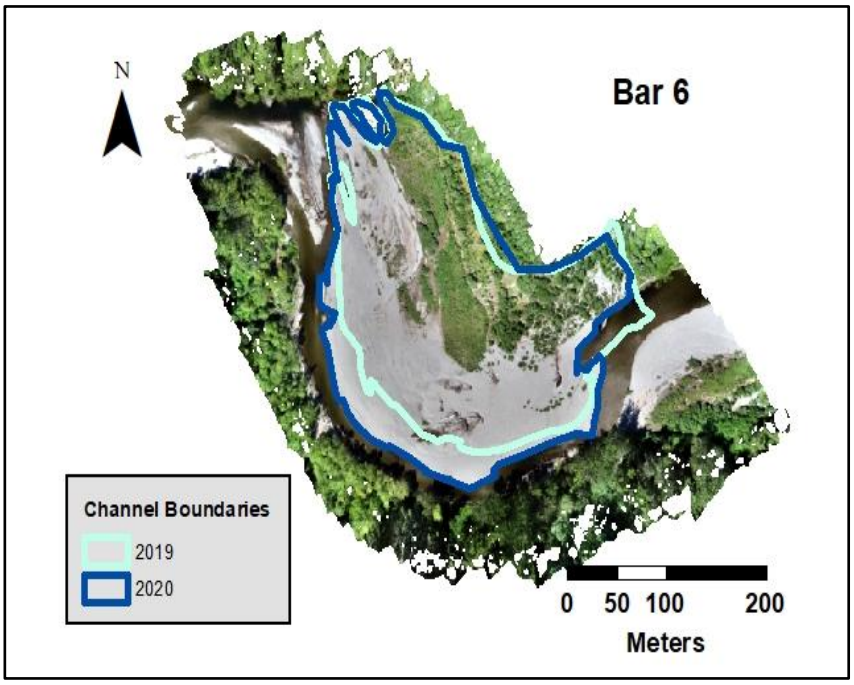

Figure 17. Changes to the gravel bar (2019-2020) at the Bar 6 study reach. Flow right to left.

Delineation of the upper right boundary of Bar 6 involves some error because of dense vegetation growth, however, the majority of bar growth is occurring laterally or longitudinally, with little to no change to the right bank vegetated area (Figure 17). There appears to be some erosion of the gravel bar at the head of Bar 6, and minor deposition and growth at the bar tail, as well as considerable lateral expansion near the apex (Figure 17). Bar 6 displays a well-known pattern of bar evolution with rapid lateral expansion and a high rate of erosion of the opposite (left) bank (Rice et al., 2009). The downstream migration and lateral expansion occurring between 2019 and 2020 at Bar 6 are in agreement with previous findings of lateral growth at the bar apex observed from the previous tracer study (2015-2018) (McQueen, 2019). Furthermore, from 2015-2018, McQueen (2019) also identified a ~1m thick bedload sheet that migrated from the bar head, accreted laterally and stopped near the bar apex. The exposed bedrock bend at the tail of Bar 6

limits the longitudinal growth of the bar, and is a possible explanation for why the bar is primarily growing laterally at such a high rate (Figure 17).

Bar 6X and 7

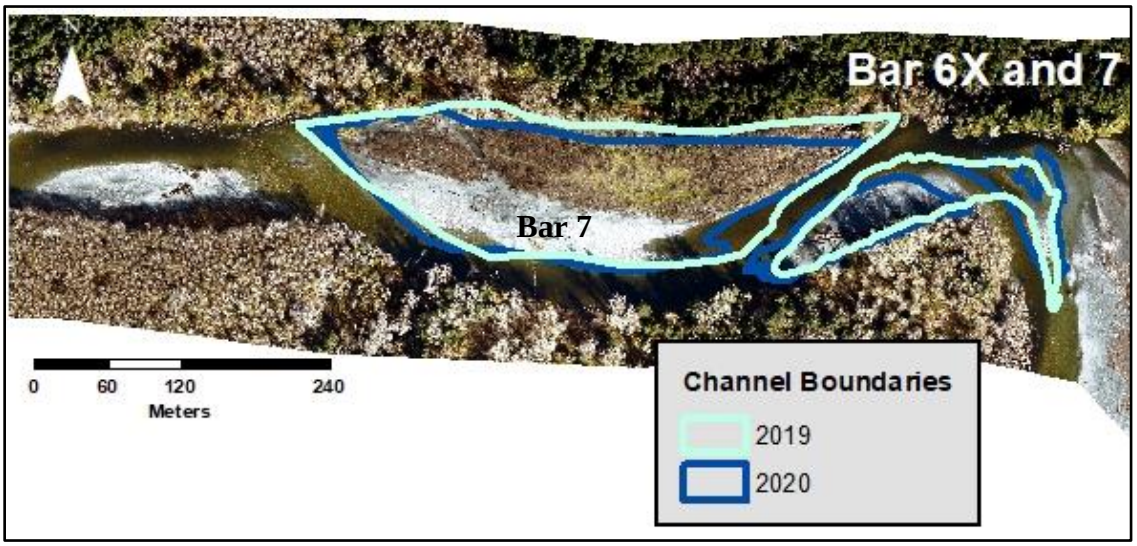

Figure 18. Changes to gravel bar 6X and 7 (2019-20) at the Bar 7 study reach. Flow right to left.

Bar 6X saw considerable changes from the 2019-20 year, which is not surprising due to its location, with high rates of erosion because of channel narrowing at the bend (Figure 18). During the 2019-20 flooding period, a chute cut-off was formed and subsequent channel avulsion at the bend of Bar 6X, which lead to significant changes to the gravel bar (Figure 18). The gravel bar became divided, with a newly formed channel island and a subsequently reduced area to bar 6X (Figure 18). The change in flow direction most likely caused subsequent erosion at the apex of Bar 6X, with longitudinal expansion at the Bar 7 tail (Figure 18). Although no delineation of the gravel bar was done using the 2021 imagery because of higher flows and greater inundation, there was apparent longitudinal and lateral growth at the head of Bar 6X for the 2020-21 year, with exposed gravel expanding farther than the 2020 boundary of the bar (Figure 18).

The right bank boundary of Bar 7 could not be accurately delineated because of the difficulty distinguishing between bar and bank vegetation, however it is assumed little to no change occurred at this boundary based on previous years (McQueen, 2019) (Figure 18). The most significant change to Bar 7 was erosion at the bar head which may be attributed to channel avulsion occurring at the bend and subsequent changes in flow direction (Figure 18). Previous observations by

McQueen (2019) of erosion of the left bank opposite Bar 7, as well as high tracer deposition at the apex of Bar 7, suggest long-term lateral growth of the bar. Erosion to the left bank was focused closer to the Bar 7 tail, with identifiable lateral growth of the bar from 2019-20 adjacent to this area of erosion (Figure 18).

Bar 15

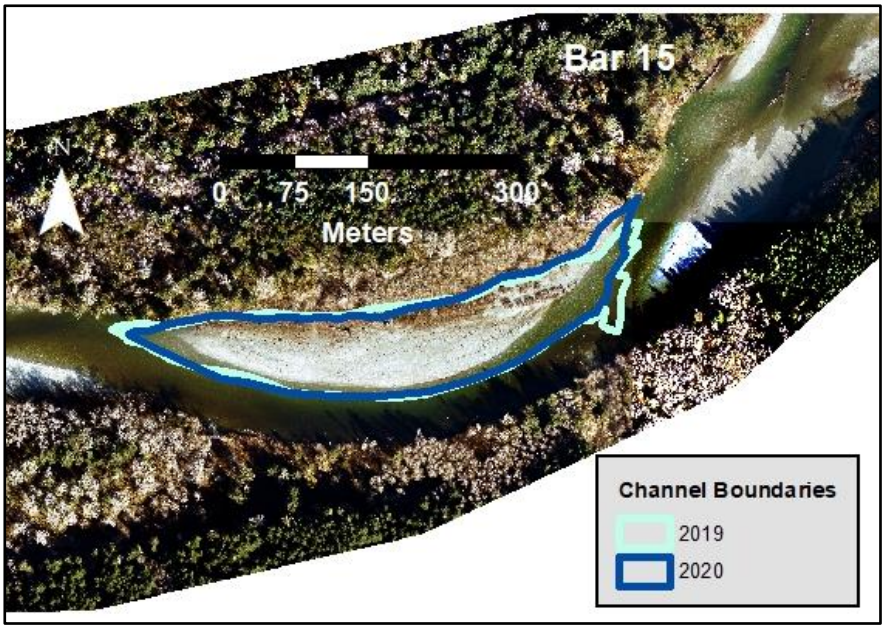

Figure 19. Changes to the gravel bar (2019-2020) at the Bar 15 study reach. Flow right to left.

Similar to results of minimal channel boundary change to the Bar 15 reach between 2019-2021, there was little change to the gravel bar itself (Figure 19). There appears to be some change, with considerable longitudinal and lateral erosion at the bar head which most likely can be attributed to the 100-year flood occurring in January 2020 (Figure 19). Results from the previous tracer study on the San Juan also found that Bar 15 is primarily being built by vertical accretion with limited lateral growth of the bar, which aligns with the minimal change observed from 2019-2020 (McQueen, 2019). Overall, Bar 15 appears to have undergone less extreme morphologic change, with minimal erosion to the left bank and limited lateral bar growth relative to the other two seeding sites.

5.3 Gravel Bar Grain Size Characteristics

Surface Wolman counts (Wolman, 1954) were conducted in July of 2020 at each of the three study sites at three distinct locations on the gravel bar: head, apex, and tail. Results from the Wolman counts provide insight into potential patterns of particle size sorting on the three gravel bars of interest (Figure 20). At all three study sites, the grain size distribution at the bar head was coarsest (Figure 20). At Bar 6, the apex and tail saw finer grain distributions that were almost identical (Figure 20). However, for both Bar 7 and Bar 15, the grain size distribution at the bar tail was considerably finer than both the apex and head of the bars (Figure 20). Differences in the distribution between gravel bars can also be seen, with Bar 15 having an overall finer grain size distribution at the head, apex, and tail relative to the distribution at Bar 6 and 7 (Figure 20). The results from the Wolman counts provide evidence of grain size sorting patterns on the gravel bars, more specifically downstream fining of grain size from the bar head to the bar tail. This is common in wandering gravel bed rivers with well-developed bar morphology because of the trajectory of secondary flows that have the capacity to carry only finer particles along the inward apex of the bar (Clayton, 2010).

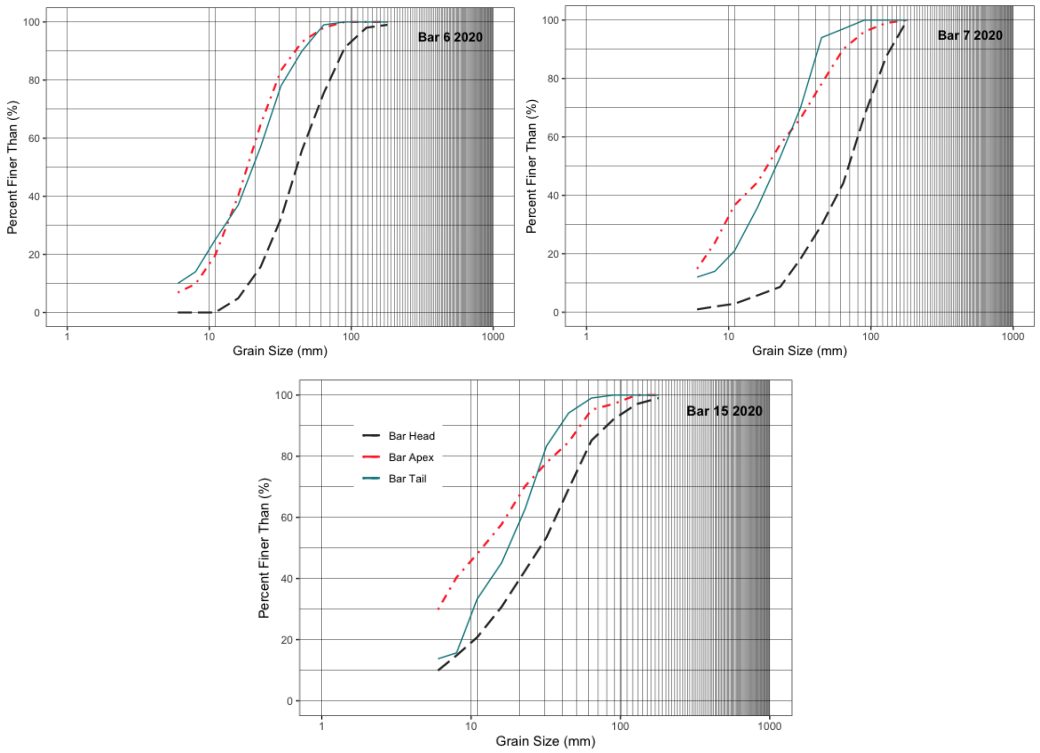

Figure 20. Wolman count results (July 2020) of the grain size distribution at Bar 6 (top left), Bar 7 (top right) and Bar 15 (bottom).

5.4 Surface Tracer Results

5.4.1 Introduction

Approximately 100 surface tracers were deployed at each of the three study sites (Bar 6, 7, 15) for the 2019-20 and 2020-21 deployment years. Tracers were deployed across the surface of the wetted channel at pool tail-out locations. Tracer particles were binned into four grain size classes representative of the grain-size distribution on the natural bed surface. Surface tracers were deployed in October and recovery took place the following July at low flow. Surface tracer results for the 2019-20 and 2020-21 deployment year include analyses with three years of previous tracer results on the San Juan River (McQueen, 2019). An overview of results for surface tracers is presented in section 5.4.2. The results of particle mobility and pathlength distances of recovered surface tracers as well as the influence of grain size and flow on mobility and pathlength distance can be found in sections 5.4.3 - 5.4.5. Pathlength and exceedance probability distributions were analyzed to better understand particle dispersion and results can be found in section 5.4.6. Section 5.4.7 describes tracer deposition by morphological unit and lastly, section 5.4.8 examines burial depths of recovered mobile tracers.

5.4.1.1 Hydrological Analysis

An analysis of the hydrological events that occurred during the winter flooding season for the past two deployment seasons along with the previous three tracer deployment seasons was conducted (McQueen, 2019). For the 2019-20 deployment period, there was one mobilizing event above Q_{bf}, with $Q_p = 1360 m^3 s^{-1}$ which is estimated to be $2.1Q_{bf}$, and a recurrence interval of at least 100 years. The 2020-21 deployment season saw the least amount of hydrological activity, with only one event above Q_{bf} with a peak discharge of 735 $m^3 s^{-1}$. The small flood event ($1.1Q_{bf}$) was of short duration, with excess flows totaling 8 hours above bankfull (Table 5). Peak discharge during the previous deployment seasons (2016-17 to 2018-19) was similar to the two most recent deployments, ranging from 749 $m^3 s^{-1}$ – 1,003 $m^3 s^{-1}$ (Table 5).

Table 5. Results from the hydrological analysis for all (2016 – 2021) deployment years.

Year	Number of Events $Q > Q_{bf}$	Maximum peak, Q_p (m^3s^{-1})	Total Time $Q > Q_{bf}$ (hours)	Total Excess Flow Energy, Ω_T (MJ/m)		Peak Event Excess Energy Ω_P (MJ/m)	
				Bar 6 & 7	Bar 15	Bar 6 & 7	Bar 15
2016-17	2	749	22.5	66.7	36	56.9	30.7
2017-18	4	1,003	44	352.5	190.2	157.5	85
2018-19	2	942	28	150.5	81.2	139.3	75.2
2019-20	1	1,360	21	421.1	227.2	421.1	227.2
2020-21	1	735	8	20.1	10.9	20.1	10.9

5.4.2 Overview of Surface Tracer Results

An overview of surface tracer results can be found in Table 6. Recovery of surface tracers were similar between deployment years, ranging from 60.3 - 83% for the 2019-20 deployment and from 60 – 76% for the 2020-21 year (Table 6). For both tracer deployment years, Bar 6 surface tracers had the lowest recovery. A possible explanation for the low recovery is the deep pool located ~150m downstream of the seeding site, where tracers may have been deposited at water depths beyond detection. The smaller two size classes of surface tracers deployed (22-32mm and 32-45mm) had lower recovery rates, with an average recovery of ~65% compared to ~77% recovery for the largest size classes (45-64mm and 64-90mm). This was especially the case for Bar 6, where the 22-32mm size surface tracers had a recovery rate of just 50% for both years, and the 32-45mm had a slightly higher recovery of 60% and 64% for the respective two years. Differences in recovery rates between grain sizes was also seen in previous tracer work on the San Juan River (McQueen, 2019; McQueen et al., 2021).

Table 6. Summary of surface tracer results for the 2019-20 and 2020-21 deployment year.

Year	Q_p (m^3 s^{-1})	Recovery (%)	F_m	$\bar{L}$ (m)	L_m (m)
		Bar 6			
2019-20	1360	60.3	1	306.2	168.4
2020-21	735	60.0	0.98	157.1	73.9
		Bar 7			
2019-20	1360	83.0	0.96	393.8	425.1
2020-21	735	74.0	0.96	253.3	223.1
		Bar 15			
2019-20	1360	72.4	0.94	344.2	297
2020-21	735	76	0.33	139.4	81.2

5.4.3 Mobility and Pathlength Distance

Mobility was calculated as the fraction of recovered tracers (F_m) that moved more than 10m downstream from the initial seeding site. Recovered surface tracers had high mobility across both deployment seasons ($F_m > 0.90$ for all study reaches) with the exception of Bar 15 for the 2020-21 season ($F_m = 0.33$) (Table 6). Negligible differences in mobility are seen between grain size classes for both Bar 6 and Bar 7 study reaches, as almost all particles were mobilized (Table 6; Table 7). Differences in mobility between size classes of tracers is apparent for the Bar 15 reach that had low mobility during the 2020-21 year. The smallest grain size class (22-32mm) had the highest number of tracers mobilized, and the largest grain size class (64-90mm) had the lowest number of tracers mobilized (Table 7). Recent channel avulsion and subsequent changes to flow direction in the Bar 15 reach provide a potential explanation for the low number of tracers mobilized.

Pathlength distances (L) were calculated as the distance travelled by recovered mobilized tracers (moved >10m downstream from the initial seeding site), for the three study reaches. Average pathlength distances ($\bar{L}$) and median pathlength distances (L_m) were used in the analyses, to account for expected skewed distributions (Table 6). Overall, average pathlength distances for the 2019-20 year ranged from 306.2m - 393.8m for the three study reaches, which are well-above average pathlength distances of previous tracers deployed in the San Juan River (Table 6) (McQueen, 2019).

Average pathlength distances ($\overline{(L)}$) of recovered surface tracers for the 2020-21 tracer deployment season were lower, ranging from 139.4m – 253.3m for the three study reaches. Amongst grain size classes, $\bar{L}$ tended to follow a decreasing trend with increasing grain size class for both deployment years and all study reaches, with few exceptions (Table 7). Mobilized tracers at the Bar 15 reach for the 2020-21 deployment year appear to deviate from this trend, as the second largest grain size class of tracers (45-64mm) had the highest pathlength distances ($\bar{L}$ = 298.6m). However, only two 45-64mm tracers were mobilized, which does not accurately represent tracer pathlengths of this size class when compared to the other study reaches and previous deployment years (Table 7).

Table 7. Mobility (F_m) and pathlength distances (L) of recovered surface tracers.

Year	Grain Size (mm)	Bar 6					Bar 7					Bar 15				
		N_r	R (%)	F_m	$\bar{L}$ (m)	L_m (m)	N_r	R (%)	F_m	$\bar{L}$ (m)	L_m (m)	N_r	R (%)	r_m	$\bar{L}$ (m)	L_m (m)
2019-20	22-32	18	64	1	352.1	148.2	20	77	.95	468.5	435.6	16	64	1	426.3	433.2
	32-45	12	42	1	357	287.6	17	71	1	409.1	444.2	16	67	1	462.7	437.1
	45-64	20	74	1	298.7	250.4	24	96	1	342.2	370.7	21	84	1	314.2	277.2
	64-90	14	61	1	206.2	95.1	22	88	.91	371.7	412.5	18	75	1	201	148
	> 90	-	-	-	-		-	-	-	-		4	57	.70	106.4	125.3
2020-21	22-32	13	50	1	205.3	188	20	80	.95	278.6	220.1	14	56	.64	172.4	122.2
	32-45	15	60	1	167.3	68.7	17	65	1	314.7	327.9	28	82	.39	171.5	123.6
	45-64	12	48	.92	112.8	67.7	20	83	.95	231.5	237.8	13	81	.15	298.6	298.6
	64-90	20	83	1	142.6	84.2	17	68	.94	165.6	185.4	21	84	.14	64.8	32.2

5.4.4 Discharge effects on mobility and pathlength distance

The fraction of recovered mobile tracers (F_m) for the 2019-20 and 2020-21 deployment years were analyzed, along with three years of past tracer data, against three different flow metrics to better understand the influence of flow. To investigate, a simple linear regression was performed, using the three different flow metrics as predictor variables; total excess energy expenditure (Ω_T), peak event excess energy expenditure (Ω_P), and maximum peak discharge (Q_p) (Table 5). The three predictor variables were tested against the F_m in each study reach, for a total of five deployment years.

The linear fit between F_m and all three flow metrics in the Bar 6 and Bar 7 reach was weak. However, the F_m at the Bar 6 and Bar 7 study reaches was better correlated to peak event excess

energy expenditure (Ω_P) (Bar 6: $R^2 = 0.25$, p = 0.39; Bar 7: $R^2 = 0.16$, p = 0.51) and maximum peak discharge (Q_p) (Bar 6: $R^2 = 0.26$, p = 0.38; Bar 7: $R^2 = 0.18$, p = .47) than to total excess energy expenditure (Ω_T) (Bar 6: $R^2 = 0.11$, p = 0.58; Bar 7: $R^2 = 0.04$, p = 0.75) (Figure 21). All three flow metrics were good predictors of F_m in the Bar 15 reach with (Ω_T) yielding the strongest correlation ($R^2 = 0.71$, p = 0.07). Results of Ω_P ($R^2 = 0.57$, p = 0.14) and Q_p ($R^2 = 0.66$, p = 0.09) show similar, relatively strong, correlation to F_m in the Bar 15 reach. The slopes of the linear fit between the three flow metrics and F_m in the Bar 15 reach ($\Omega_T = 0.0027$, $\Omega_p = 0.0027$, $Q_p = 0.0010$) differed from the slopes of Bar 6 ($\Omega_T = 0.00014$, $\Omega_p = 0.00024$, $Q_p = 0.00015$) and Bar 7 ($\Omega_T = 0.000079$, $\Omega_p = 0.00017$, $Q_p = 0.00011$) suggesting a different relationship between F_m and the influence of flow between these reaches.

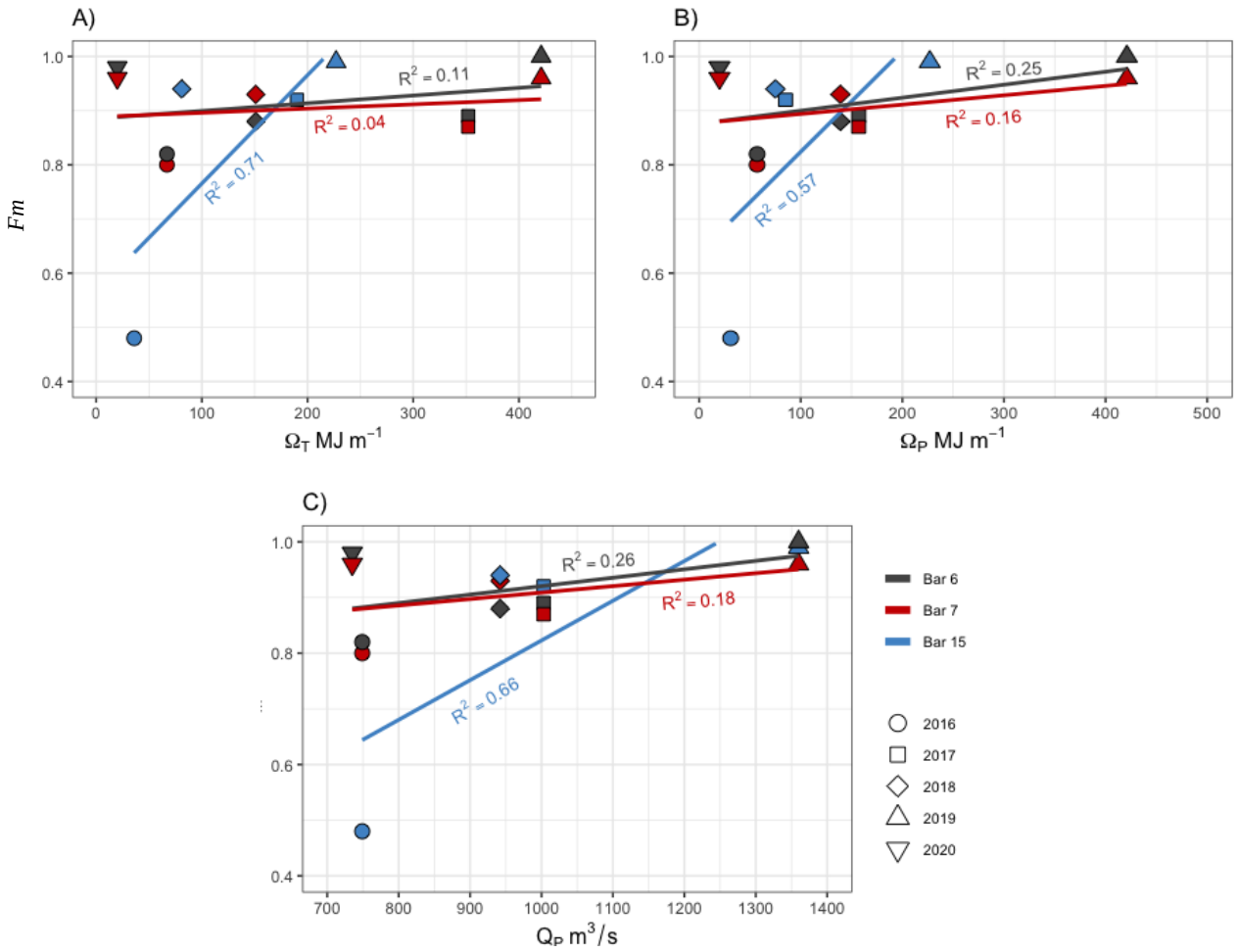

Figure 21. Mobility (F_m) of surface tracers at the three study reaches plotted against A: total excess flow energy (Ω_T); B: peak event excess flow energy (Ω_P); C: maximum peak discharge (Q_P).

The relationship between F_m in the Bar 6 and Bar 7 study reach and all three flow metrics appears to be weak. However, peak flood events led to near full mobilization of recovered tracers for all five deployment years in these reaches. Therefore, any differences in both peak flows and flow duration between years in the Bar 6 and Bar 7 study reach could not lead to significant changes in F_m. At a smaller temporal scale and larger range of flows, mobility at these reaches may be better predicted; however results from this study suggest mobilizing events have roughly the same effect on mobility regardless of magnitude and duration.

Bar 15 had greater variation in mobility (F_m) between deployment years, with $\Omega_{T,}$ the variable that takes into account both peak flows and flow duration, being the strongest predictor variable. Although, linear fits of all three metrics had similar explained variation (R^2) in relation to F_m in the Bar 15 study reach. The apparent 'strength' (high R^2 values) in the relationship between the three flow metrics and F_m at the Bar 15 study reach is most likely influenced by the abnormally low mobility seen in the 2016 tracer results (McQueen et al., 2021). McQueen et al. (2021) suggested the anomaly was in part due to local morphodynamics and lower $\Omega_{T.}$ Aside from the extreme high and low F_m values in the Bar 15 study reach, the relationship between flow and tracer mobility appears to be weak. Overall, there is a considerable amount of variation in F_m that is left unexplained by the influence of all three flow metrics.

Grain size distributions (number of tracers of each grain size class) were similar between deployment years and thus, it is unlikely that the influence of grain size could explain any differences in F_m between years. However, differences in seeding locations, as well as annual morphologic change to the channel, may have led to restructuring in the local bed morphology between years. This suggests that differences in bed texture at deployment sites may be able to explain the variation in F_m in the three study reaches that is left unexplained from the flow analysis. However, changes in the local bed texture at deployment sites, influenced by annual flood events, could not be properly identified in this study. Therefore, differences in channel morphology between and within deployment years may explain variation in mobility between and within reaches, although empirical evidence is needed.

Median pathlength distances (L_m) of recovered surface tracers were analyzed with previous tracer results (2015-2018) in the San Juan River (McQueen, 2019; McQueen et al., 2021) in relation to

the three flow metrics. Average pathlength distances ($\overline{L}$) rather than median, of recovered surface tracers were also analyzed with the three flow metrics, and produced similar results. However, median pathlength distances better account for skewness in the data's distribution and was chosen to best interpret the influence of flow on pathlength distances.

The relationship between pathlength distances and flow was first assessed by study reach. Median pathlength distances (L_m) were weakly correlated to total excess energy expenditure (Ω_T) for both Bar 6 and Bar 7, but yielded a strong significant relationship for Bar 15 (Bar 6: $R^2 = 0.49$, $p = 0.12$; Bar 7: $R^2 = 0.19$, $p = 0.26$; Bar 15: $R^2 = 0.99$, $p = < 0.001$) (Figure 22). Both peak event excess flow energy expenditure (Ω_P) (Bar 6: $R^2 = 0.56$, $p = 0.09$; Bar 7: $R^2 = 0.66$, $p = 0.06$; Bar 15: $R^2 = 0.64$, $p = 0.07$) and maximum peak discharge (Q_P) (Bar 6: $R^2 = 0.67$, $p = 0.06$; Bar 7: $R^2 = 0.63$, $p = 0.07$; Bar 15: $R^2 = 0.75$, $p = < 0.05$) yielded a stronger relationship to median pathlength distance for both the bar 6 and bar 7 study reaches (Figure 22).

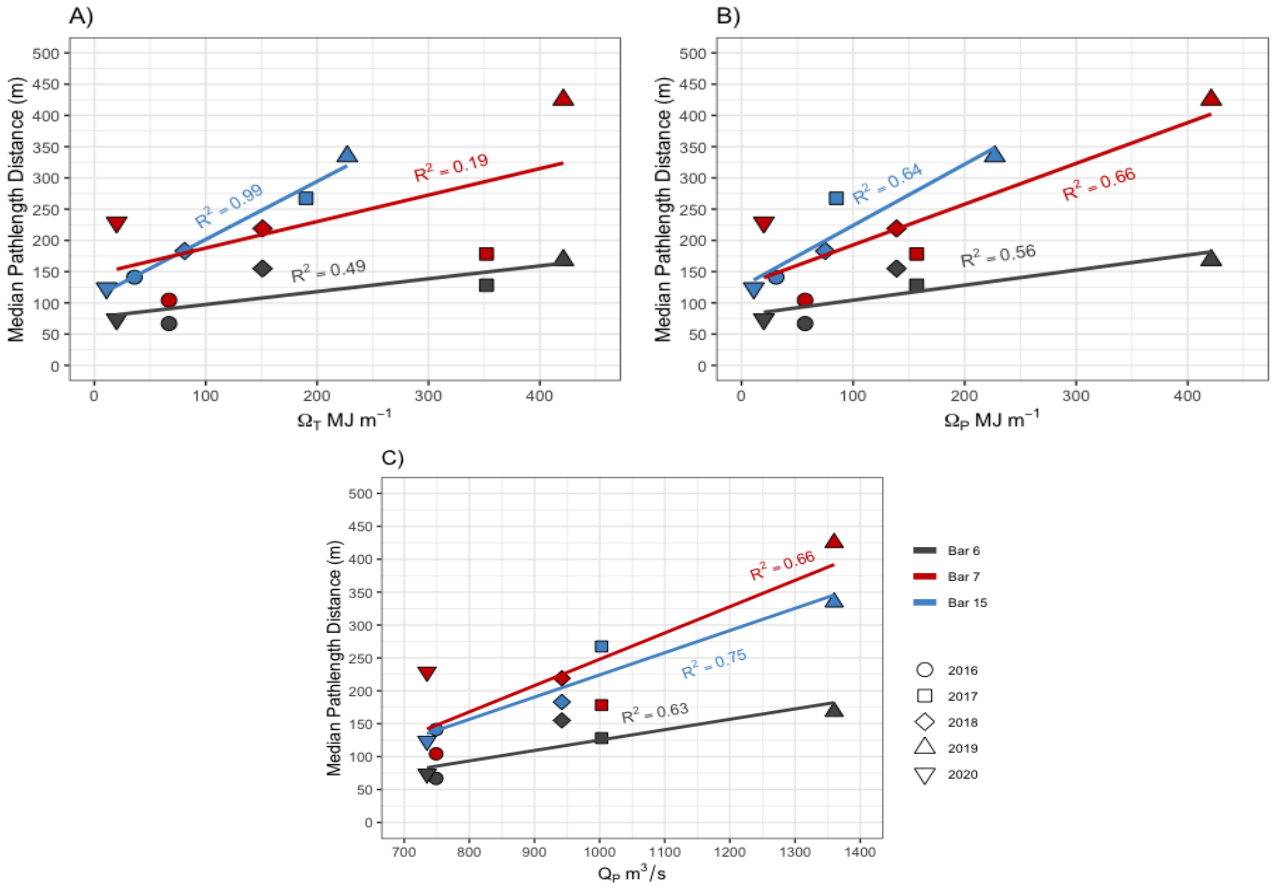

Figure 22. Median pathlength distances (m) of surface tracers at the three study reaches plotted against A: total excess flow energy (Ω_T); B: peak event excess flow energy (Ω_P); C: maximum peak discharge (Q_P).

In contrast to tracer mobility, pathlength distances showed high correlation to the three flow metrics for two of the three study reaches, with the exception of Bar 7 pathlength distances relating to Ω_T. However, aside from the extreme high and low flow values, the relationship between flow and median pathlength distances is less clear, indicating that distances are similar for the majority of flows with the exception of extreme low and high flood years (Figure 22). For Bar 6 and Bar 7 the weakest correlation was Ω_T, suggesting that flow duration has minimal influence on tracer pathlength distances for the two study reaches. Bar 15 yielded a strong relationship between pathlength distances and Ω_T but were weakly correlated to the other two flow metrics. Surprisingly, four separate flood events above bankfull in 2017, including the second highest peak discharge event (Q_p = 1,003m^3 s^{-1}), did not lead to substantially higher pathlength distances when compared to other years that experienced lower magnitude flows and had a smaller number of flood events (Table 5; Figure 22).

Overall, there is positive trend seen, with higher peak flows leading to greater pathlength distances. The number and duration of events above bankfull (Ω_T) may be a less important influence on pathlength distances compared to the magnitude and duration of the peak flood event. Additionally, median pathlength distances differed between study reaches subject to the same flow events, even during years with high peak flood events, reflected in the variation in slope of linear fit between sites for all three metrics (Figure 22). Furthermore, Bar 15 yielded a strong relationship to Ω_T and saw weaker relationships to both Ω_P and Q_p, suggesting that the Bar 15 reach may be more influenced by flow duration. This relationship may be caused by the Bar 15 reach having a less morphologically-complex channel, relative to the other two reaches. As well, the deployment location at the Bar 15 reach did not change across all five years. This allowed for a more accurate estimate of the influence of flow variables, controlling for other factors, such as morphological differences, at the location tracers were initially entrained. Bar 6 and 7 study reaches had less variation explained by the three flow metrics, which is perhaps due to differences in initial seeding sites between study years that are not accounted for.

Median pathlength distances (L_m) were morphologically-scaled to the bar length to assess the overall relationship between pathlength distances and both Ω_T and Ω_P. The relationship between pathlength distances and Q_p was not assessed as this metric did not change between sites. Scaled median pathlength distances were weakly correlated to both (Ω_T) (R^2 = 0.22, p = < 0.05) and (Ω_P)

(R^2 = 0.34, p = < 0.05) (Figure 23). Comparable to the results assessed by study reach, a stronger correlation is seen for Ω_P, supporting the idea that the magnitude and duration of a peak flood event has a greater influence on pathlength distances of individual particles, rather than the total magnitude and duration of flood events above bankfull within each winter flooding season. The weaker correlation seen when assessing the influence of flow for all three study reaches combined, also supports the idea that pathlength distances differ significantly at the reach scale, suggesting a strong morphological influence on particle dispersion. Furthermore, maximum pathlength distances rarely exceeded one bar length even in the 2019-20 study year, affected by the 100-year flood event. This points to a larger-scale morphological constraint on pathlength distances that may explain some of the variation seen when analyzing the relationship between pathlength distances and flow.

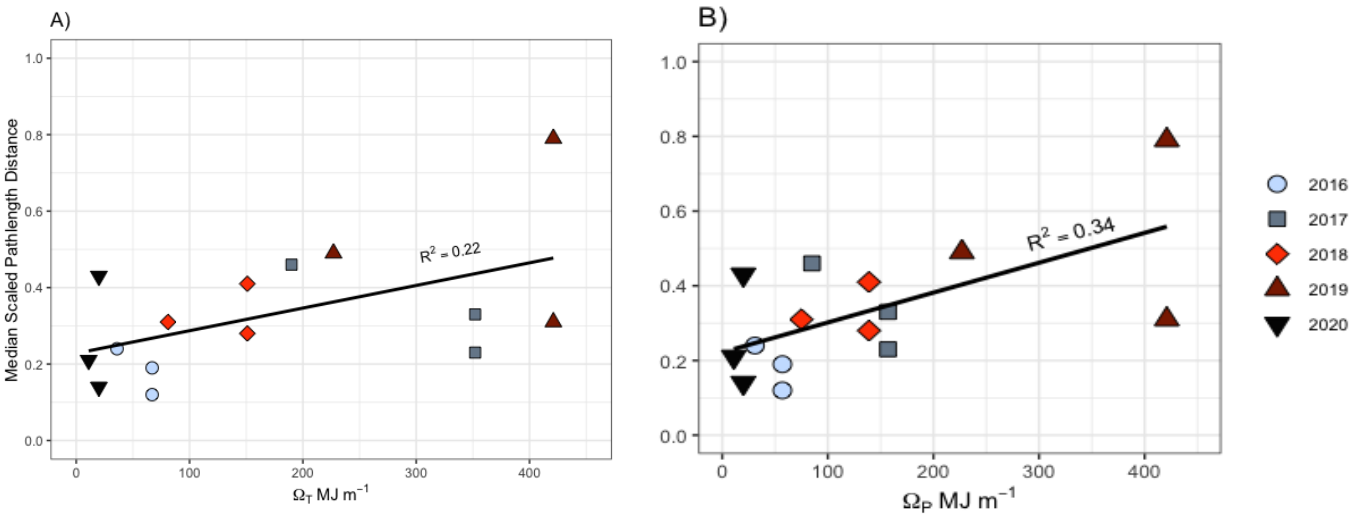

Figure 23. Median pathlength distances (m) of surface tracers scaled by bar length plotted against A: total excess flow energy (Ω_T); B: peak event excess flow energy (Ω_P).

5.4.5 Grain Size Effects on Pathlength Distance

The effects of grain size on pathlength distances (L) were also analyzed. The Shapiro-Wilk test was used to assess the normality of the data for both study years. Data did not fit normal distributions (p = < 0.05). The Kruskal-Wallis (K-W) test, which is used for data that does not follow a normal distribution, was chosen to assess for differences in pathlength distances between grain size classes. Pathlength distances were morphologically-scaled to the bar length to normalize data between gravel bar reaches and were further analyzed by individual gravel bar study site for

the 2019-20 and 2020-21 study years to assess differences between grain size groups at the reach scale. Individual study reach data did not fit normal distributions (p = < 0.05), therefore the K-W test was also used for this analysis.

For the 2019-20 deployment year, pathlength distances were compared between five grain size groups (22-32mm, 32-45mm, 45-64mm, 64-90mm, and > 90mm). The largest grain size group (> 90mm) had a very small sample size (N = 3), therefore results for this grain size group were interpreted with caution. There was a statistically significant difference between grain size groups and pathlength distances for the 2019-20 study year (Chi-Square = 20.909, D.F = 4, and P = < 0.001) (Figure 24). A post-hoc Dunn test was used to test pairwise differences between groups. The Dunn test indicated that there are significant differences in pathlength distances between 22-32mm and 45-64mm (P = < 0.05), 32-45mm and 45-64mm (P = < 0.05), 22-32mm and 64-90mm (P = < 0.01), 32-45mm and 64-90mm (P = < 0.05), 22-32mm and > 90mm (P = < 0.05), and 32-45mm and > 90mm (P = < 0.05). The results show that significant differences in pathlength distances are between the smallest two grain size groups and the largest three grain size groups (Figure 24). Although the Benjamini-Hochberg method was used in the post-hoc Dunn test to reduce the false discovery rate and adjust p-values, significant results for the largest (>90mm) grain size group may not be accurate due to underrepresentation from the extremely small sample size recovered. Overall, the influence of grain size for the 2019-20 study year is significant, with decreasing pathlength distances with increasing grain-size of tracers.

For the 2020-21 study year, pathlength distances were compared between four grain size groups (22-32mm, 32-45mm, 45-64mm, and 64-90mm) (Figure 24). There was no statistically significant difference between grain size groups and pathlength distances for the 2020-21 study year (Chi-Square = 3.460, D.F = 3, and P = 0.326) (Figure 24). Data did not show any significant trends of decreasing pathlength distances with increasing grain-size. Weak trends do appear, with the smallest grain size group (22-32mm) having the greatest median pathlength distance ($L_{\mathbf{m}}$ = 213m) and the largest grain size group (64-90mm) resulting in the lowest ($L_{\mathbf{m}}$ = 96m). However, the trend becomes less evident beyond the smallest and largest grain size groups. The third largest grain size group (45-64mm) had a very similar pathlength distance to the smallest grain size group ($L_{\mathbf{m}}$ = 202m), and much greater than the second smallest grain size group (32-45mm) ($L_{\mathbf{m}}$ = 124m). Overall, grain size appears to have little influence on pathlength distances for the 2020-21 study

year, which saw a much smaller peak flood event (Q_p = 735m^3 s^{-1}) and overall less hydrological activity than the previous year. For the 2019-20 deployment that experienced a 100-year flood event (Q_p = 1360m^3 s^{-1}), resulting in greater travel distances across all study reaches, we are able to see a more evident influence of grain size. To assess the influence of grain size further, pathlength distances were also compared by study reach.

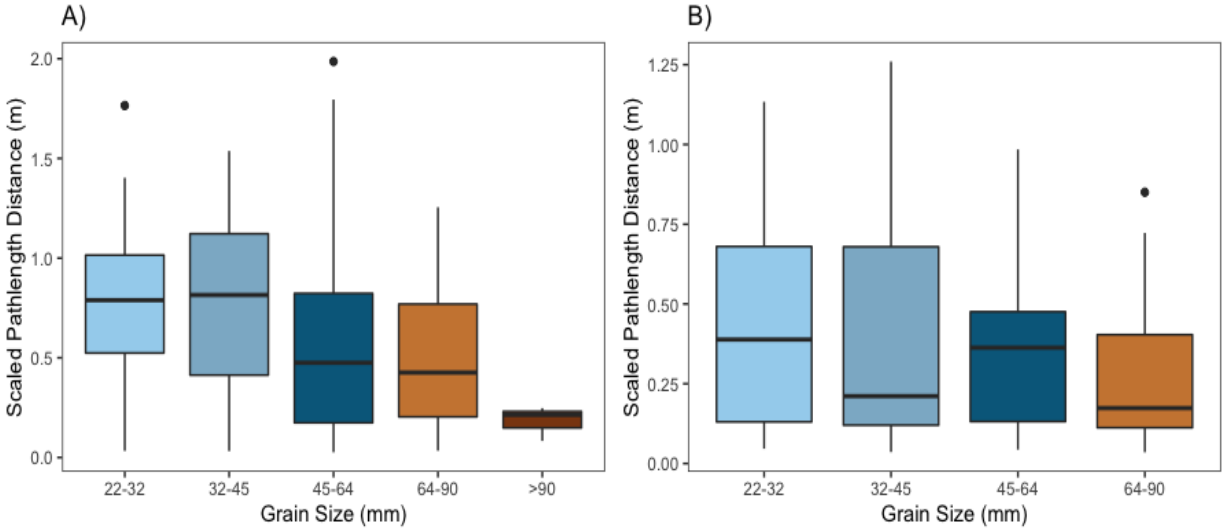

Figure 24. Scaled pathlength distance (m) by grain size class (mm) for A: 2019-20 study year and B: 2020-21 study year

Boxes represent the first and third quartile, the median is depicted by the black centre line of the boxes. Whiskers represent the minimum and maximum pathlength distance with block dots representing outliers.

For the 2019-20 study year, pathlength distances were compared between four grain size groups (22-32mm, 32-45mm, 45-64mm, and 64-90mm) for both the Bar 6 and Bar 7 study reaches (Figure 25). Bar 15 had an additional set of coarse tracers (> 90mm) for the 2019-20 deployment year so pathlength distances were between five grain size groups (22-32mm, 32-45mm, 45-64mm, and 64-90mm, and >90mm). There was no statistically significant difference between grain size groups and pathlength distances for Bar 6 (Chi-Square = 3.170, D.F = 3, and P = 0.366) and Bar 7 (Chi-Square = 5.122, D.F = 3, and P = 0.163) (Figure 25). However, there was a significant difference between grain size groups and pathlength distances for Bar 15 (Chi-Square = 21.644, D.F = 4, and P = < 0.001) (Figure 25). A post-hoc Dunn test revealed statistically significant differences in pathlength distances between 22-32mm and 64-90mm grain size groups (P = < 0.01) and between 32-45mm and 64-90mm grain size groups (P = < 0.01). There were also significant differences between the two smallest grain sizes (22-32mm and 32-45mm) and > 90mm grain size (P = < 0.05);

however as previously mentioned, the small sample size (N = 3), may not accurately represent pathlength distances for this grain size. At the 90% confidence level, there were statistically significant differences between 22-32mm and 45-64mm grain size groups (P = < 0.10) and between 32-45mm and 45-64mm grain size groups (P = < 0.10).

A weak trend of decreasing pathlength distances with increasing grain size can be seen between the smallest and largest grain size groups for the Bar 6 study reach (Figure 25). No trends appear for the Bar 7 study reach for the 2019-20 year, with similar pathlength distances seen across all grain size groups (Figure 25). Disregarding the largest grain size group (> 90mm), Bar 15 still shows a very strong trend of decreasing pathlength distance with increasing grain size (Figure 25C). Of the three gravel bar study reaches, Bar 15 exhibits the least complex morphology, thus it is possible that the influence of grain size will be most apparent; whereas channel morphology may have a more dominant role in controlling pathlength distances for the Bar 6 and Bar 7 study reach.

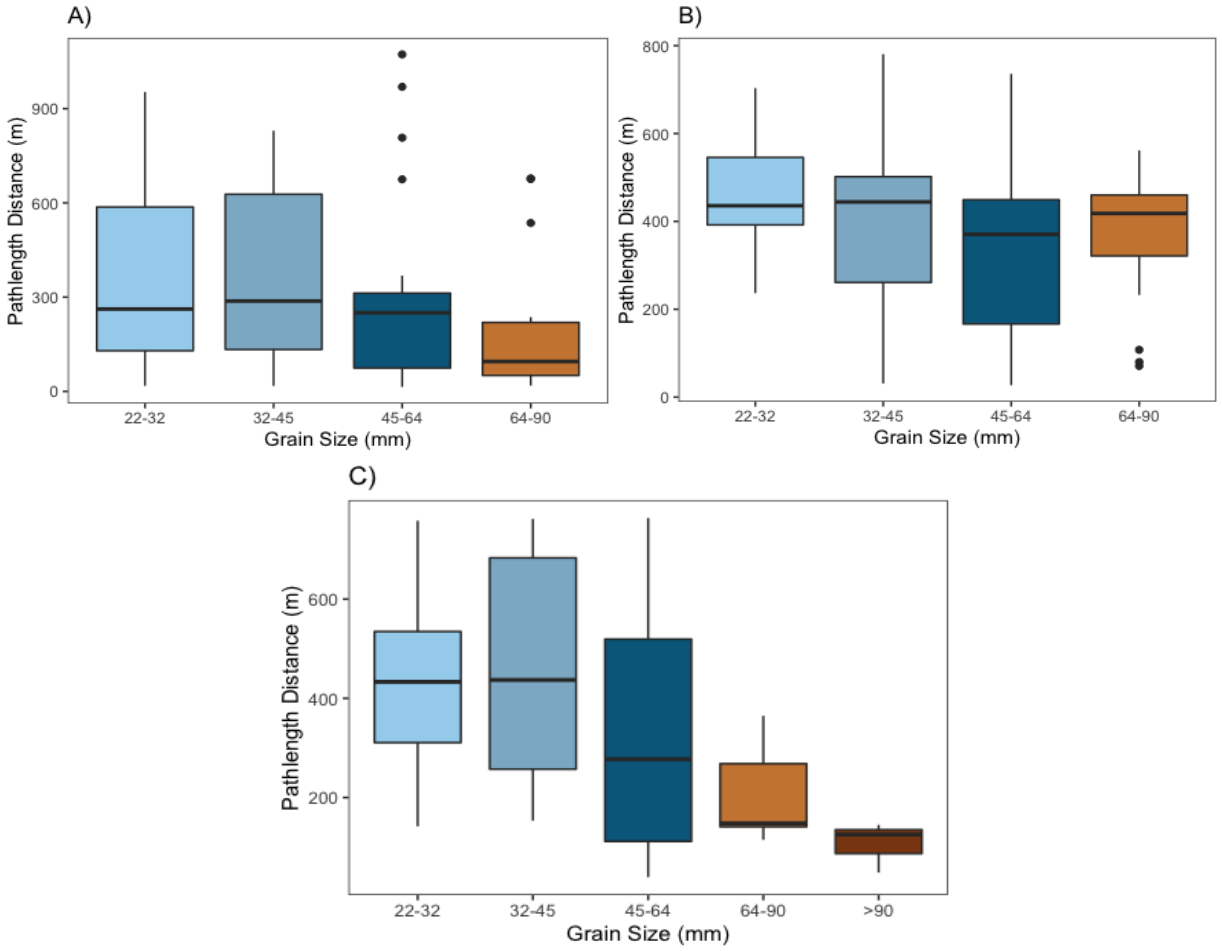

Figure 25. Pathlength distance (m) grouped by grain size class (mm) for A: Bar 6 2019-20 study year; B: Bar 7 2019-20 study year and; C: Bar 15 2019-20 study year.

For the 2020-21 deployment, pathlength distances (*L*) were compared between four grain size groups (22-32mm, 32-45mm, 45-64mm, and 64-90mm) for the three study reaches. There were no statistically significant difference between grain size groups and pathlength distances for Bar 6 (Chi-Square = 2.506, D.F = 3, and P = 0.474), Bar 7 (Chi-Square = 4.227, D.F = 3, and P = 0.238), and Bar 15 (Chi-Square = 2.575, D.F = 3, and P = 0.462). There appears to be a weak trend of decreasing *L* with increasing grain size for Bar 6, with the smallest grain size group (22-32mm) having significantly greater pathlength distances relative to the three larger grain size groups (Figure 26). No trends are apparent for both the Bar 7 and Bar 15 study reaches for the 2020-21 deployment. Furthermore, Bar 15 pathlength distances between grain size groups shows an surprising relationship, with the third largest grain size group having the greatest L_m. However, due

to low recovery rates of the larger grain size groups at the Bar 15 study reach, the sample size for both the 45-64mm (N = 2) and 64-90mm tracers (N = 3) were extremely small and most likely does not accurately represent relative pathlength distances for these grain size classes. Overall, for the 2020-21 study year, the influence of grain size on pathlength distances of tracers appears to be negligible.

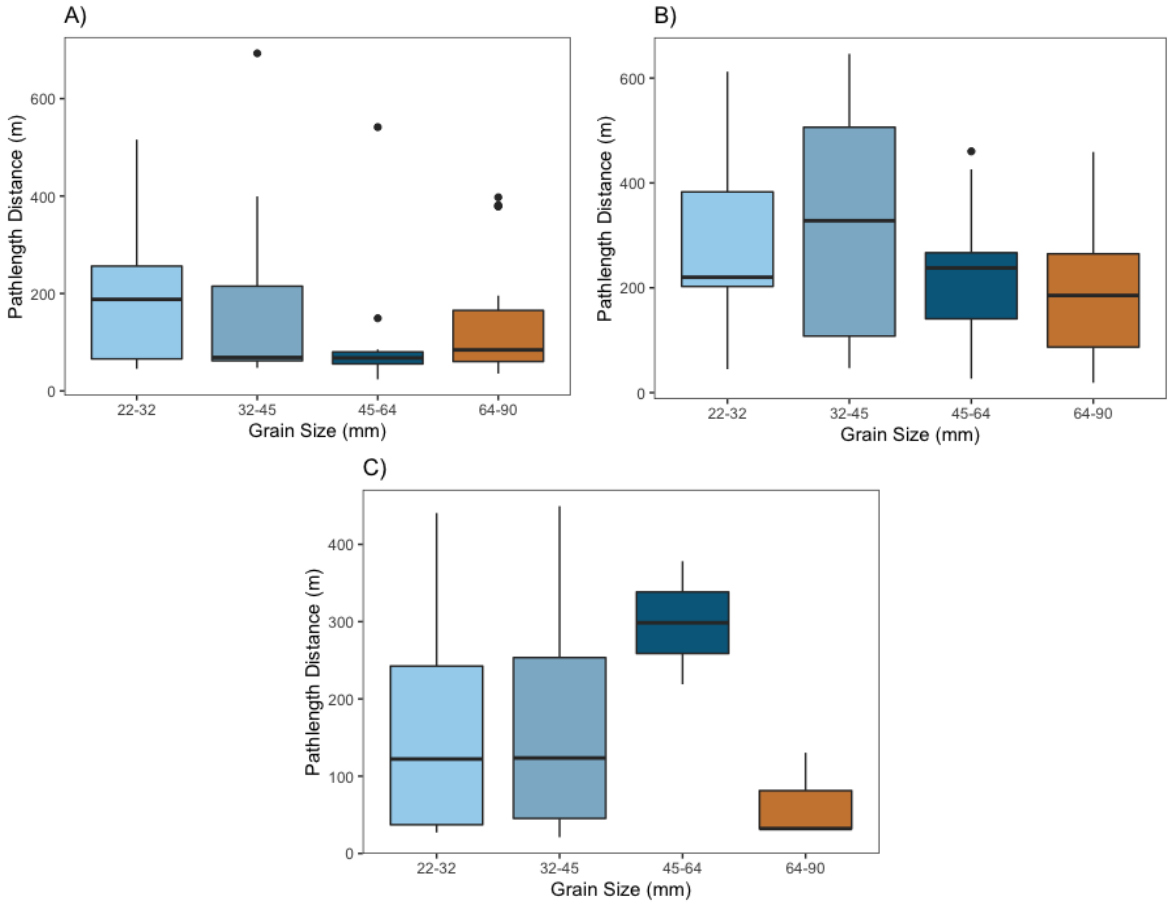

Figure 26. Pathlength distance (m) grouped by grain size class (mm) for A: Bar 6 2020-21 study year; B: Bar 7 2020-21 study year and; C: Bar 15 2020-21 study year.

In summary, results indicate that pathlength distances are weakly influenced by grain size during years with lower peak flood events and limited hydrological activity. Furthermore, the 2019-20 study year subject to a 100-year flood event saw differences in the effects of grain size between study reaches, suggesting the relationship between grain size and pathlength distance may vary due to the dominant role of channel morphology, especially in reaches that have more complex

morphological features.. To further understand pathlength dispersion of recovered tracers, pathlength distributions can be explored.

5.4.6 Pathlength Distributions

Tracer pathlength distributions were binned into 50m intervals to visualize tracer frequency distributions within and between macroforms (length of the gravel bar) to interpret final tracer positions relative to meso-scale morphological units in the reach. Frequency distributions of Bar 7 and Bar 15 pathlengths from previous tracer deployments on the San Juan River (McQueen, 2019) were also re-analyzed to further understand the influence of morphology on pathlength distributions, with relative deployment locations from all years being in close proximity (< 50m). Distributions for Bar 6 could not be compared to previous deployment years, as earlier deployment locations (2015-18) were located at the head of Bar 6, ~500m upstream. Aerial imagery from collected LIDAR data. in the summer of 2019 is used to display recovery locations for the 2019-20 tracer deployment. Aerial imagery from LIDAR data which was also collected by Terra Remote Sensing Inc in March (2021) and is used to display recovery locations for the 2020-21 tracer deployment. It is important to note that the 2019 imagery shows recovery locations relative to the channel at the time of deployment (Fall 2019), therefore they do not capture channel changes that occurred during the 2019-2020 winter flooding period. As well, the 2021 aerial imagery was collected earlier than usual, at higher flows, and the gravel bars are more inundated compared to the 2019 imagery, making comparison and interpretation problematic.

Bar 6

Both the 2019 and 2020 deployments of surface tracers at the Bar 6 study reach were seeded at the tail of Bar 6 at pool tail-out locations (Figure 27). The Bar 6 deployment location for the 2020-21 deployment was moved ~10m downstream to a new pool-tailout location because of changes to the channel morphology (Figure 27). Bar 6 pathlength distributions from both the 2019 and 2020 deployment display a right-skewed multi-modal distribution with $\bar{L}$ greater than $L_{\mathbf{m}}$ (Figure 27; Figure 28). The majority (>50%) of the tracers did not move past the large bend at Bar 6X in both deployment years (Figure 27). This may also explain the low recovery rate for Bar 6 deployment, with a large number of tracers potentially being trapped in the deep pool ~200m downstream at undetectable water and/or sediment depths due to infilling of the pools.

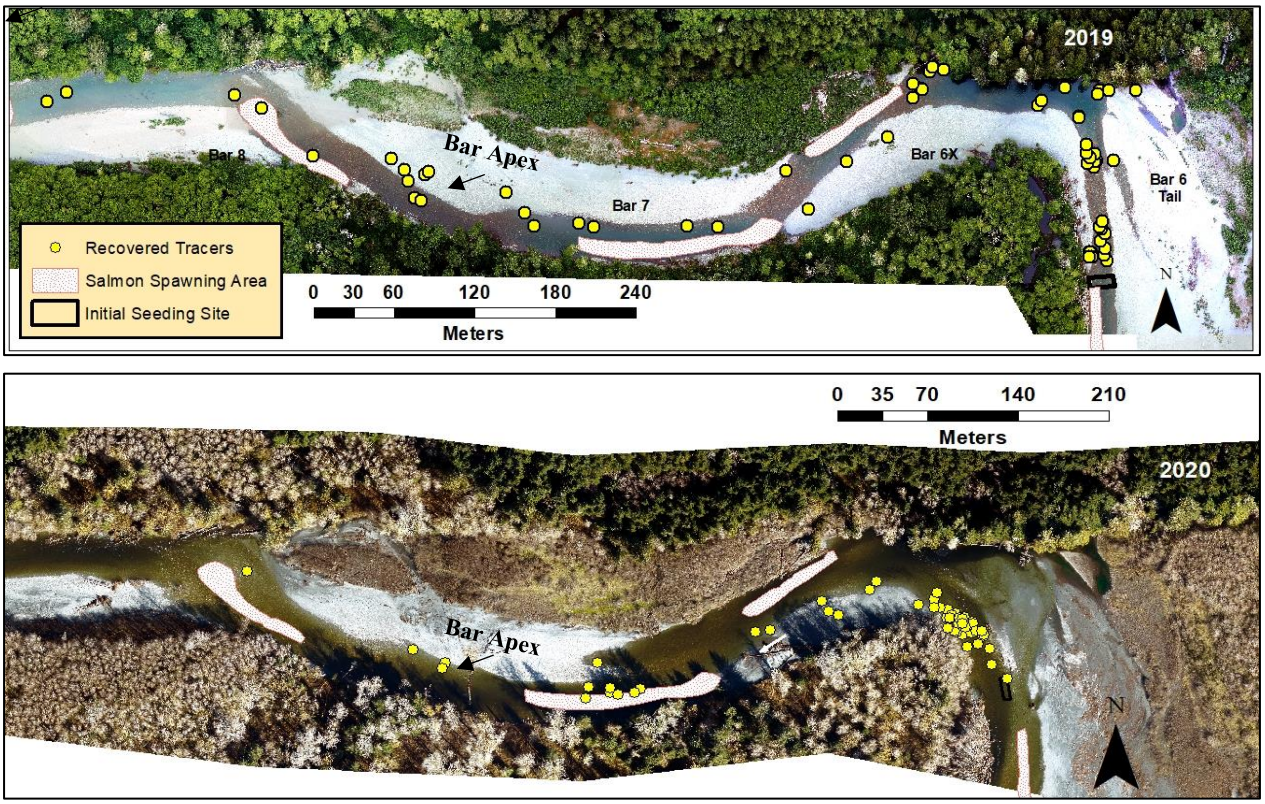

Figure 28. Recovered tracers deployed at the Bar 6 study reach for the 2019-20 year (top) and 2020-21 year (bottom). Flow right to left.

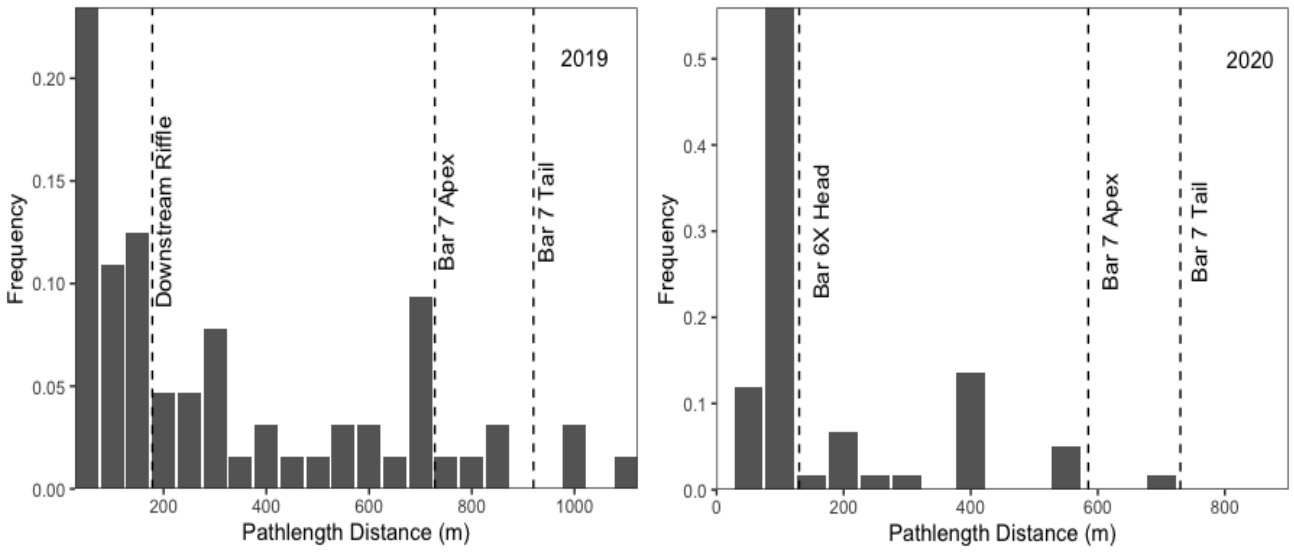

Figure 27. Pathlength distributions for recovered tracers at the Bar 6 study reach for the 2019-20 study year (Left) and 2020-21 study year (right).

Both the 2019 and 2020 deployments of surface tracers at the Bar 6 study reach were seeded at the tail of Bar 6 at pool tail-out locations (Figure 27). The Bar 6 deployment location for the 2020-21 deployment was moved ~10m downstream to a new pool-tailout location because of changes to the channel morphology (Figure 27). Bar 6 pathlength distributions from both the 2019 and 2020 deployment display a right-skewed multi-modal distribution with $\bar{L}$ greater than $L_{\mathbf{m}}$ (Figure 27). The majority (>50%) of the tracers did not move past the large bend at Bar 6X in both deployment years (Figure 27; Figure 28). This may also explain the low recovery rate for Bar 6 deployment, with a large number of tracers potentially being trapped in the deep pool ~200m downstream at undetectable water and/or sediment depths due to infilling of the pools.

For the 2019 deployment, the first mode coincides with the location of the nearest downstream riffle (~50m), where the largest fraction of tracers were deposited (Figure 28). There were two modes associated with tracers that moved past the Bar 6X bend. The second mode is associated with a small number of tracers that were deposited near the pool tail-out adjacent to Bar 6X (Figure 27; Figure 28). The last mode represents the farthest downstream site of significant tracer deposition located at the Bar 7 apex, specifically along the channel margin, which is also a site of major deposition for tracers seeded at Bar 7 in the 2019-20 deployment (Figure 27). High tracer deposition at the Bar 7 apex can be attributed to reach-scale downstream migration and lateral growth of the gravel bar (Figure 27; Figure 28).

For the 2020-21 deployment, that had a much lower peak flood event than the 2019-20 deployment, tracers moved shorter distances. The first mode represents a significant deposition site for tracers (>60%) at the Bar 6X head (Figure 27; Figure 28). This was also an area of tracer deposition for the previous deployment, although a greater number of tracers were deposited at the Bar 6X head for the 2020-21 deployment. The second mode is associated with deposition at the Bar 7 head, with 10% of tracers being deposited in this area (Figure 27; Figure 28). There was also a small number of tracers deposited at the Bar 7 apex, which represents the farthest downstream depositional area (mode) for the 2020-21 deployment (Figure 27). Fewer tracers travelled far enough to become trapped at the Bar 7 apex for the 2020-21 deployment, which may be attributed to the lower peak flood event that occurred, compared to the previous 2019-20 deployment (Figure 27).

Hydrological activity (all flood events above bankfull), as well as the peak flood event were considerably different between the two deployment years. This may explain the differences seen in pathlength distributions between the two deployments, with a greater proportion of recovered tracers moving less than 200m downstream of the initial deployment location for the 2020-21 deployment. However, depositional areas where tracers seem to become trapped were consistent for both years, with tracers being deposited at the Bar 6X head, and Bar 7 apex in both deployments. This indicates a strong morphological control on pathlength distances at the reach scale. The 2019-20 deployment at the Bar 6 study reach also had the farthest distance travelled (1072m) by any tracer across the three study reaches and five years of tracer deployment on the San Juan River, which may be influenced by the 100-year flood event (Figure 27).

Bar 7

Both deployment locations at the Bar 7 study reach were adjacent to Bar 6X, at pool tailout locations, slightly upstream of the Bar 7 head (Figure 29). The 2020-21 deployment location was moved ~30m upstream to a new pool tailout location because of channel changes. Deployment locations for previous tracer work on the San Juan River (2015 - 2018) at the Bar 7 study reach were ~20m downstream of the 2019-20 deployment location (McQueen, 2019). Deployment strategy for the previous deployments (2015-2018) placed tracers in both the wetted channel and dry gravel bar, which may influence pathlength distributions compared to the deployment strategy used for this study.

Pathlength distributions for the 2019-20 deployment year at the Bar 7 study reach followed a roughly symmetrical distribution, with the primary mode occurring at the Bar 7 apex, where roughly half of recovered tracers were found (Figure 29; Figure 30). A greater number of tracers exceeded one riffle-pool-bar unit during the 2019-20 deployment at the Bar 7 study reach, relative to the other two study reaches for all deployment years. This can be attributed to the extreme flood event that occurred in January 2020. Furthermore, significant bank erosion at the Bar 6 and Bar 7 study reach suggests that channel changes were greater during the 2019 deployment of tracers, and is reflected in the high mobilization and greater pathlength distances of tracers at the Bar 7 study reach for the 2019-20 deployment.

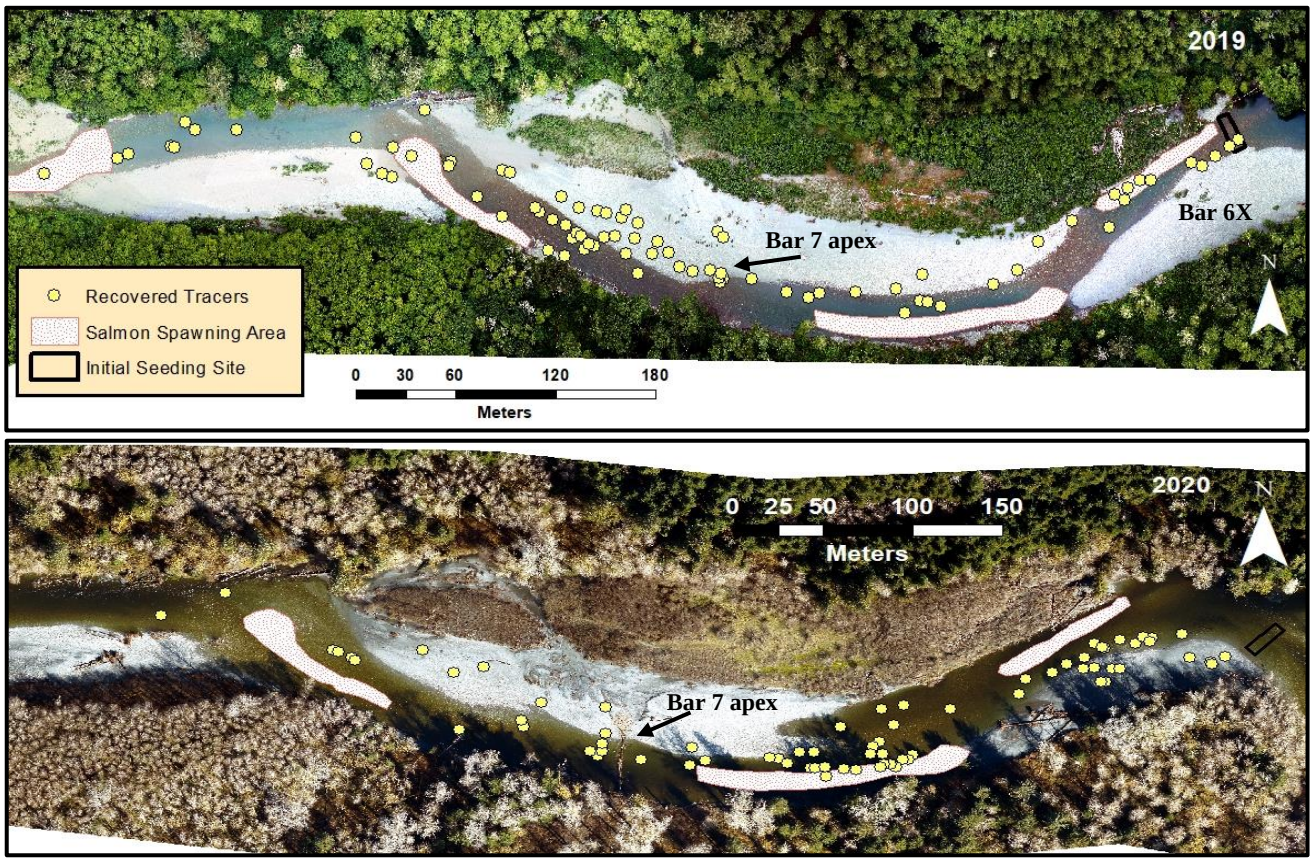

Figure 29. Recovered tracers deployed at the Bar 7 study reach for the 2019-20 year (top) and 2020-21 year (bottom). Flow right to left.

Tracer pathlength results from the 2020-21 deployment followed a right-skewed distribution, with four distinct modes (Figure 30). The majority of tracers travelled short distances and deposited at the Bar 6X apex, slightly downstream from the seeding site, representing the first mode (Figure 29; Figure 30). The second mode saw the largest proportion of tracers (~ 40%) deposited at Bar 7 head (Figure 29; Figure 30). A smaller proportion of tracers were deposited at both the Bar 7 apex and tail, representing the third and fourth modes of pathlength distributions (Figure 29; Figure 30).

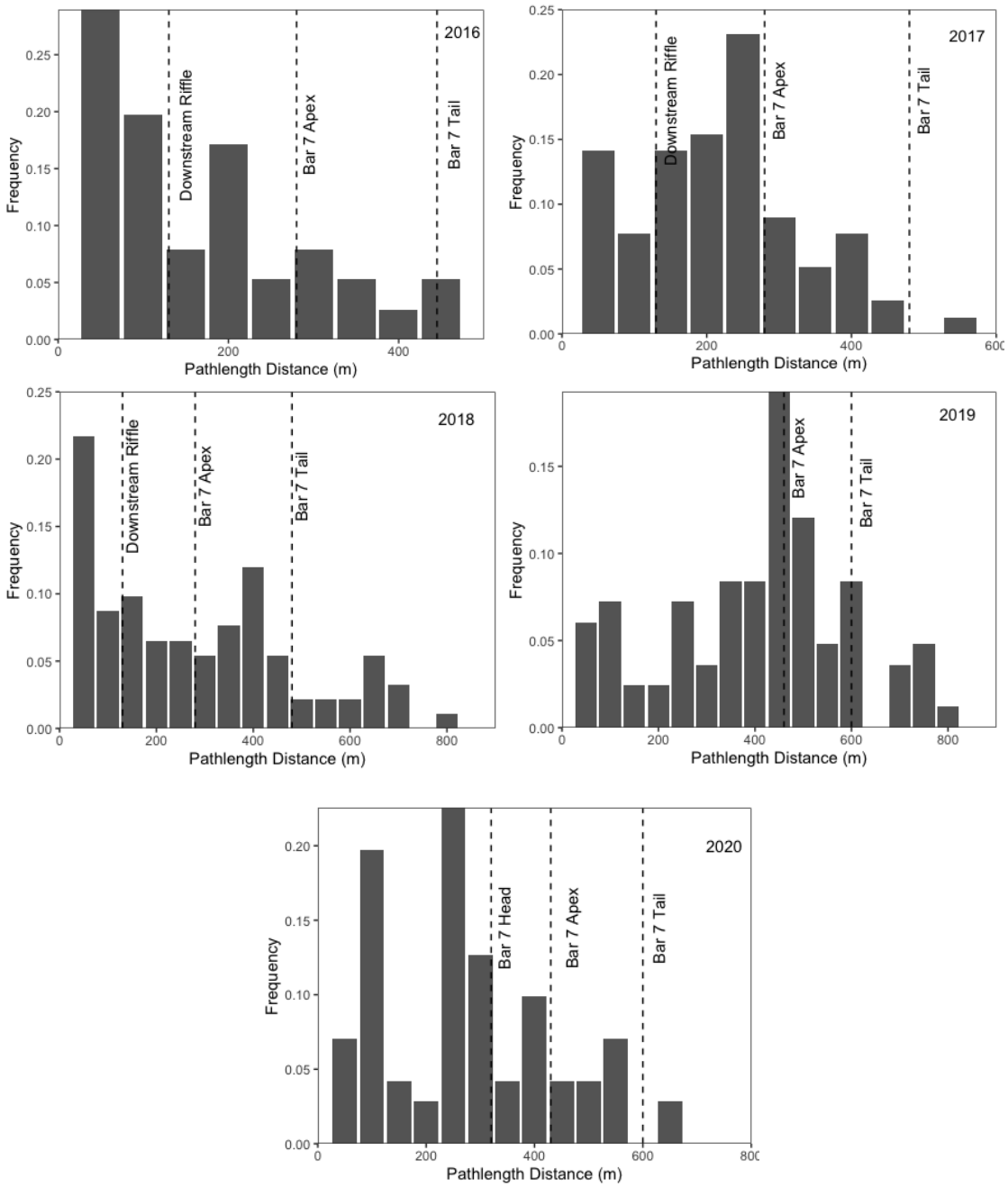

Figure 30. Pathlength distributions for recovered tracers at the Bar 7 study reach for the 2019-20 year (middle right) and 2020-21 year (bottom) and for a previous tracer deployment study (2016-2018).

The 2017 deployment at the Bar 7 study reach, that experienced the second largest peak flood event, had a similar uniform distribution to the 2019 tracer deployment, with high deposition of tracers at the Bar 7 apex (Figure 30). Furthermore, pathlength distributions for the 2016, 2018, and 2020 deployment years that had relatively moderate peak flood events, all displayed right-skewed

multimodal distributions. The greater peak flood events that occurred during the 2017 and 2019 deployments may explain the difference in pathlength distributions for these years, with higher flows leading to greater overall mobility and greater pathlength distances of tracers. In contrast, deployments that were subject to more moderate flood events had a high proportion of tracers that remained close (< 100m) to the initial seeding location (Figure 29; Figure 30).

For all deployment years at the Bar 7 study reach, there was consistent high deposition of tracers at the Bar 7 apex, even though hydrological activity and the magnitude of peak flood events differed between years (Figure 29; Figure 30) . This suggests that channel morphology, rather than flow, is the dominant control on pathlength distances. As well, high deposition at the bar apex, specifically the bar apex margins, can be linked to overall bar development, with observations of downstream migration and lateral growth of the gravel bar from annual aerial imagery (McQueen et al., 2021). Furthermore, the 2019-20 and 2020-21 deployments at the Bar 6 study reach (located ~200m upstream of the Bar 7 study reach deployment locations) also had a high proportion of tracers being deposited at the Bar 7 apex. This suggests that the Bar 7 apex is a significant trapping area and thus, an important morphological control on pathlengths, especially for years subject to greater peak flood events. Overall results from pathlength comparisons show a strong morphological constraint on pathlengths, with tracers becoming trapped at the first major downstream depositional area. As well, observations of annual channel change from aerial imagery can link individual tracer pathlengths to overall bar growth development, with compensating erosion to the opposite bank. The influence of flow strength is also apparent, with deployment years subject to lower magnitude flood events leading to a greater proportion of tracers moving short (<100m) distances downstream of the initial deployment location.

Bar 15

The 2019-20 and 2020-21 deployment locations were the same, with tracers seeded at the pool tailout adjacent to the Bar 15 head at the bar head (Figure 31). The previous two deployments (2017 and 2018) were located ~15m downstream, and the 2016 deployment was located ~30m downstream of the 2019-20 and 2020-21 deployment location.

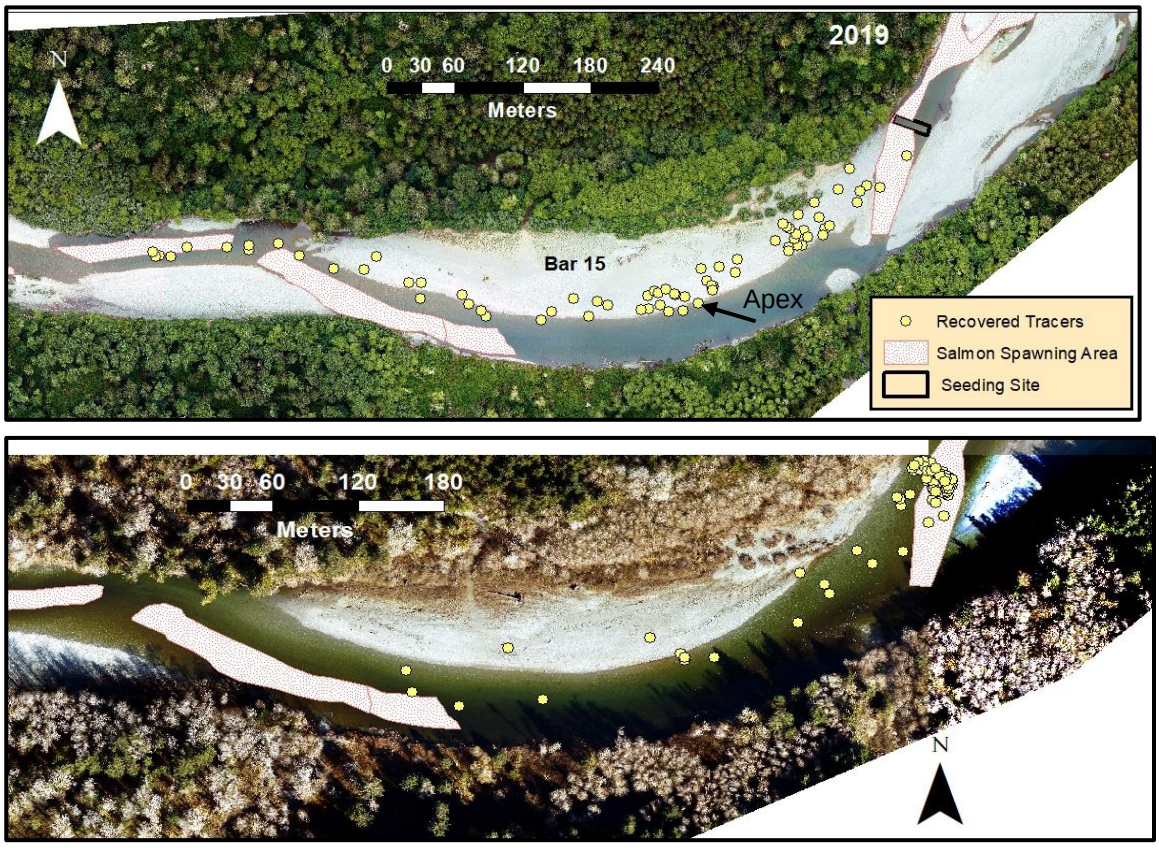

Figure 31. Recovered tracers deployed at the Bar 15 study reach for the 2019-20 year (top) and 2020-21 year (bottom). Flow right to left.

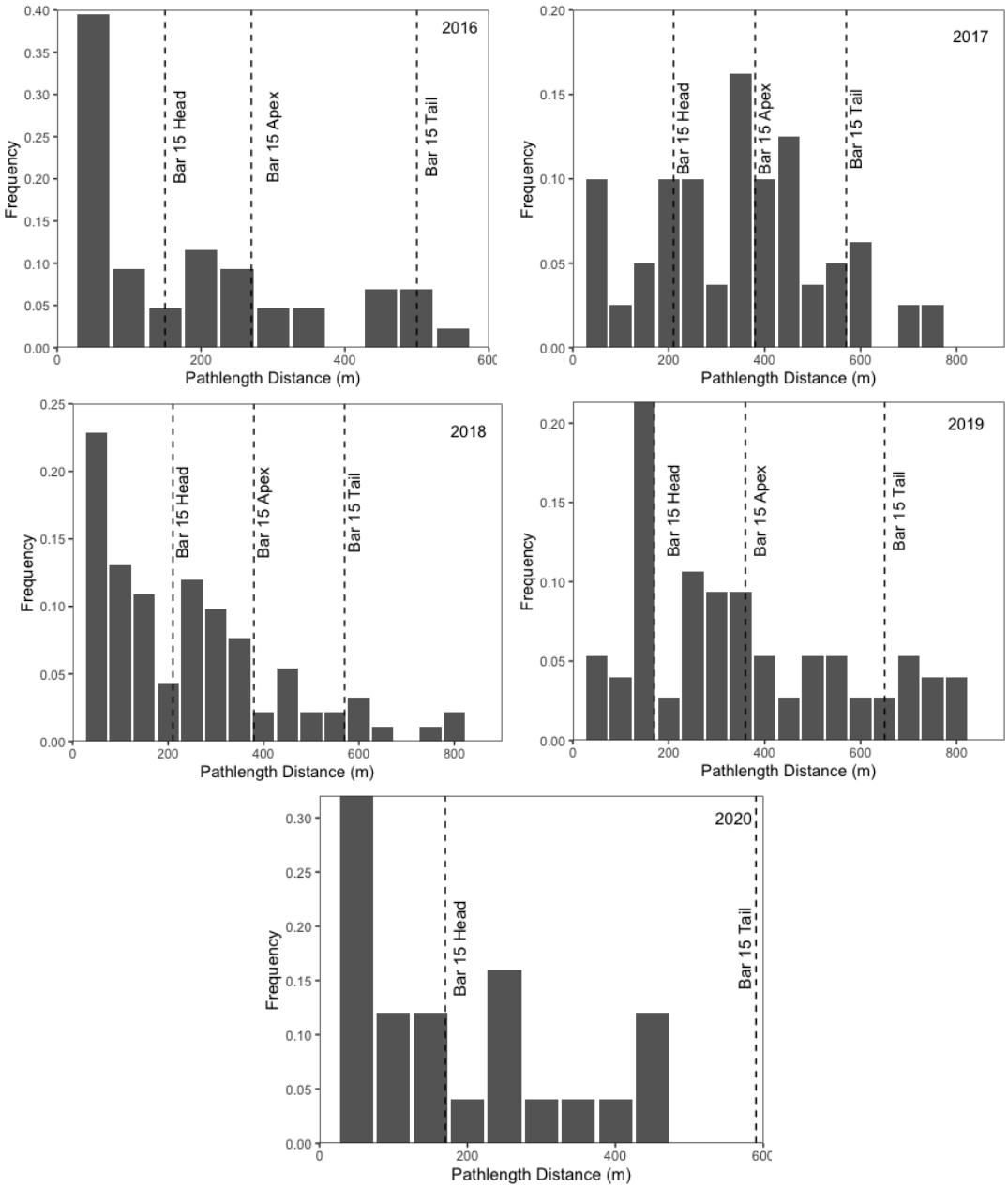

Figure 32. Pathlength distributions for recovered tracers at the Bar 15 study reach for the 2019-20 year (middle right) and 2020-21 year (bottom) and for a previous tracer deployment study (2016-2018).

Pathlength distributions for the 2019-20 and 2020-21 deployments display similar right-skewed multi-modal distributions (Figure 32). Although, differences are apparent in the longer-tailed pathlength distribution for the 2019-20 deployment, compared to the 2020-21 deployment at the

Bar 15 study reach that had a maximum pathlength distance of only 450m (Figure 32). The first mode of deposition of tracers at the Bar 15 study reach for the 2019-20 deployment occurs at the bar head , ~100m downstream of the seeding site (Figure 31; Figure 32). This was also the case for the 2020-21 deployment, with a greater number of tracers travelling short distances and depositing at the bar head, relative to the 2019-20 deployment (Figure 31). The second mode of deposition for the 2019-21 deployment is associated with a cluster of tracers that deposited at the bar apex near the channel margin (Figure 31; Figure 32). The second and third mode of deposition for the 2020-21 deployment also occurs at the bar apex, and just downstream of the bar apex, respectively. Differences in pathlength distribution of tracers between the 2019-20 and 2020-21 deployment are reflective of peak discharge and flow conditions experienced that year.

Bar 15 tracer pathlength distributions from previous deployment years are similar to both 2019-20 and 2020-21, exhibiting right-skewed, multi-modal distributions, with the exception of the 2017 deployment (Figure 32). The 2017 year exhibits a more uniform pathlength distribution, with the primary mode of deposition occurring at the bar apex (Figure 32). Although the 2020-21 deployment year had the highest peak flows, the 2017 year had the most flood events above bankfull. This suggests that the frequency and duration of flood events above may have influenced tracer pathlength distributions, with a greater number of tracers being remobilized for the 2017-18 deployment year. Like the other two study reaches, for all deployment years at the Bar 15 study reach, there appears to be a morphological constraint, with tracers rarely exceeding one riffle-pool-bar unit. Furthermore, differences in tracer pathlength distributions at the Bar 15 study reach between years may be associated to the number of flood events above bankfull and flood duration. This suggests that since the Bar 15 study reach has a more simple channel morphology relative to the other two study reaches, the influence of flow may be greater.

5.4.6.1 Exceedance Probability Distributions

Tracer pathlength distances for the three study reaches were ranked in a descending order ($X > x$) to examine exceedance probabilities. Such that, the probability of exceeding the minimum pathlength distance for a given year, at a given study reach is equal to 1. Exceedance probability distributions were analyzed for the 2019-20 and 2020-21 deployment years at the three study reaches, with previous pathlength data (2015-2018) also assessed for the Bar 7 and Bar 15 study reach (McQueen, 2019) (Figure 33).

Exceedance probabilities show differences between study reach distributions, as well as differences within a given study reach between years (Figure 33). The 2016-17 and 2020-21 deployment years were subject to the lowest peak flood events, with less tracers travelling extreme distances (relative to the average) at the Bar 15 study reach, seen in the lighter-tailed distributions for these years (Figure 33). This is also apparent at the Bar 6 study reach, with more extreme values, reflected in the heavy-tailed distribution for the 2019-20 deployment year, compared to the 2020-21 deployment year that saw a much more moderate flood event. Furthermore, the Bar 7 study reach displays the heaviest-tailed distributions of tracer pathlength distances compared to the other two study reaches for all years (Figure 33).

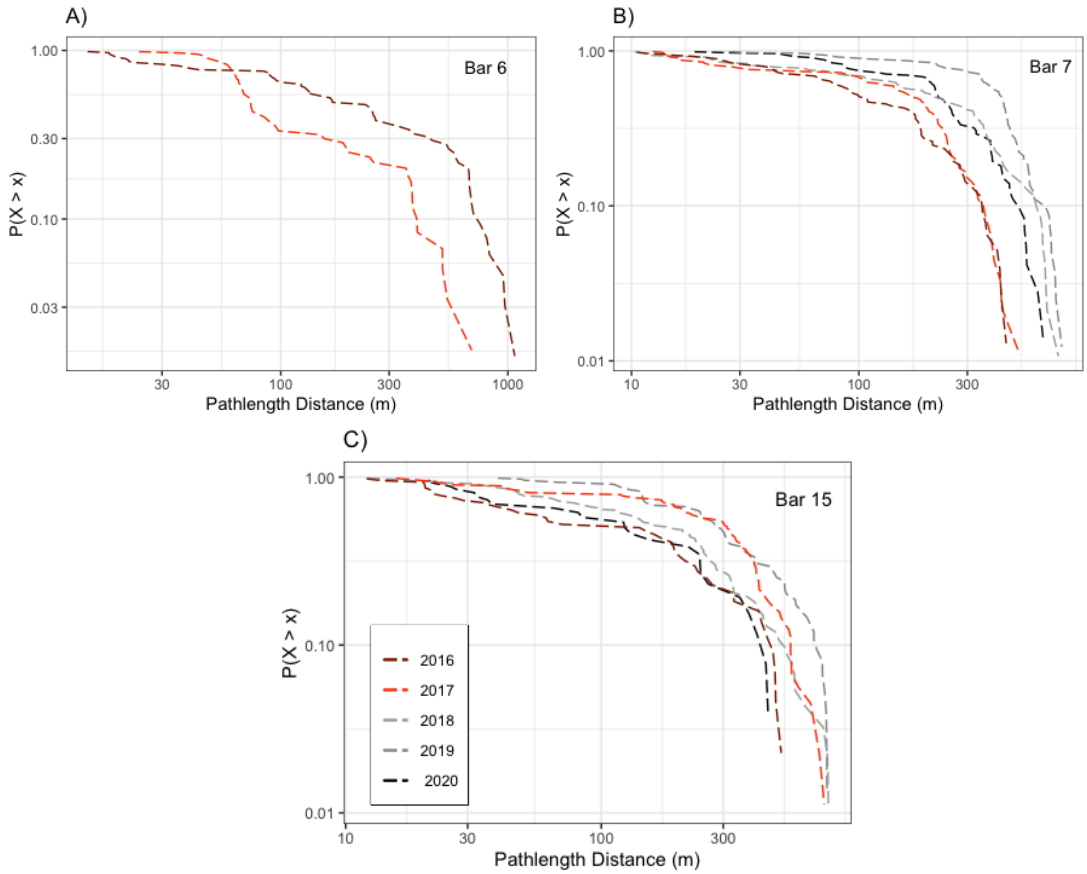

Figure 33. Exceedance probability plots of pathlength distances for A: Bar 6 study reach B: Bar 7 study reach and C: Bar 15 study reach.

5.4.7 Deposition By Morphology

The influence of channel morphology on tracer pathlength dispersion was further investigated by assessing tracer deposition by morphology unit for both the 2019-20 and 2020-21 deployment years (Figure 34). The channel was classified by macro-scale bedform (Bar Head, Bar Apex, Bar Tail) as well as pool, riffle, and pool tailout units. Tracer deposition by morphology unit was further classified to investigate any influence of grain size on deposition location. The unit of deposition for tracers was recorded during tracer recovery and further verified using 2019 and 2020 aerial imagery. The extent of each unit could not be precisely delineated (i.e pool transition into pool tailout), however using recorded field notes and aerial imagery, reliable deposition locations could be inferred.

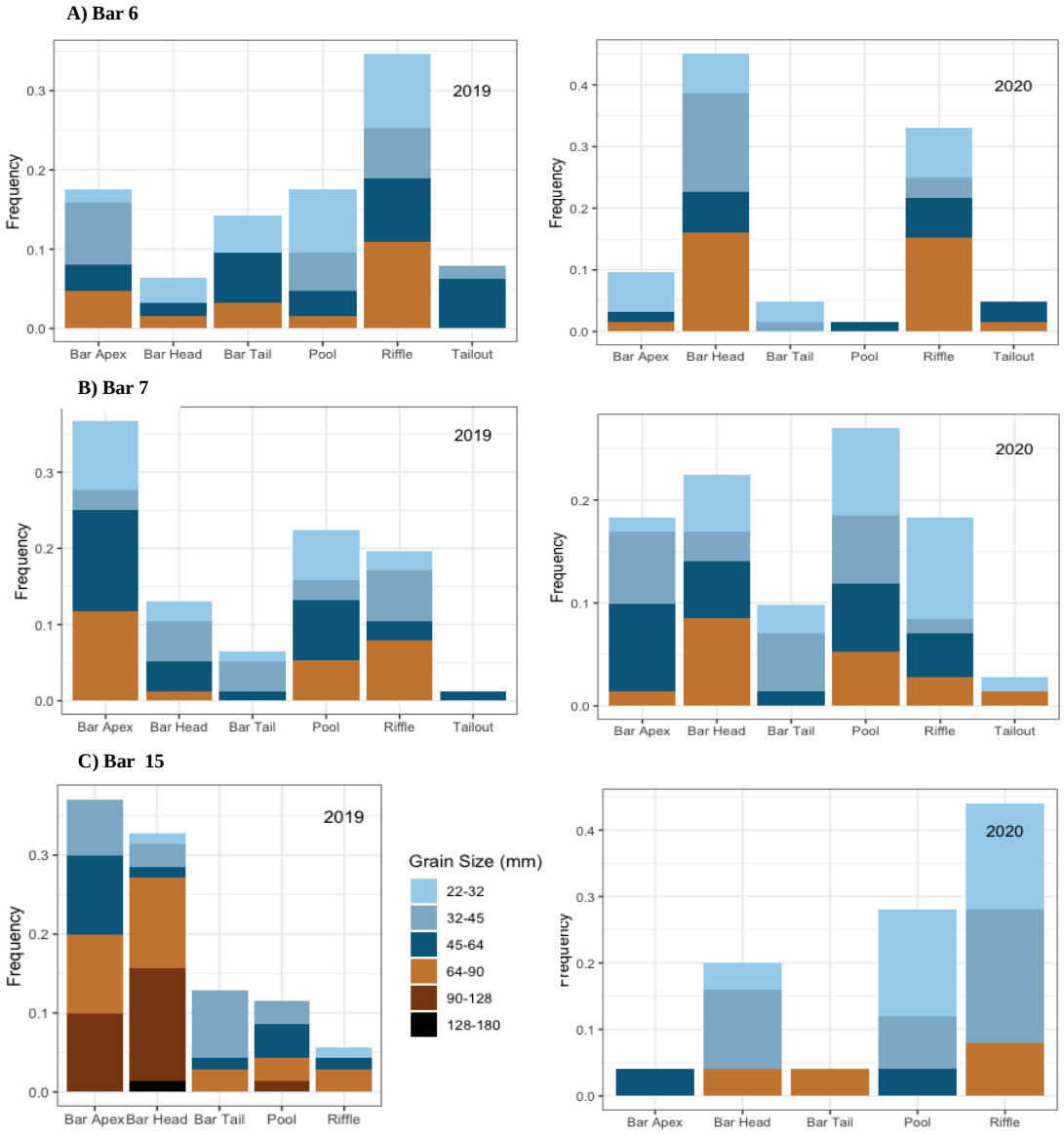

Figure 34. Surface tracer frequency across morphological units for A: Bar 6 study reach; B: Bar 7 study reach and C: Bar 15 study reach.

Different patterns of tracer deposition by morphology unit are seen between the three study reaches, with a greater proportion of tracers at the bar 15 study reach depositing at the bar head (Figure 34). Differences in flow trajectory where tracers are initially mobilized, influenced by the reach-scale morphology, may explain the variation in tracer deposition by morphology unit between the three study reaches. Differences in tracer deposition are also apparent between the two deployment years, within a given study reach. For the 2019-20 deployment year, which experienced the 100-year flood event, all three study reaches saw a greater proportion of tracers depositing at the bar apex, compared to the 2020-21 deployment year (Figure 34). For the Bar 6 and Bar 7 study reaches, there was an increase in the number of tracers depositing at the bar head, and a subsequent decrease in the number of tracers depositing at the bar apex, for the 2020-21 deployment year, which was also seen in previous tracer work in the San Juan River (McQueen, 2021) (Figure 34). These findings support the idea that in lower flow years, more particles deposit onto the bar head, with greater tracer deposition at the bar apex and thus, greater bar growth and development, in years subject to higher-magnitude peak flood events.

For the 2020-21 deployment year, a greater proportion of tracers were deposited in pools at the Bar 7 and Bar 15 study reach, compared to the 2019-20 deployment year that experienced higher peak magnitude flows (Figure 34). This agrees with the literature, that a greater proportion of particles are routed into pools during lower peak flood events (Milan et al., 2013). Contradicting this, the bar 6 study reach had a lower proportion of tracers deposited in pools for the 2020-21 deployment, (Figure 34). However, the Bar 6 study reach had the lowest recovery, with the smallest tracer class having the lowest number recovered for the 2020-21 year, which suggests that some of the ‘missing’ tracers may well be deposited in pools, at water depths beyond detection.

Although there is no obvious influence of grain size on tracer deposition by morphology unit, some patterns emerge. The larger grain size classes had a higher proportion deposited on the bar head and bar apex, especially at the Bar 15 study reach (Figure 34). The smaller two grain size classes of tracers had a greater number deposit on the bar tail, riffles, and pools (Figure 34). This also points to sediment routing patterns influenced by grain size, as well as grain-size sorting patterns on the gravel-bar, which have been noted in the literature (Clayton, 2010).

5.4.8 Tracer Burial Depths

To investigate the active layer depth in large gravel-bed rivers, tracer burial depth data for the 2019-20 and 2020-21 deployment years were analyzed (Table 8). Median burial depth (B_m) is used to represent the distribution of the data, as tracers that could not be detected with the wand antenna (> 0.5m) were not physically dug up, and accurate burial depth is unknown. Tracers that were undetectable were assumed to be buried at 0.5m, which was also used as a proxy for previous tracer work in the San Juan River (McQueen et al., 2021), therefore burial depths are a conservative estimate. Burial depth data for the 2020-21 deployment year is limited, due to lower mobility and a greater proportion of tracers being deposited in the wetted channel, in which burial depth could not be assessed.

Table 8. Tracer burial data for the 2019-20 and 2020-21 deployment years.

Year	Gravel Bar Site	N_{buried}	B_m
2019-20	Bar 6	21	50
	Bar 7	41	32
	Bar 15	52	21.8
2020-21	Bar 6	7	50
	Bar 7	13	17
	Bar 15	4	7

For both deployment years, the bar 6 study reach had the greatest burial depth, with B_m = 0.5m (Table 8). Both the Bar 6 and Bar 7 study reach had greater median burial depths than the Bar 15 study reach. This agrees with previous findings in the San Juan River, where lower burial depths at the Bar 15 reach reflected the lower magnitude of topographic change seen on DoDs (McQueen, 2021). The value of $2D_{90}$ (twice the 90th percentile of the coarsest grain size) is commonly used to assess the maximum extent of the active layer depth (Hassan, 1990). Importantly, median burial depths were greater than $2D_{90}$ for all three study reaches (Bar 6 D_{90} = 95mm; Bar 7 D_{90} = 103mm; Bar 15 D_{90} = 88mm) during the 2019-20 deployment year subject to the 100yr flood event. Burial depths were also analyzed by grain size class for the 2019 deployment year, however, no obvious trends were observed (Figure 35).

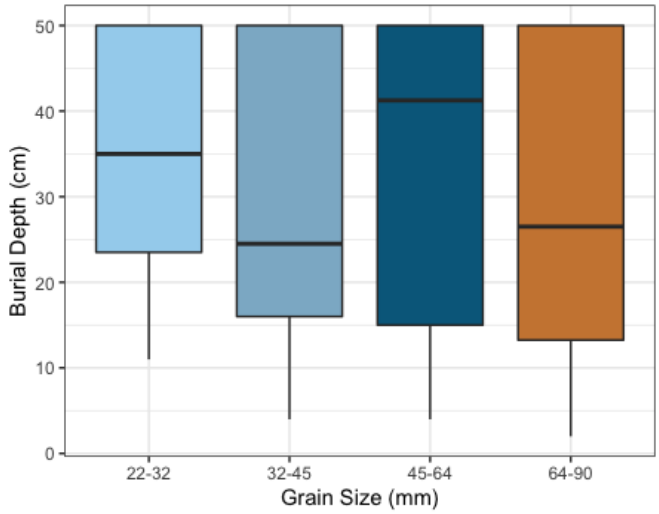

Figure 35. Burial depths (cm) by grain size class (mm) for the 2019 deployment year.

5.5 Buried Tracer Results

5.5.1 Overview of Results

Table 9 provides a summary of buried tracer results for the two deployment years. Recovery of buried tracers was high, ranging from 69.4-100% recovery (Table 9). The Bar 6 study reach for the 2019-20 deployment, and the Bar 15 study reach for the 2020-21 deployment experienced limited scour, and therefore had high recovery of tracers for that year (Table 9). The Bar 7 study reach had high mobility and scour for both deployment years, relative to the other two study reaches (Table 9). Pathlength distances of recovered mobilized tracers for the Bar 6 and Bar 7 study reaches were greater for the 2019-20 deployment year, relative to the 2020-21 year (Table 8). However, only two tracers were mobilized at the Bar 6 study reach for the 2019-20 year, with (N = 2), making pathlength comparisons difficult to interpret between the two years at the Bar 6 study reach (Table 9).

Tracer mobility and pathlength distances of buried tracers are assessed in section 5.5.2. Pathlength distributions, as well as exceedance probability distributions, which compare buried and surface tracer pathlengths, are found in section 5.5.3 and 5.5.3.1 respectively. Results of buried tracer deposition by morphology unit are found in section 5.5.4. Section 5.5.5. discusses

the comparison results between surface and buried tracer pathlength distributions. Scour results can be found in section 5.5.6, and burial depth results can be found in section 5.5.7. Lastly, a summary of surface and buried tracer results can be found in section 5.6.

Table 9. Summary of buried tracer results for the 2019-20 and 2020-21 deployment year

Year	Q_p (m^3 s^{-1})	Recovery (%)	F_m	S (%)	$\bar{L}$ (m)	L_m (m)
			Bar 6			
2019-20	1360	97.3	0.06	5.7	266.5	NA
2020-21	735	83.3	0.54	82.7	125.7	72.6
			Bar 7			
2019-20	1360	69.4	0.97	100	425.8	438.9
2020-21	735	83.3	1	100	251.8	262.4
			Bar 15			
2019-20	1360	75	0.77	96.7	115.7	122.2
2020-21	735	100	0	0	NA	NA

5.5.2 Particle Mobility and Pathlength Distance

Buried tracer mobility (F_m) varied between study reaches as well as deployment years (Table 9; Table 10). For the 2019-20 deployment year, the Bar 6 study reach had low overall mobility of buried tracers (F_m = .06) with only two tracers, initially buried at 10cm depths, being mobilized (Table 10). Overall mobility of buried tracers for the 2019-20 deployment year was higher for the other two study reaches: Bar 7 (F_m = .97) and Bar 15 (F_m = .77). For the 2019-20 year, the Bar 7 study reach had full mobility for tracers initially buried at 10cm and 30cm depths, with slightly lower mobility (F_m = .89) for tracers initially buried at 20cm depth (Table 10). The Bar 15 study reach also had near full mobility for the 2019-20 deployment year, with tracers initially buried at 10cm depths having slightly lower mobility (F_m = .70) compared to 20cm depths (F_m = .91) and 30cm depths (F_m = .80) (Table 10).

For the 2020-21 deployment year, that saw a more moderate peak flood event, compared to the 2019-20 year (Table 10), the Bar 6 study reach saw greater mobility (F_m = 0.54). For the 2020-21 year, tracers at the Bar 6 study reach that were initially buried at 30cm depths had significantly lower mobility (F_m = 0.27) relative to 10cm (F_m = 0.63) and 20cm depths (F_m = 0.73) (Table 10).

For the 2020-21 year, the Bar 7 study reach had the highest mobility of buried tracers, relative to the other two study reaches, with full mobility (F_m = 1) at 10cm seeding depths and near full mobility at both 20cm (F_m = 0.80) and 30cm depths (F_m = 0.88). None of the buried tracers at the bar 15 study reach were mobilized for the 2020-21 year, with surface tracers at the Bar 15 study reach for the 2020-21 year also subject to much lower mobility, relative to the previous deployment year.

Table 10. Mobility (F_m) of recovered buried tracers by initial burial depth (cm).

Year	Initial Burial Depth (cm)	Bar 6 F_m	Bar 7 F_m	Bar 15 F_m
2019-20	10	0.17	1	0.70
	20	0	0.88	0.91
	30	0	1	0.80
2020-21	10	0.75	1	0
	20	0.73	0.80	0
	30	0.27	0.88	0

Surprisingly, mobility of buried tracers at the Bar 6 study reach was low for the 2019-20 deployment subject to the extreme flood event, relative to the 2020-21 deployment year that had a more moderate flood event (Table 10). Previous tracer work at the Bar 6 study reach identified a coarse gravel sheet that migrated downstream from the Bar 6 head between 2015 and 2019 (McQueen et al., 2021). This may explain the limited mobility of buried tracers that were seeded near the apex margin at the Bar 6 study reach for the 2019-20 year, with only two tracers being able to become mobilized and 'escape' prior to deposition by the coarse gravel sheet at the seeding area. The Bar 7 study reach had similar mobility between the two deployment years, even with the Bar 7 seeding site being moved ~20m upstream for the 2020-21 deployment. The Bar 15 study reach, which had high mobility during the 2019-20 deployment, did not have any tracers mobilized during the 2020-21 deployment year (Table 9). This may be explained by channel changes that occurred during the 100yr flood event the prior deployment year, specifically, channel avulsion, which led to primary flows being redirected, away from the seeding area. Differences in mobility between study reaches and deployment years may be related to differences in flow strength, as well

as the influence of the local bed texture at the seeding area, with high spatial variation of tracer mobility seen within study reaches.

Both average ($\bar{L}$) and median (L_m) pathlength distances of buried tracers were calculated, to account for expected skewed distributions (Table 9; Table 11). For the 2019-20 deployment year, recovered buried tracers that were mobilized had $\bar{L}$ of 266.5m, 425.8m, and 115.7m for the Bar 6, 7, and 15 study reach respectively (Table 9). L_m could not be calculated for the Bar 6 study reach for the 2019-20 year (N = 2), however both the Bar 7 and Bar 15 study reach had $L_m > \bar{L}$, suggesting skewed pathlength distributions. Average pathlength distances ($\overline{L}$) of recovered buried tracers for the 2020-21 deployment year were significantly lower for the Bar 6 and Bar 7 study reach, relative to the 2019-20 deployment year (Table 9).

Amongst grain size classes, pathlength distances tend to follow a decreasing trend with increasing grain size class for both deployment years for all study reaches, with few exceptions (Table 11). The smallest grain size class (22-32mm) had the greatest pathlength distances for all study reaches and both deployment years, with the exception of Bar 7 for the 2020-21 deployment year, with the largest grain size class (64-90mm) having the highest average pathlength distances (Table 11). However, the smallest grain size class of buried tracers at the Bar 7 study reach for the 2020-21 deployment year had a slightly greater median pathlength distance than the largest class. Two 64-90mm tracers, initially buried at 10cm depths travelled > 500m at the Bar 15 study reach for the 2020-21 deployment year, skewing the data for the largest grain size class (Table 11).

In summary, the 2019-20 deployment year subject to a 100-yr flood event led to greater pathlength distances of buried tracers, compared to the 2020-21 deployment year subject to a more moderate flood event. Similar to surface tracer results, pathlength distances of buried tracers varied between study reaches and deployment years, with Bar 7 tracers having the greatest average pathlength distances for both deployment years (Table 11). Similar to surface tracer results, pathlength distances tended to decrease with an increase in grain size class, however, two 64-90mm tracers travelled extreme distances at the bar 15 study reach for the 2020-21 deployment year, skewing the data.

Table 11. Pathlength distances (m) of recovered buried tracers by grain size class (mm).
N_A represents the number of buried tracers recovered that are used in the analysis.

Year	Grain Size (mm)	Bar 6			Bar 7			Bar 15		
		N_A	$\bar{L}$ (m)	L_m (m)	N_A	$\bar{L}$ (m)	L_m (m)	N_A	$\bar{L}$ (m)	L_m (m)
2019-20	22-32	0	-	-	5	562.5	558.9	7	139.6	139.3
	32-45	1	446.2*	446.2*	5	347.2	445.3	6	144.4	154.9
	45-64	1	86.8*	86.8*	7	388.7	430.6	6	96.7	89.6
	64-90	0	-	-	7	421.3	419.5	6	78.0	45.5
2020-21	32-45	10	219.5	181.5	11	267.9	271.3	0	-	-
	45-64	3	200.7	114.7	7	199.8	111.7	0	-	-
	64-90	3	80.6	87.3	6	320.9	269.1	0	-	-

5.5.3 Pathlength Distributions

To further assess pathlength distances of buried tracers, the pathlength distributions (pathlength distance frequencies) of recovered, mobilized (moved > 10m downstream) buried tracers were also analyzed. Pathlength distributions were binned into 50m intervals to visualize tracer frequency distributions within and between macro-scale bedforms (length of the gravel bar) to interpret final tracer positions relative to meso-scale morphological units (pools, riffles, bar apex) in the reach. Buried tracer pathlength distributions at the bar 15 study reach from the 2019-20 deployment year, as well as buried tracers at the bar 15 study reach from the 2020-21 deployment year, are not included in this analysis as the tracers had limited or no mobility.

Aerial imagery acquired from LIDAR data collected by Terra Remote Sensing Inc in 2019, is used to display buried tracer recovery locations for the 2019-20 deployment year. As well, aerial imagery acquired from LIDAR data, collected by Terra Remote Sensing Inc in 2021 is used to display tracer recovery locations for the 2020-21 deployment year. Importantly, the July 2019 aerial imagery shows recovered buried tracer locations relative to the channel morphology at the time of deployment (Fall 2019) and does not capture channel changes that occurred during the 2019-20 winter flooding period. Furthermore, the March 2021 aerial imagery was collected earlier than usual, at higher flows, thus the gravel bars are more inundated relative to the actual recovered position in July 2021 at low flow.

Bar 6

The Bar 6 study reach deployment location for the 2019-20 and 2020-21 deployment of buried tracers was located near the tail of Bar 6 at the channel margin adjacent to the pool-tailout where surface tracers were deployed (Figure 37). The deployment location for the 2020-21 deployment was relocated ~10m downstream because of changes to the channel morphology at the original deployment location (Figure 37). Only two tracers for the 2019-20 deployment at the Bar 6 seeding site were mobilized, moving ~85m and ~450m downstream (Figure 37). The 2020-21 deployment year at the bar 6 study reach, subject to a more moderate peak flood event relative to the 100-year flood event in 2019-20, had a greater number of buried tracers become mobilized (N = 26).

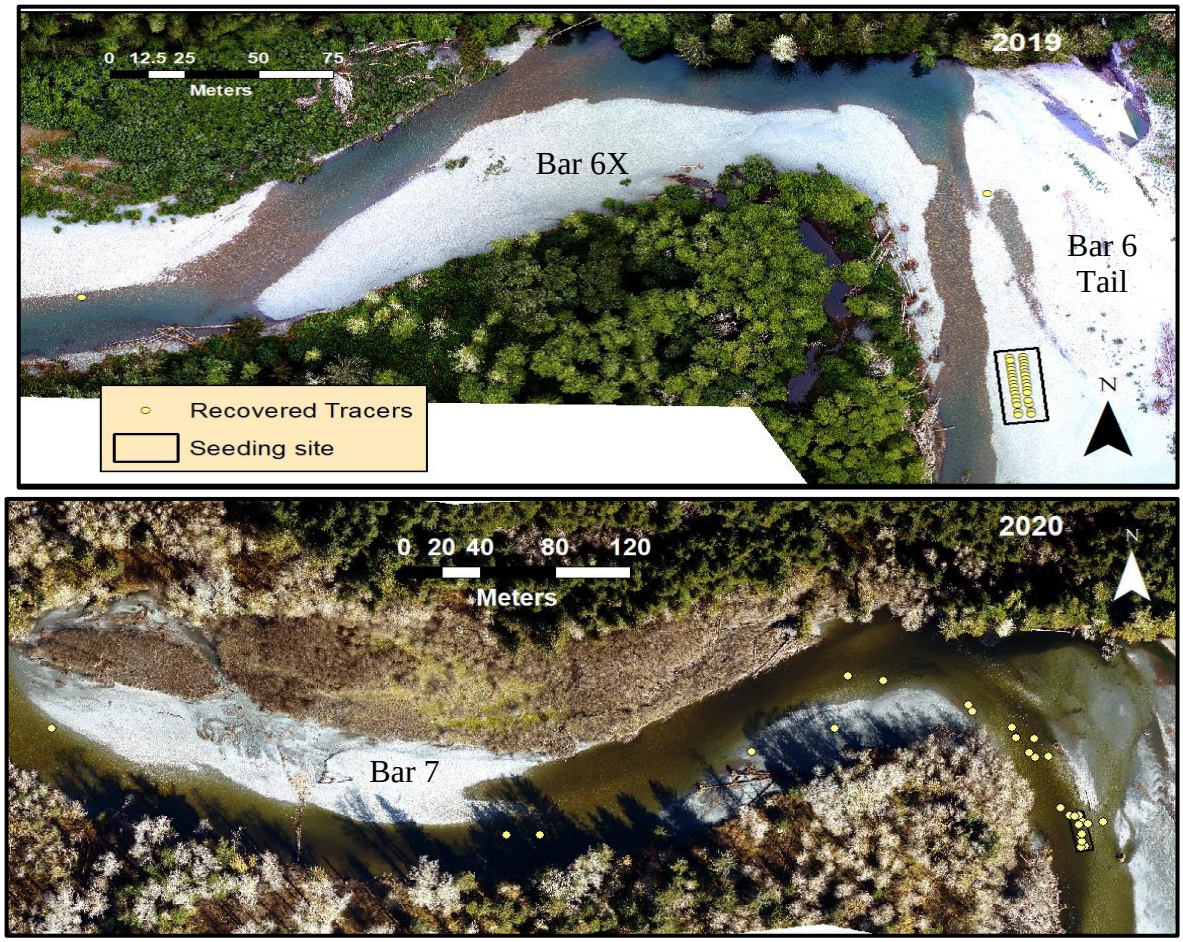

Figure 36. Recovered buried tracers deployed at the Bar 6 study reach for the 2019-20 year (top) and 2020-21 year (bottom). Flow right to left.

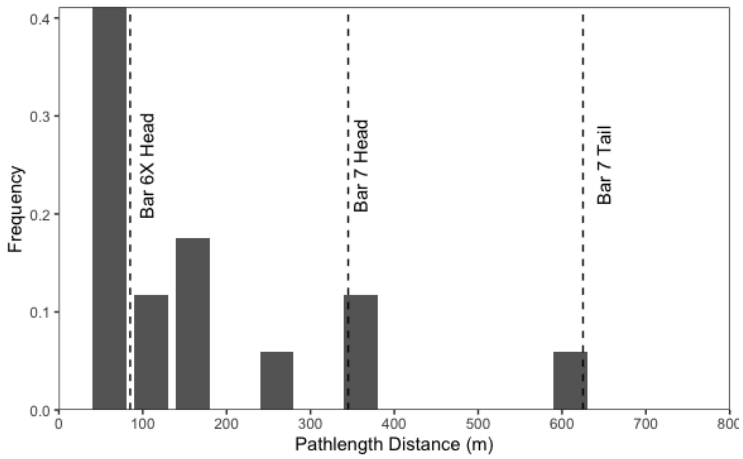

Figure 37. Pathlength distributions for recovered buried tracers at the Bar 6 study reach for 2020-21 study year .

The 2020-21 buried tracers at Bar 6 display a right-skewed distribution with the majority (~ 40%) tracers moving a relatively short distance, depositing in a cluster at the head of Bar 6X, representing the primary mode of buried tracer deposition (Figure 38). A few tracers travelled farther, with two tracers being deposited near the Bar 7 head, and one tracer being deposited at the Bar 7 tail (Figure 38). No tracers in either year travelled farther than one riffle-pool-bar unit, which is similar to surface tracer results for the two deployment years as well as previous tracer results in the San Juan River at the Bar 6 study reach (McQueen, 2019; McQueen et al., 2021). Furthermore, the primary mode of deposition at the Bar 6X head for the 2020-21 deployment year, where a large proportion of tracers were deposited, shows that mobilized tracers were subsequently trapped at the first depositional area downstream of the seeding site (Figure 38).

Bar 7

The deployment location at the Bar 7 study reach for both the 2019-20 and 2020-21 deployment of buried tracers was located near the Bar 6X apex, just upstream of the Bar 7 head, at the channel margins adjacent to the surface tracer pool-tailout deployment location (Figure 39). The seeding site for the 2020-21 deployment was relocated ~20m upstream because of changes to the channel (Figure 39). Both deployment years had high mobilization of recovered buried tracers at the Bar 7

study reach, with tracers travelling greater distances in the 2019-20 deployment year, subject to the 100 year flood event.

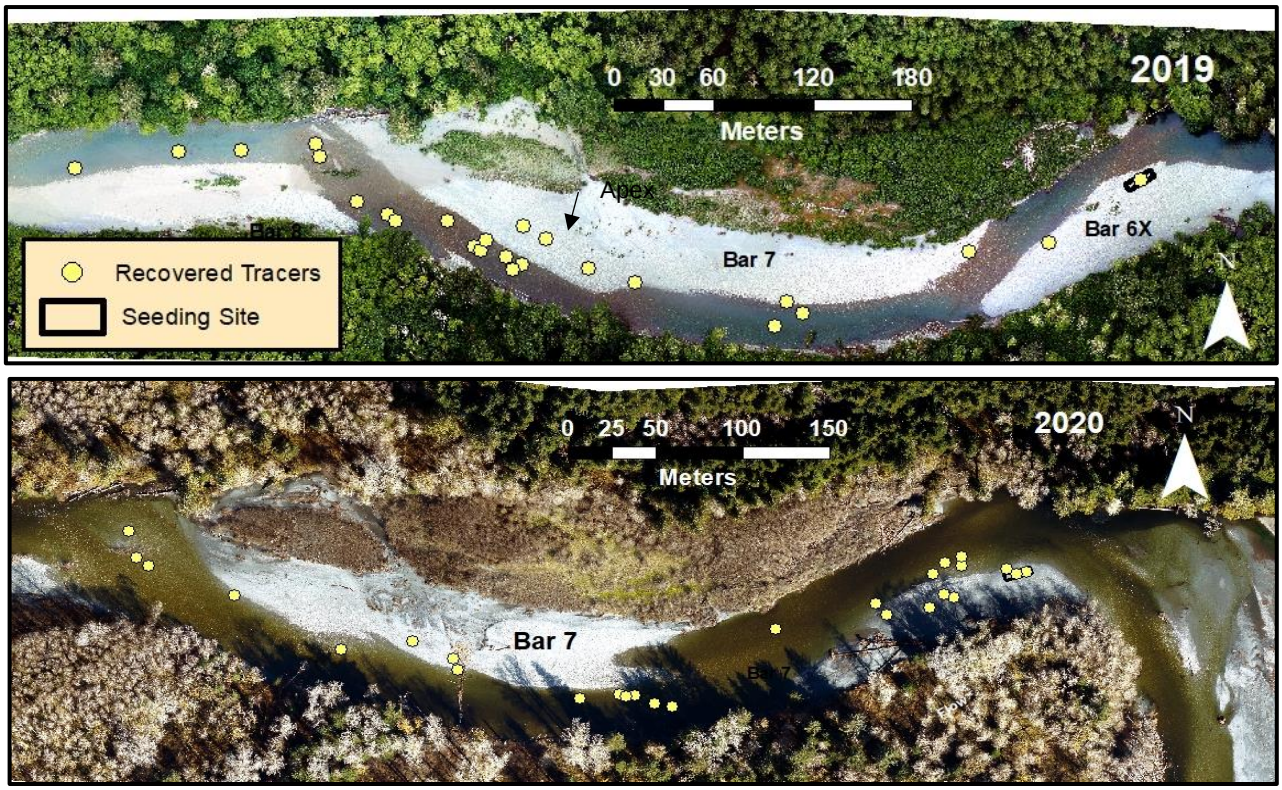

Figure 39. Recovered buried tracers deployed at the Bar 7 study reach for the 2019-20 year (top) and 2020-21 year (bottom). Flow is from right to left.

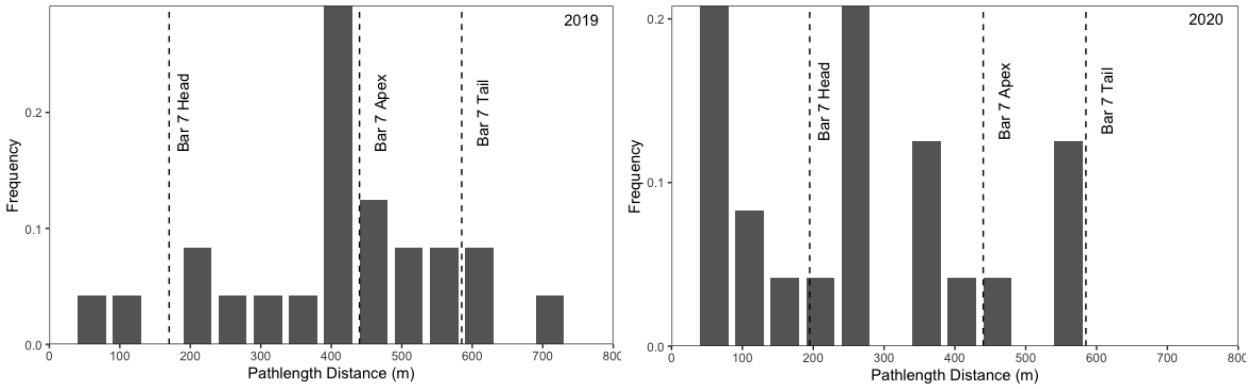

Figure 38. Pathlength distributions for recovered) buried tracers at the Bar 7 study reach for the 2019-20 (left) 2020-21 study year (right).

Pathlengths of recovered buried tracers at the Bar 7 study reach for the 2019-20 deployment year followed an approximately uniform distribution, with the highest proportion of tracers (~30%) being deposited at the Bar 7 apex (Figure 39; Figure 40). Only 10% of buried tracers exceeded one riffle-pool bar unit for the 2019-20 deployment year, which is similar to surface tracer results at the Bar 7 study reach for the 2019-20 year. For the 2020-21 deployment year, pathlengths of recovered buried tracers at the bar 7 study reach followed a multi-modal right-skewed distribution (Figure 40). A cluster of 2020-21 deployed tracers (~20%) travelled a short distance downstream and deposited at the Bar 6X apex, with a second cluster of tracers (~20%) being deposited at the Bar 7 head (Figure 39; Figure 40). A third cluster of tracers, representing the last depositional mode, were deposited at a newly formed channel island adjacent to the Bar 7 tail, although the imagery shows inundation in that area due to higher flows at the time of imagery collection (Figure 39; Figure 40). For the 2020-21 year, no tracers exceeded one riffle-pool-bar unit.

There are apparent differences between buried tracer pathlength distributions for the two deployment years at the Bar 7 study reach. The shorter pathlength distances of buried tracers for the 2020-21 deployment year can be attributed to the lower peak flood event that occurred, relative to the 2020-21 deployment year. Furthermore, the 2019-20 year that was subject to the extreme flood event, had a greater proportion of tracers (10%) exceed one riffle-pool bar unit. Additionally, a higher fraction of tracers were deposited at the Bar 7 apex for the 2019-20 year. This suggests that greater peak flows for the 2019-20 year led to greater pathlength distances, and contributed to bar growth and development at the Bar 7 study reach.

Bar 15

The bar 15 deployment location was located on the bar head, at the channel margin, adjacent to the pool tailout where surface tracers were deployed (Figure 41). The 2019-20 deployment year saw high mobility of recovered buried tracers (Figure 41). The 2020-21 deployment year, which experienced a more moderate peak flood event, had no mobilization of recovered buried tracers. This is similar to the results of Bar 15 surface tracers as the 2020-21 deployment year had much lower mobility than that of the 2019-20 recovered surface tracers, and may be influenced by recent channel avulsion leading to changes in flow direction at the deployment location between the two years.

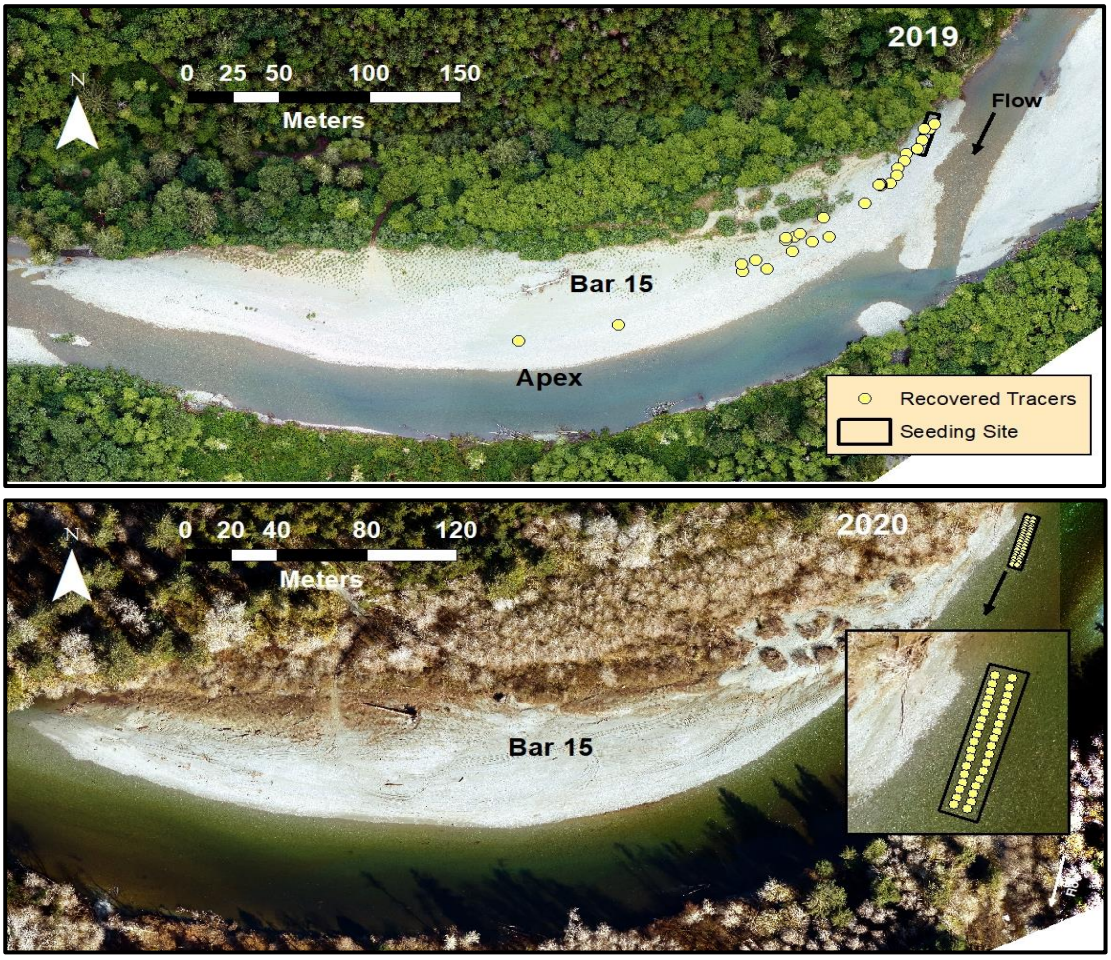

Figure 40. Recovered buried tracers deployed at the Bar 15 study reach for the 2019-20 year (top) and 2020-21 year (bottom). Flow right to left.

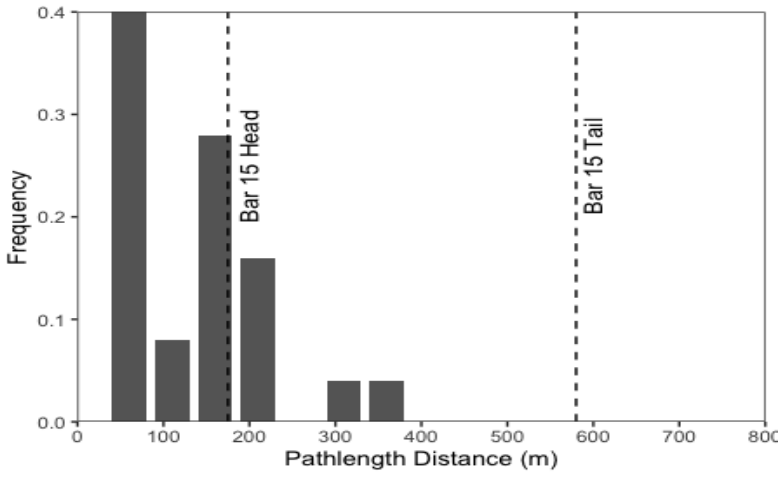

Figure 41. Pathlength distributions for recovered buried tracers at the Bar 15 study reach for the 2019-20 study year.

Pathlength distributions of recovered mobilized buried tracers at the Bar 15 study reach for the 2019-20 deployment year follow a right skewed distribution, with the vast majority of tracers (~90%) being deposited a short distance downstream at the bar 15 head (Figure 41; Figure 42). The remaining tracers (~10%) deposited at the Bar 15 apex, with no tracers exceeding one riffle-pool-bar unit (Figure 41; Figure 42). Overall, the Bar 15 study reach had shorter pathlength distances for both buried and surface tracers for the 2019-20 deployment year, compared to the bar 7 study reach, and may be related to the more simple channel morphology at the Bar 15 study reach.

5.5.3.1 Exceedance Probability Distributions

Exceedance probability plots were also used to visualize mobilized buried tracer pathlength distributions, as well as directly compare surface and buried tracer pathlength distributions at the same study reach and deployment year. The Bar 7 study reach had significant mobilization of buried tracers for both deployment years, although only the 2020-21 deployment year at the Bar 6 study reach and the 2019-21 deployment year at the Bar 15 study reach had sufficient tracer mobilization and are included in this analysis (Figure 43). Exceedance probability distributions help visualize the apparent pathlength differences between study reaches and deployment years (Figure 43). Furthermore, surface and buried pathlength distributions at the same study reach for the same deployment year, appear to be similar (Figure 43).

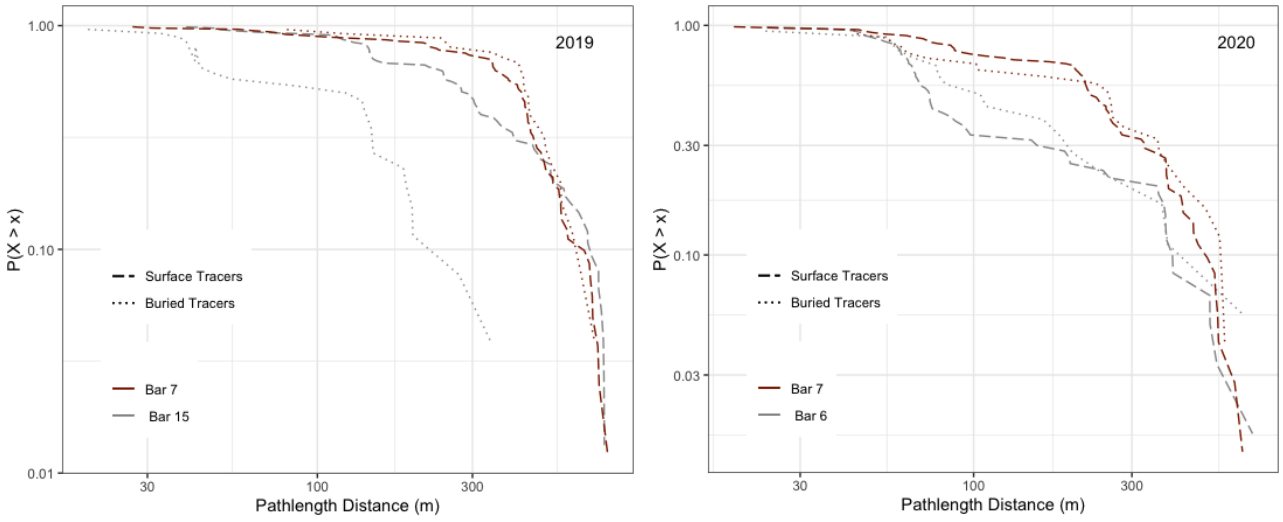

Figure 42. Comparison of exceedance probability distributions of surface and buried tracer pathlengths for the study reaches for the 2019-20 study year (left) and 2020-21 study year (right).

For the 2019-20 deployment year, Bar 15 buried tracers had much shorter pathlength distances with a maximum pathlength distance (L_{max}) = 342m, and exhibits a thinner-tailed distribution relative to bar 7 buried tracers, which saw an L_{max} = 709.1m. Furthermore, 75% of Bar 7 buried tracers exceeded the buried tracers L_{max} = 342m at the Bar 15 study reach, for the 2019-20 year. This results highlights, the differences in pathlength distributions between the two study reaches, which can be attributed to differences in morphology at the reach and local scale (Figure 43). Interestingly, for the 2019-20 year, Bar 7 recovered surface and buried tracers exhibit an extremely similar exceedance pathlength distribution, with buried tracers having a L_{max} of 709.1m, and surface tracers having a L_{max} of 780.6m (Figure 43). In contrast, buried and surface tracers display different pathlength distributions at the bar 15 study reach (Figure 43). However the overall shape of the distribution is similar, with the main difference being that buried tracers had a much shorter L_{max} = 342m, relative to L_{max} = 763.4m for surface tracers (Figure 43).

For the 2020-21 deployment year, buried tracers at the Bar 6 study reach travelled shorter distances on average than buried tracers at the Bar 7 study reach, however Bar 6 buried tracers had a greater L_{max} = 644.5m, with Bar 7 buried tracers L_{max} = 572m (Figure 43). Similar to pathlength results for the 2019-20 year, both buried and surface tracers at the Bar 7 study reach for the 2020-21 year exhibit similar pathlength distributions with L_{max} = 255m for buried tracers and L_{max} = 223m for surface tracers (Figure 43). Bar 6 buried and surface tracers exhibit similarly-shaped pathlength distributions, although a much heavier-tailed distribution is seen for surface tracers at the Bar 6 study reach (Figure 43).

Overall, Bar 7 surface and buried tracers exhibit similar exceedance pathlength distributions for both deployment years, with tracers travelling greater distances for the 2019-20 deployment year, seen in the heavier-tailed distribution, influenced by the 100-year flood event in January 2020 (Figure 43). Bar 6 buried and surface tracers for the 2020-21 year also displayed similar exceedance distributions, with the Bar 6 and Bar 7 seeding sites being in relative proximity. This suggests that in these two reaches, pathlengths of subsurface and surface tracers are in part controlled by depositional trapping areas, dictated by the reach-scale morphology. Furthermore, the different exceedance distributions seen for surface and buried tracers at the Bar 15 study reach, suggests that

the reduced complexity in channel morphology at this reach allows for other controls, such as flow, to have a greater influence on pathlength dispersion.

5.5.4 Deposition by Morphology Unit

The influence of channel morphology on buried tracer pathlength dispersion was further investigated by assessing the location of tracer deposition by morphology unit for both the 2019-20 and 2020-21 deployment years. However, neither Bar 6 2019-20 nor Bar 15 2020-21 buried tracers are analyzed because of the limited mobilization of these buried tracers. The channel was classified by macro-scale bedform (bar head, bar apex, bar tail) as well as by channel island (tail island), pool, riffle, and pool tailout units. Tracer deposition by morphology unit was further classified to investigate any influence of grain size on deposition location. The unit of deposition for tracers was recorded during tracer recovery and further verified using 2019 and 2020 aerial imagery. The extent of each unit could not be precisely delineated (i.e pool transition into pool tailout), however using recorded field notes and imagery, reliable depositional locations could be inferred.

All three study reaches displayed different depositional patterns of tracers by morphology unit (Figure 44). Similar to surface tracer results, deposition of Bar 15 buried tracers exhibit a less complex pattern, with deposition either at the bar head or bar apex, and is reflective of the more simple channel morphology at the Bar 15 reach, relative to the Bar 6 and Bar 7 study reach (Figure 44). Depositional patterns reflect the influence of the most proximate macroform unit, relative to the deployment location of buried tracers. With the majority of buried tracers at the Bar 15 study reach being deposited short distances downstream of the bar head seeding area, with only two tracers travelling slightly farther downstream and depositing at the bar apex (Figure 44).

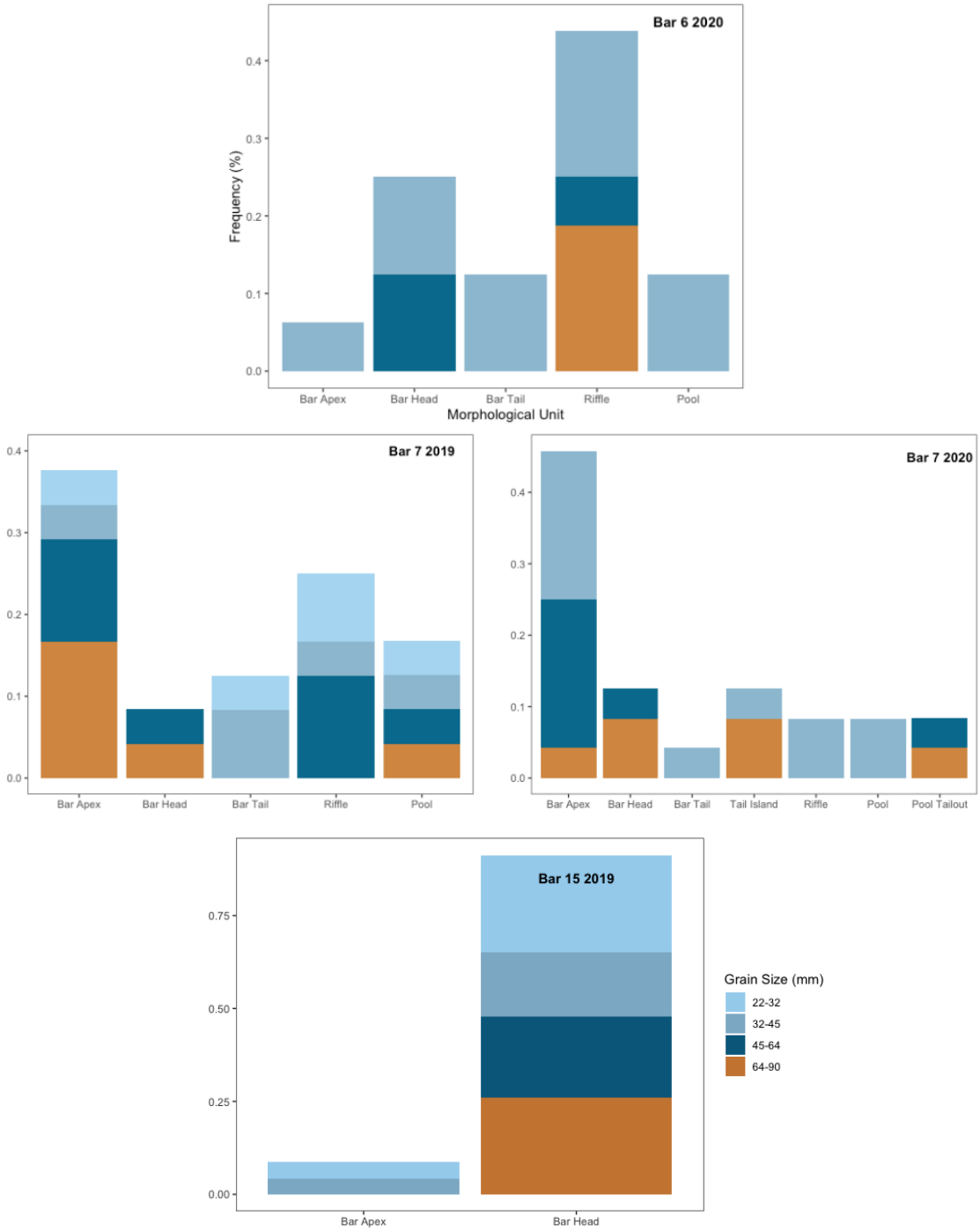

Figure 43. Buried tracer frequency distributions across morphological units by grain size (mm).

The majority of Bar 6 buried tracers that were mobilized during the 2020-21 deployment year were subsequently deposited in the riffle, which is the nearest downstream depositional unit, with most

of the remaining mobilized buried tracers also travelling short distances and were deposited at the bar 6X head, adjacent to this riffle (Figure 44). The high proportion of buried tracers being deposited at the bar 6X head is similar to surface tracer results at the Bar 6 study reach for the 2020-21 deployment year. Additionally, all of the recovered buried tracers at the Bar 6 study reach of the largest grain size-class deposited just a short distance downstream in the riffle, highlighting the influence of grain size on buried tracer deposition (Figure 44).

Bar 7 buried tracers had relatively similar depositional patterns for both deployment years, with high deposition at the bar apex (Figure 44). Although this is misleading, as the majority of buried tracers for the 2020-21 deployment deposited at the Bar 6X apex, roughly ~20m downstream of the deployment location, whereas for the 2019-20 deployment year, the majority of bar 7 buried tracers deposited ~400m downstream at the Bar 7 apex. The consistent deposition of both bar 7 recovered surface and buried tracers at the Bar apex strongly suggests the apex is a high trapping area, which can tied to lateral bar growth and development at the reach scale. When observing grain size trends, only the two smallest grain size classes of buried tracers at the Bar 7 study reach were deposited at the bar tail for both deployment years, which points to downstream fining, and overall grain-size sorting patterns of the bars.

Overall, between study reaches and deployment years, recovered buried tracers exhibit different depositional patterns by morphology unit, although there are some consistencies (Figure 44). Buried tracer results show high deposition at the bar apex for both deployment years at the bar 7 study reach (Figure 44). This was also seen for surface tracer results for the 2019-20 deployment year for both the Bar 6 and Bar 7 study reaches, suggesting the bar apex is a key morphological unit of deposition, with the greatest number of tracers trapped at these two reaches. At the reach scale, the biggest difference can be seen between the Bar 15 study reach and the other two study reaches, where the majority of buried tracers for the 2019-20 deployment year were trapped at the bar head and few were deposited at the apex (Figure 44). Although, surface tracers at the Bar 15 study reach for the 2019-20 deployment year had high deposition at the bar apex. This suggests that at high enough peak flows, tracers seeded in both the subsurface and surface near the bar head will most likely become trapped at the bar apex at all three study reaches, with few exceptions. Lastly, grain-size patterns show that the largest-sized grain size classes of tracers were deposited at the nearest downstream morphological unit, travelling shorter distances, relative to the smaller

grain size classes. As well, only the smallest two grain-size classes of recovered mobilized buried tracers were deposited at the bar tail, suggesting grain-size sorting of bars influences both surface and subsurface tracer dispersion.

5.5.5 Comparison Between Buried and Surface Tracer Dispersion

Similarities in pathlength distribution between surface and buried tracers are apparent, with exceedance probabilities of surface and buried tracers at the Bar 7 study reach exhibiting similar shaped distributions, (Figure 43). This is also the case at the Bar 6 study reach for the 2020-21 deployment year, where the shape of the exceedance probability distribution, as well as median pathlength distances for surface and buried tracers are similar (Figure 43). Furthermore, Bar 15 buried and surface tracers for the 2019-20 year also had a similar-shaped pathlength distribution, although the difference in median and maximum pathlength distance between surface and buried tracers is much greater relative to the other two seeding sites (Figure 43). The similar shaped distributions can be attributed to the similar patterns of morphological deposition for buried and surface tracers at each seeding site for the same deployment year.

Bar 7 buried and surface tracers for the 2019-20 deployment year both had high deposition at the bar apex, with Bar 15 buried and surface tracers both having the majority of deposition at the head of the bar. For the 2020-21 deployment year, overall pathlength distances for Bar 6 and 7 buried and surface tracers were shorter relative to the prior deployment year that saw the 100 year flood event, however both surface and buried tracers still had similar depositional patterns to each other, with the majority of tracers depositing closer to the seeding site at the head and apex of bar 6X.

Overall, once mobilized, tracers that are initially buried in the subsurface exhibit similar tracer dispersion characteristics to surface tracers at the same seeding location. The similar pathlength distributions and depositional patterns between surface and buried tracers provide strong evidence of morphological control with both surface and buried tracers becoming trapped in the same depositional area for the same deployment year. Furthermore, both surface and buried tracers at all seeding sites and both deployment years, rarely exceed one riffle-pool-bar unit, even when subject to a 100-year flood event, suggesting that at a certain threshold, flow is no longer the control and particle pathlengths become governed by morphological constraint.

5.5.6 Scour and Fill

Buried tracers were initially seeded at either 10, 20, or 30cm depths, to better understand the process of scour and fill at pool tailout margins in the San Juan River. Digital Elevation Models (DEMs) extracted from UAV imagery collected in July of 2020, post 2019-20 tracer recovery, are used to display the spatial variation of scour and fill of immobile buried tracers, where useful. Percent scoured, refers to the number of tracers that were subject to scour at depths equal to or greater than the initial burial depth of the tracer, out of the total number of recovered buried tracers. In some cases, there was scour up to the initial burial depth, but the tracer was not subsequently mobilized (moved >10m downstream). Furthermore, some tracers were found in the wetted channel, and no final burial depth could be measured. However, using both field measurements (measuring tape) for physically recovered tracers as well as recovered GPS waypoints, most tracers were able to be accurately identified as scoured or not; only four tracers had to be excluded from the analysis.

5.5.6.1 Scour

Scour results of buried tracers at the three study reaches are presented in Table 12. Scour of buried tracers varied between study reaches as well as within a study reach (Table 12). There was full scour (all tracers were scoured to initial burial depth) at the Bar 7 study reach for both deployment years (Table 12). The Bar 6 study reach had only partial scour of recovered buried tracers for both the 2019-20 and 2020-21 deployment year (Table 12). The Bar 15 study reach also had partial scour of recovered buried tracers for the 2019-20 deployment year, with no tracers being scour for the 2020-21 deployment year at the Bar 15 study reach (Table 12).

Table 12. Scour results of buried tracers. N_A represents the number of tracers used in the analysis.

Year	Initial Burial Depth (cm)	Bar 6		Bar 7		Bar 15	
		N_A	% Scour	N_A	% Scour	N_A	% Scour
2019-20	10	12	17	6	100	10	100
	20	12	0	8	100	11	100
	30	11	0	10	100	10	90
2020-21	10	8	100	9	100	12	0
	20	10	100	8	100	12	0
	30	11	55	7	100	12	0

For the 2019-20 deployment year, the Bar 6 study reach had the most limited scour depths, with only two tracers subject to scour up to 10cm depths (Figure 45). Surprisingly, the Bar 6 study reach experienced greater scour in 2020-21 deployment year, relative to the previous year that experienced the extreme flood event. With 100% scour of tracers at both 10 and 20cm depths, and 55% (6 out of 11 tracers) scour at 30cm depths at the Bar 6 study reach for the 2020-21 deployment year (Figure 45). The Bar 15 study reach had significant scour for the 2019- 20 deployment year, with 100% scour of tracers at 10 and 20cm depths, and 80% (8 out of 10 tracers) scour at 30cm initial depths. The Bar 15 study reach did not experience any scour of deployed tracers for the 2020-21 year, with Bar 15 surface tracers also subject to limited mobility for the 2020-21 deployment year. This can be attributed to channel changes and subsequent changes to the flow trajectory, leading to reduced mobility and scour near the bar 15 deployment location.

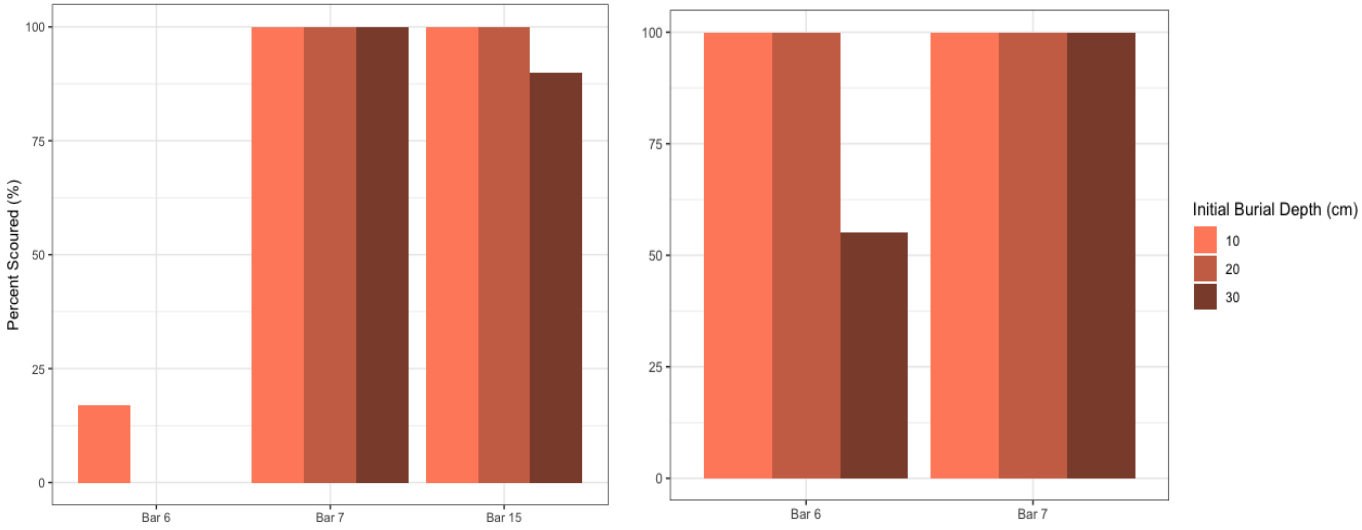

Figure 44. Percent scour (%) of recovered buried tracers that were included in analysis for the 2019-20 (left) and 2020-21 study year (right).

Overall, results show that scour is highly spatially variable and reach-dependent, with all three study reaches experiencing different scour extents in both deployment years (Figure 45). For the Bar 6 study reach, it appears that although peak flows do play a role, there may be other factors, such as bed texture, with a migrating gravel bed sheet observed at the Bar 6 study reach from 2015-2019 (McQueen, 2019; McQueen et al., 2021). Furthermore, the Bar 7 study reach experienced full scour up to 30cm depths even during years of moderate flood events. This suggests that scour in

the San Juan River may occur at significant depths (up to 30cm) during any year that experiences a typical moderate flood event. Furthermore, the spatial distribution of scour at the reach-scale can vary greatly, with the Bar 6 and Bar 7 study reach experiencing either limited or no scour (< 10cm depths), while the Bar 7 study reach experienced full scour of all tracers, up to 30cm depths, all subject to the same peak flood events. In summary, for the limited sampling data collected for buried tracers, scour appears to be unpredictable beyond the fact that scour up to and above 30cm depths is possible in some locations in any year subject to a moderate flood event. To further understand the influence of bed morphology, the spatial distribution of scour can be assessed.

5.5.6.2 Spatial Distribution of Scour

DEM's extracted from UAV imagery collected in July 2020 are used to help identify patterns in the spatial distribution of scour that occurred at the Bar 6 study reach for both deployment years, as well as the bar 15 study reach for the 2019-20 deployment year. It is important to note that DEMs do not reflect any changes to the gravel bars that occurred during the 2020-21 deployment year.

Bar 6

For the 2019-20 deployment year, the two tracers that were subject to scour up to 10cm depths were in relatively close proximity to each other (Figure 46). The remaining 10 tracers that were initially buried at 10cm depths did not experience full scour and remained in place (Figure 46). Surprisingly, the two tracers that were scoured at 10cm depths were seeded in the transect furthest from the wetted channel that most likely experiences the greatest flow strength, further pointing to the role of bed texture, rather than flow, as the primary influence on scour at the Bar 6 study reach for the 2019-20 deployment year (Figure 46). These results show that scour at the Bar 6 seeding site during the 2019-20 deployment year was extremely localized.

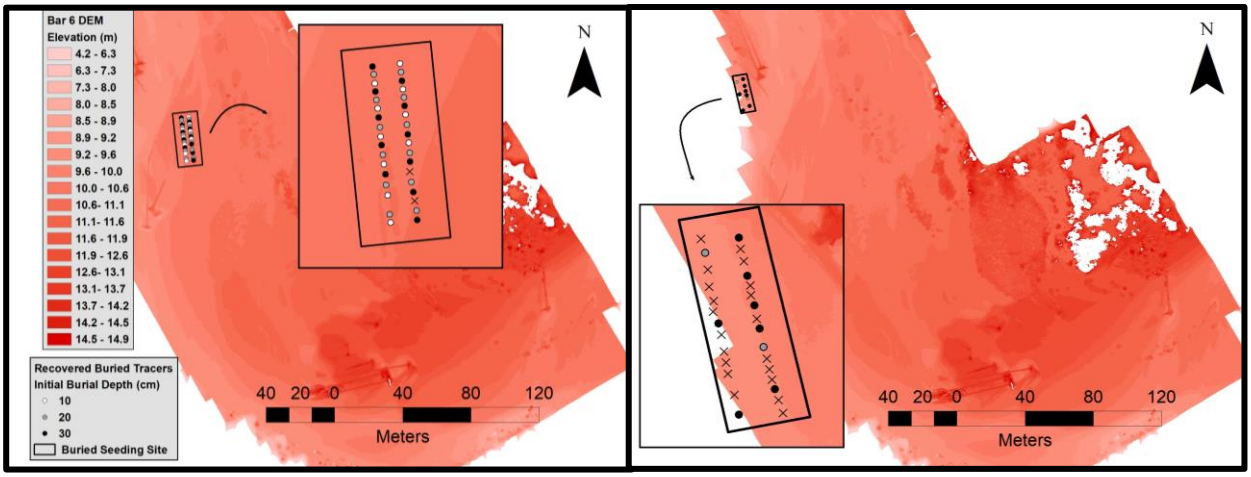

Figure 45. Spatial distribution of scour of recovered buried tracers at the Bar 6 study reach.

The spatial distribution of scour of recovered buried tracers at the Bar 6 study reach for the 2019-20 deployment year (pictured left) and the 2020-21 deployment year (pictured right) by initial burial depth (cm). X represents tracers that were fully scoured from the seeding site. burial depth

For the 2020-21 deployment, Bar 6 tracers experienced scour depths up to 30cm, with all recovered tracers initially buried at 10 and 20cm depths subject to scour (Figure 46). Two tracers initially buried at 20cm depths appear to have remained in place, however they were found at the surface (0cm depths) and therefore were still subject to 30cm scour depths. Only 55% of the tracers initially buried at 30cm depths (6 out of 11) were scoured. Interestingly, only one of the tracers initially buried at 30cm depths seeded in the transect farthest from the wetted channel was scoured, suggesting that for the 2020-21 deployment year, peak flows played a greater role on the extent of scour of tracers (Figure 46). There was a pattern of greater scour in the transect closest to the wetted channel, however scour of tracers still appears to be highly localized at the bar 6 study reach for the 2020-21 deployment year (Figure 46).

Bar 15

For the 2019-20 deployment year, the Bar 15 study reach had 100% of tracers scoured up to 20cm depths, although one tracer initially buried at 10cm depths was not mobilized (moved <10m), but was found at the surface (Figure 47). Furthermore, all but one tracer (9 out of 10) was scoured to 30cm depths at the bar 15 study reach, for the 2019-20 deployment year. The only tracer that was not scoured up to 30cm depths was initially seeded at the farthest downstream position of the inner transect, farthest from the bar margin and wetted channel, and appears to be located in an area of

greater elevation (Figure 47). Results suggest that there may be scour up to 30cm depths in areas closest to the wetted channel during years of extreme flood events, which may have implications for salmon spawning habitat located near the channel center at the Bar 15 study reach.

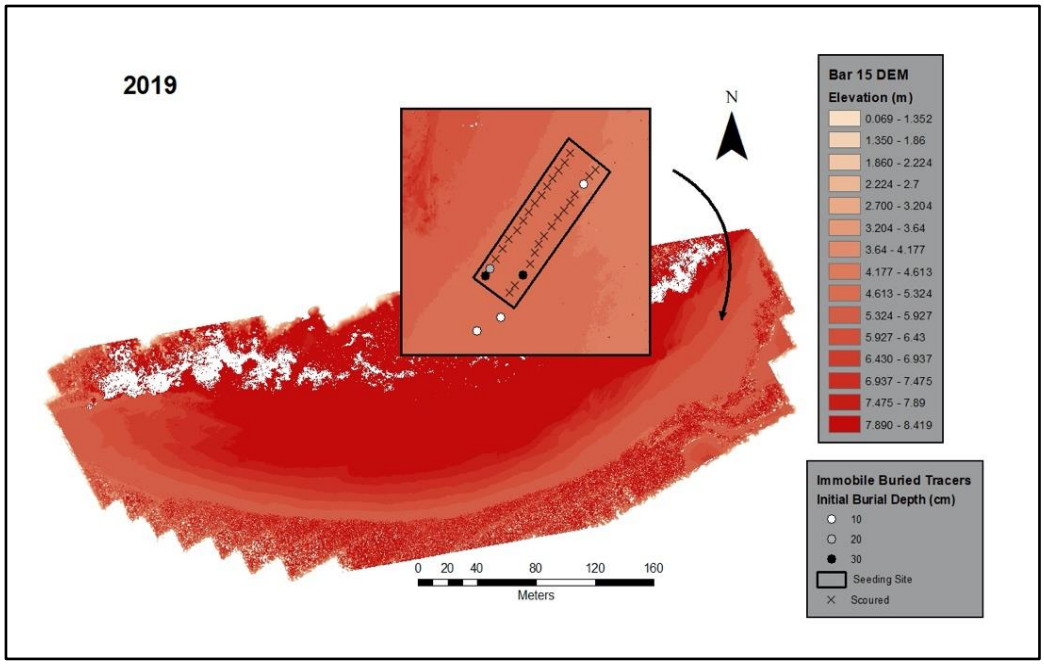

Figure 46. Spatial distribution of scour of recovered buried tracers (by initial burial depth) at the Bar 15 study reach for the 2019-20 study year.

5.5.6.3 Scour and Fill Depths

To better understand the active layer depth in the San Juan River, the net burial depth change (cm) of recovered buried tracers that remained in place at the initial seeding location were analyzed. The net burial depth change (cm) is calculated by taking the difference between the final and initial burial depths of recovered tracers, which includes tracers that were scoured, but remained at the seeding site. However the net burial depth change does not include the final burial depths of mobilized tracers. The net burial depth change of tracers were analyzed at the Bar 6 study reach for the 2019-20 deployment year, as well as, the Bar 15 study reach for the 2020-21 deployment year (Figure 48; Figure 49).

Median net burial depth change for recovered tracers was similar for tracers seeded at all three initial burial depths (Figure 48). The median net burial depth change for Bar 6 tracers initially

buried at 10cm, 20cm, and 30cm initial depths was 12cm, 11.3cm, and 12cm respectively (Figure 48). The maximum net burial depth change, which is equivalent to the maximum exchange depth of the active layer at the seeding site was 27cm (Figure 48). The positive median net burial change represents an overall net fill, suggesting that the bar 6 study reach for the 2019-20 deployment year was a site of deposition. Results also show that deposition was relatively equal across the seeding site and that the two tracers that were mobilized at this site, may have escaped before burial happened, or earlier on in the same flood event.

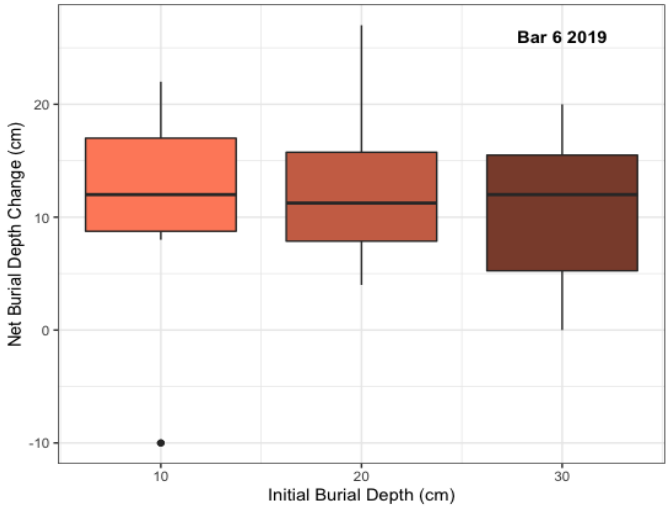

Figure 47. Median net burial depth change (cm) for recovered buried tracers at the Bar 6 study reach for the 2019-20 study year.

In contrast to the Bar 6 study reach for the 2019-20 deployment year, the Bar 15 study reach seems to have had a more limited active layer exchange, with overall negative depth change, suggesting the seeding site was an area of erosion for the 2020-21 deployment year (Figure 49). Similar to the Bar 6 tracers for the 2019-20 deployment, median net burial depths were relatively equal across the three initial burial depths (Figure 49). The median net burial depth change for tracers was -4cm, -3.5cm, and -4cm for tracers initially seeded at 10, 20, and 30cm depths respectively (Figure 49). The maximum net burial depth change, which is equivalent to the maximum exchange of the active layer was -12cm, suggesting that the Bar 15 study reach deployment location experienced a less dynamic active layer for the 2020-21 deployment year relative to the Bar 6 deployment location for the 2019-20 deployment year. The minimal burial depth change is reflective of the limited bed

movement that occurred during the 2020-21 deployment year at the Bar 15 study reach, which was also apparent in surface tracer results.

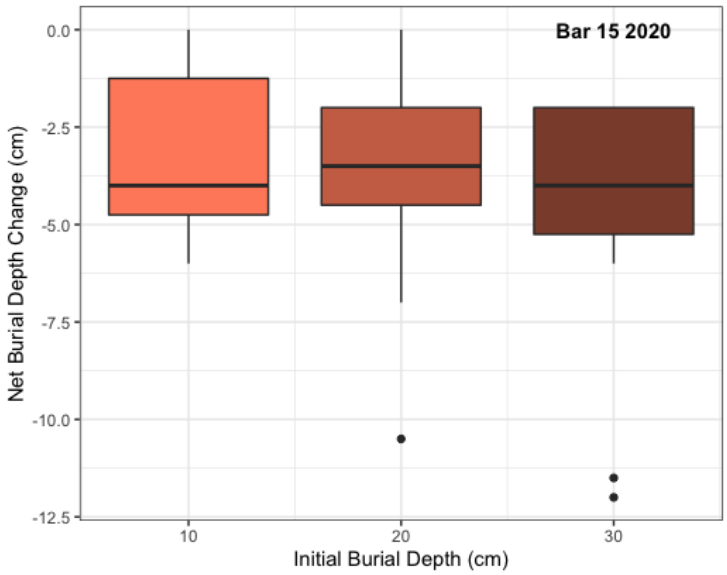

Figure 48. Net burial depth change (cm) for recovered buried tracers at the Bar 15 study reach for the 2020-21 study year.

5.5.6.4 Spatial Distribution of Scour and Fill

Bar 6

The active layer exchange depth at the Bar 6 study reach for the 2019-20 year, was further analyzed by assessing the spatial distribution of net burial depth change at the seeding site. DEMs extracted from aerial imagery collected in July 2020 are used to display the net burial depth change. Although overall median net burial depth change was similar between grouped tracers at initial 10, 20, and 30cm depths suggesting an even distribution of scour, closer analysis of the spatial distribution shows variation between closely seeded tracers (Figure 50). Overall, individual tracers were subject to similar net burial depth change when in close proximity (Figure 50). Furthermore, the transect seeded closest to the wetted channel, appears to have slightly smaller net burial depth change relative to the farthest transect (Figure 50). Although differences are seen between tracers within the seeding site, the relative difference is quite small, especially for tracers in close proximity. The local bed texture most likely plays a dominant role in the apparent differences in exchange depths

at the seeding site, however the subsurface grain-size distribution at deployment was not able to be measured in this study.

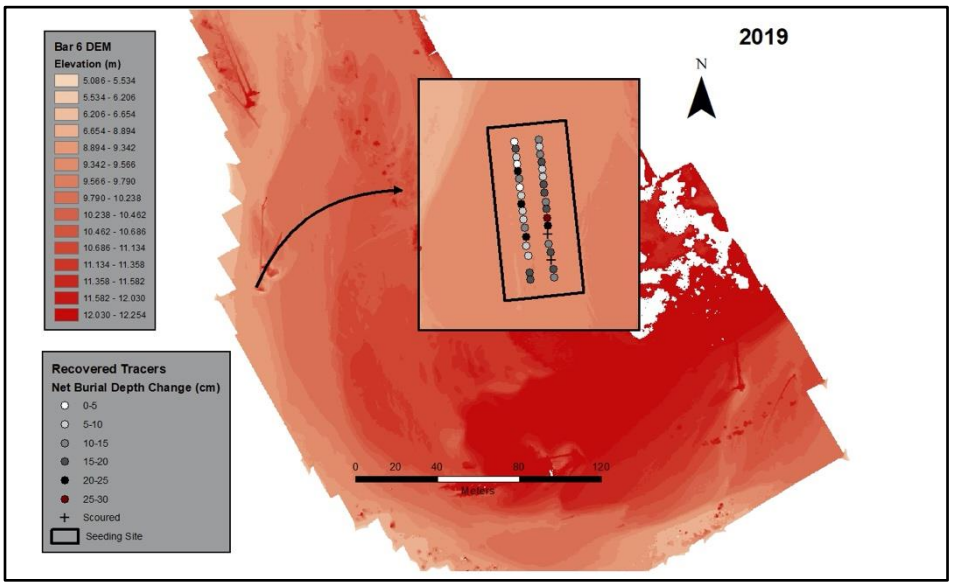

Figure 49. Spatial Distribution of scour and fill at the Bar 6 study reach for the 2019-20 deployment year.

The spatial distribution of scour and fill is depicted by net burial depth change (cm) at the Bar 6 study reach for the 2019-20 deployment year. X represents tracers that were fully scoured from the seeding site.

Bar 15

The active layer exchange depth at the Bar 15 study reach for the 2020-21 deployment year was also further analyzed by assessing the spatial distribution of net burial depth change at the seeding site. A DEM of Bar 15 from 2020 aerial imagery is also used to visualize the net burial depth change at the Bar 15 deployment location, however the DEM does not reflect any channel changes that occurred during the 2020-21 deployment year. Overall, buried tracers at the Bar 15 seeding site were subject to similar net burial depth changes (Figure 51). However, there are a few differences between net burial depth change of adjacent tracers at the Bar 15 seeding site. Three tracers that experienced a net scour between 10-15cm, had adjacent tracers only experiencing a net scour between 0-5cm (Figure 51). A 10cm difference between the amount of scour experienced at a 1m scale (tracers were initially spaced ~1m apart) suggests there is high spatial variation of active layer exchange depths at a localized scale. As mentioned for the bar 6 seeding site, similar

influences of subsurface bed texture may explain the differences in net burial depth change of Bar 15 tracers for the 2020-21 deployment year, although more research is needed.

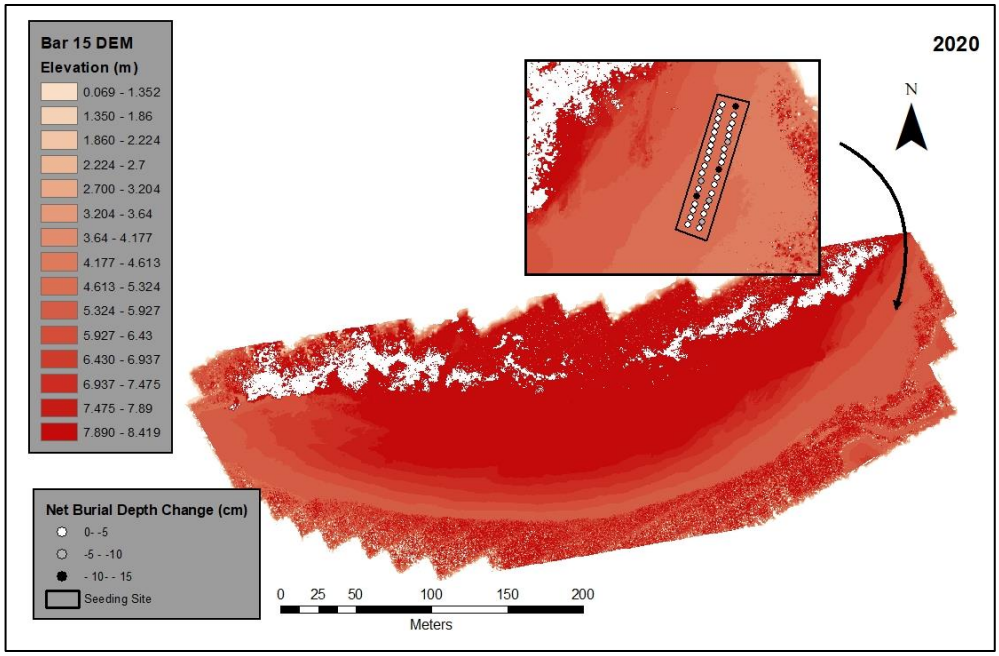

Figure 50. Spatial Distribution of scour and fill at the Bar 15 study reach for the 2020-21 study year.

5.5.7 Burial Depths of Mobilized Tracers

To further investigate the active layer depth, tracer burial depth data at the Bar 15 study reach for the 2019-20 deployment year are analyzed and compared to surface tracer burial depth results (Figure 52). There is limited burial depth data because of either low mobility, a high number of tracers being unrecoverable due to burial at undetectable depths, as well as tracers being deposited in the wetted channel that could not be recovered. Furthermore, the sample size of deployed buried tracers at each of the three study reaches was small to begin with (N = 36). Median burial depth is used to assess the data, as tracers that could not be detected with the wand antenna (> 50cm) were not physically dug up and accurate burial depth is unknown. Tracers that were buried beyond wand detection depths were assumed to be buried at 50cm, which was the assumed burial depth used for previous tracer results; therefore burial depths are a conservative estimate.

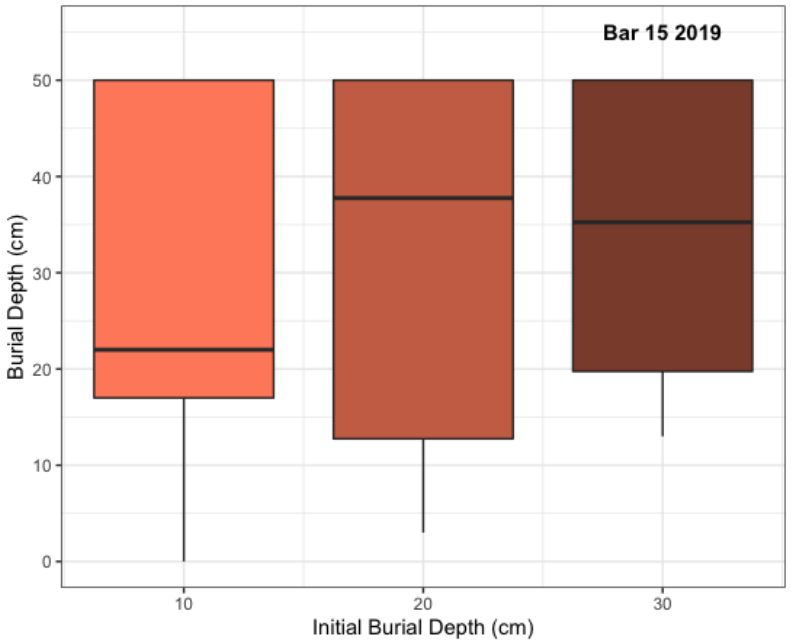

Figure 51. Recovered burial depths of mobilized buried tracers at the Bar 15 study reach for the 2019-20 year.

Bar 15 tracers for the 2019-20 deployment year had high median burial depths, with a median burial depth of 22, 37.8, and 35.3cm for tracers initially seeded at 10, 20, and 30cm depths respectively (Figure 52). The median burial depth of Bar 15 buried tracers is similar to the median burial depth of bar 15 surface tracers for the 2019-20 deployment (21.8cm), suggesting that tracers mobilized from either the surface or subsurface experience similar burial depths. Importantly, the majority (~75%) of recovered buried tracers were found at depths exceeding twice the D_{90}, which is equal to 17.7cm for the Bar 15 study reach. Burial depths exceeding twice the D_{90} were also seen in the 2019-20 and 2020-21 surface tracer results as well as from previous trace work (2016-2018) on the San Juan River (McQueen, 2019; McQueen et al., 2021).

5.6 Summary of Results

Results from both surface and subsurface particle tracking on the San Juan River provide valuable insight on tracer dispersion at the reach-scale. Recovery of surface and buried tracers was high for both deployment years. Mobility and pathlength distances of recovered surface tracers varied between reaches, with high mobility at pool tailouts at the three study reaches, with the exception of the bar 15 study reach for the 2020-21 deployment year. Tracer pathlength distances show a

positive relationship with peak flows, although the relationship appears weak for all flow metrics, which include peak flow and flow duration variables. Additionally, subsurface and surface tracer pathlength distributions were similar at the same reach, with tracers becoming trapped at the same depositional macroform units, further highlighting a strong morphological control on tracer dispersion across the entire active layer depth. Scour and fill of buried tracers also varied between reaches, with high spatial variation of scour at the local scale (within the reach). Results from this study will be compared with results from the literature, including work from a previous 4-year particle tracking study on the San Juan River, in section 6.

6 Discussion

Results of surface tracer particle mobility and characteristics of pathlength dispersion are discussed in section 6.1, along with a discussion of the influences of flow, grain size, and channel morphology. Surface tracer pathlength characteristics are further compared to subsurface tracer pathlengths in section 6.2. Results of scour and fill of initially buried tracers as well as burial depths of recovered surface tracers are discussed with the literature on the active layer depth in gravel-bed rivers and scour risk to physical spawning habitat (section 6.3). Section 6.4 discusses recovery rate results on the San Juan River, relating to particle tracking work done on similar gravel bed rivers. Lastly, section 6.5 discusses resulting implications on the risk to salmonid species in the San Juan River, as well as a discussion of broader implications for restoration work done on similar rivers subject to disturbance.

6.1 Surface particle mobility and pathlength dispersion

The two year surface tracer dataset collected in this study can provide insight into individual particle mobility at pool-tailouts in a large wandering gravel-bed river at three distinct study reaches (Bar 6, 7, 15). For the 2019-20 deployment that saw the 100-year extreme flood event, all three study reaches experienced near full mobility of recovered surface tracers. The subsequent 2020-21 deployment year that was subject to a more moderate flood event (~1.5yr recurrence) saw near full mobility at two of three reaches, with the Bar 15 reach subject to partial (~55%) mobility. Mobility results are similar to McQueen's (2019) previous tracer deployment results for the same three study reaches, with near full mobility of tracers with the exception of partial mobility at the Bar 15 reach for the 2016-17 deployment year that saw a similar flood event (~1yr recurrence) to the 2020-21 deployment year that also experienced partial mobility at the Bar 15 study reach.

Pathlength distances for recovered surface tracers differed between the two deployment years. Recovered surface tracers from the 2019-20 deployment year had greater average pathlength distances at all three study reaches, ranging from 303m – 394m, relative to pathlength distances of tracers from the 2020-21 deployment year as well as to the previous three years of tracer results at the three study reaches (McQueen, 2019). The significant increase in average and maximum pathlength distances of tracers for the 2019-20 deployment year can be attributed to the 100-year flood event (Q_p = ~1360m^3/s) that occurred January 2020, and will be discussed further in the

following subsection. The pathlength distances of tracers for the 2020-21 deployment year with Q_p = ~735m^3s^{-1}, ranged from 139.4m – 253.3m which are similar to results from previous tracer deployment years that had comparable peak flood events in 2016-2017 deployment with Q_p = 749m^3s^{-1} and for the 2018-19 deployment year with Q_p = 942m^3s^{-1} (McQueen, 2019; McQueen, 2021).

Furthermore, average pathlength distances of tracers were much greater compared to results from previous tracer tracking studies on similar gravel-bed rivers. Rollet et al. (2008) used PIT tags to track particles seeded at the head of gravel bars in the Ain River, France, a large bar-dominated gravel-bed river (Q_p = 800m^3s^{-1}) for a one-year period and saw an average pathlength distance of just 50m. On the Durance River, France, that saw a similar peak flood event (Q_p = 1156m^3s^{-1}) to the 100-year flood event for the 2019-20 deployment year on the San Juan, results from a particle tracking study with tracers seeded from the mid to lower portion of the gravel bar saw an average pathlength distance of 83m for recovered tracers (Chapuis et al., 2015). Differences in average pathlength distances between the Durance and San Juan River may be explained by the greater average channel width (240m) that characterizes the Durance River (Chapuis et al., 2015) relative to the average channel width (67m) of the San Juan study reaches, where flow will be more constrained and thus lead to greater pathlength distances of tracers on the San Juan River. Discrepancies in pathlength distances observed on the San Juan and previous tracking studies may also be in part due to recovery differences, with both the Ain and Durance River having low recovery rates (~40%) which may have led to an underrepresentation of particle pathlength distances (Rollet et al., 2008; Chapuis et al. 2015). Additionally, differences in seeding locations may have an influence in resulting pathlength distances. Both Liebault et al. (2012) and Chapuis et al. (2015) noted that tracers seeded closer to the thalweg experienced greater transport distances, which is reflective of the higher pathlength distances observed on the San Juan for this study where tracers were seeded exclusively in the wetted channel at pool-tailout locations (Liebault et al., 2012).

Pathlength distributions of recovered surface tracers differed between deployment years as well as between study sites, highlighting the spatial variation of particle dispersion at the reach-scale as well as temporal differences that may be explained by differences in annual peak flood events. Tracer pathlengths for both deployment years and all three study reaches followed either a multi-

modal or bi-modal right-skewed distribution, similar to previous tracer results on the San Juan River and provides further validation of the bi- and multi-modal pathlength distributions that resulted from flume experiments of bar-dominated channels (Pyrce & Ashmore, 2003a; McQueen, 2019; McQueen et al., 2021) . For two of the three reaches, individual pathlength distributions also reflected large-scale bar development patterns that are typical of large wandering gravel-bed rivers, with high deposition at the apex and bar-pool margins (Church & Rice, 2009). Pathlength distributions from this study indicate a strong morphological role in particle dispersion at the reach scale, that is complicated by the influence of both flow and grain-size.

6.1.1 Influence of Flow

The influence of flow on mobility rates and pathlength distances for this study as well as three previous deployment years (McQueen et al., 2021) were tested against three flow metrics, peak discharge (Q_p) which considers only the magnitude, as well as excess energy of the peak flood event (Ω_P) and total excess energy of all flood events above bankfull (Ω_T) which considers both magnitude and duration of flows. In general, mobility rates increased with increasing flow on the San Juan River, with the additional two years of data from this study strengthening the relationship from McQueen's (2021) results because of the January 2020 extreme flood event, and agrees with the literature (Wilcock, 1997; Haschenburger & Wilcock, 2003; Papangelakis et al., 2016). However, there was no clear relationship between mobility rates and any of the three flow metrics, which may be caused by the limited sample size (n = 5). Furthermore, all five deployment years saw near full mobility, with only two years where partial mobility occurred at one of the study reaches, leaving little variation to explain. This suggests that on the San Juan River, most flows near or above bankfull (1.5-2 year flood event) cause full mobilization of the bed. Previous results from a particle tracking study in a small stream using magnetic tracers differ, where the bed remained in a state of partial-mobility during a 2-year flood event and only reached full mobility during a 7-year flood event, however the San Juan River is of much larger size and subject to peak flood events up to 10^3 higher (Haschenburger & Wilcock, 2003). Differences in mobility rates between the San Juan River and the majority of previous particle tracking studies may be explained by the armored bed that is more common for smaller streams and rivers (Wilcock & McArdell, 1997; Church et al., 1998) and highlights the need for continued field observations on particle mobility in large gravel bed rivers.

Pathlength distances for all three study reaches generally increased with increasing flow, a dominant trend throughout the literature (Hassan et al., 1992; Schneider et al., 2014; Bradley, 2017). Pathlength distances showed high correlation to all three flow metrics with two study reaches yielding strongest relationships with the flow metric that only considers the magnitude of the peak flood event (Q_p), although there is significant variation left unexplained and the small sample size (N = 5) limits the validity of any significant relationships seen. The weak relationship between pathlength distances and the two flow metrics that considers duration, suggest that particle transport in the San Juan River is mostly controlled by the magnitude of peak flows, which supports findings from a recent analysis on a large tracer dataset that found a strong relationship between peak stream power (a similar flow metric) and pathlength distances, while also noting large amounts of scatter in the data (Vasquez-Tarrio et al., 2018).

Differences between reaches are apparent, with tracer pathlength distances at the Bar 15 study reach being most strongly correlated to the flow metric that considers both magnitude and duration of all flows above bankfull (Ω_T). Further evidence of between-reach differences is seen in the weak relationships between scaled pathlength distances of all study reaches combined and both Ω_P and Ω_T. Reach-scale differences between the relationship of pathlength distance and increasing flow on the San Juan River suggests a strong morphological influence on tracer dispersion, which was also seen by Vasquez-Tarrio et al. (2018) where a meta-analysis of pathlength distances in relation to flow exhibited some scale dependence on the channel morphology. Additionally, individual tracer pathlengths on the San Juan River rarely exceeded one riffle-pool-bar unit, even for the deployment year subject to the most extreme flood event (2019-20), providing further evidence of morphological control on tracer dispersion at the reach scale.

6.1.2 Influence of Grain Size

No influence of grain size on particle mobility was observed in this study which was also the case for previous particle tracking work on the San Juan River, as near full mobilization occurred for all grain size classes, with few exceptions (McQueen, 2019). Previous studies done on smaller streams also saw limited grain size influence on mobility of particles < D_{50} (Church & Hassan, 1992; Papangalakis & Hassan, 2016; Ferguson & Wathen, 1998), thus offering a possible explanation for the lack of observed grain-size trends on the San Juan River where the grain size distributions were skewed to the smaller size classes. Furthermore, McQueen (2019) also noted

that stronger size-sorting effects due to complex bar development and morphological patterns suggests the controls on grain size sorting and overall tracer dispersion may be different for larger rivers compared to smaller, uniform streams.

For the 2019-20 deployment year, subject to the 100 year flood event, there was a general trend of decreasing pathlength distance with increasing grain size, which has been well documented in the literature (Church & Hassan, 1992; Milan et al., 2002; Liebault et al., 2012; Schneider et al., 2014). Furthermore, the 2019-20 study year saw differences in grain size trends between study reaches, suggesting the relationship between grain size and pathlength distance may vary due to the dominant role of channel morphology, especially in reaches that have more complex morphological features. However, for the following deployment year that saw a more moderate peak flood event, either very weak or no grain size trends were observed at the three study reaches, which was also the result from previous tracer work on the San Juan River (McQueen, 2019). Results from the San Juan River suggest grain size influences may be most apparent during years of more extreme food events when the majority of morphological work to the channel occurs, especially in relation to size-sorting processes during bar formation which has also been previously observed in flume experiments at channel forming discharges (Pyrce & Ashmore, 2005).

Results from the analysis of tracer deposition as well as grain size distributions of the gravel bars at the three study reaches taken in July 2020, exhibit downstream fining and size-sorting patterns on the San Juan River. In almost all cases, the larger two size classes of tracers saw high deposition at the head of the bar, with deposition at the bar tail being almost exclusively of the smaller two size classes. Downstream fining is also apparent in the grain size distributions of the head, apex, and tail of the gravel bars at all three study reaches for the 2019-20 year. Observations of size-sorting and downstream fining of gravel bars on the San Juan River provide direct field evidence to support

6.1.3 Influence of Channel Morphology

Pathlength distribution characteristics shows strong evidence of the underlying morphological influence on bedload transport rates in large wandering gravel bed rivers and supports previous findings of individual particle dispersion linked to overall bar development and channel change on the San Juan River (McQueen et al., 2021). The apparent trapping zones of tracers focused at the

bar apex as well as bar-pool margins persistent over the five years of sediment tracking on the San Juan River (McQueen et al., 2021) provide field based evidence to corroborate flume observations of individual tracer displacement linked to bar development (Pyrce and Ashmore, 2003a; Kasprak, 2015). Furthermore, the tendency of tracers to remain within one riffle-pool-bar unit even during years of extreme flood events also suggests a strong underlying morphological control on bedload transport rates with implications for similar wandering gravel-bed rivers with complex bar development.

The increased trapping zones linked to bar development during years of higher peak flood events identified by McDowell and Hassan (2021) using field based probability modelling agree with observations on the San Juan River; where an increased number of particles were trapped at the bar apex and channel margins during the 2020-21 deployment year subject to the 100-year flood event. However, a study on long-term topographic change on the Lower Yuba River, California suggests moderate flood events with longer duration flooding leads to greater rates of geomorphic effectiveness (channel change) than higher magnitude flooding (Gervasi et al., 2021). This is in contrast to observations on the San Juan River, although differences in hydrological regime may provide an explanation, as well as the different temporal scales between studies.

In years of higher peak-flood events, tracer pathlength tended to follow a symmetrical distribution, compared to multi-modal and positively-skewed distributions observed for years subject to more moderate-flood events which supports findings in the literature (Pyrce and Ashmore, 2003a; McQueen et al, 2021; McDowell and Hassan, 2021). Furthermore, the shorter pathlength modes and minimal trapping rate of tracers at the bar apex and bar-pool margin observed at the Bar 15 study reach can be linked to the overall lower rate of channel change relative to the other two study reaches, supporting the idea of individual tracer displacement linked to long-term channel evolution (Kasprak et al., 2015; McDowell and Hassan, 2021; Gervasi et al., 2021).

Evidence of lateral accretion of gravel bars and subsequent erosion to the opposite bank from observations of individual tracer displacement and channel change on the San Juan River is similar to patterns of bar development and overall channel evolution previously described for wandering style gravel-bed rivers (Ham, 2005; Church and Rice, 2009). Previous studies that observed long-term channel changes in morphologically-complex rivers found evidence of increased channel avulsion and aggradation due to increased sediment supply to the river (East et al., 2017; Gervasi

et al., 2021), strikingly similar to observations of channel change on the San Juan River which was subject to increased sediment supply due to logging activities in the latter half of the 20th century (NHC Ltd, 1994). High rates of sediment transport and subsequent erosion to banks in the San Juan River can lead to reduction of pools and changes to transitional areas, specifically between pools and riffles (pool tailouts) (Hanrahan, 2007) and has important implications for physical salmon habitat.

6.2 Comparison of Pathlength Dispersion Between Surface and Buried Tracers

Recovered mobilized tracers that were initially buried at either 10, 20, or 30cm depths were analyzed to better understand how subsurface mobilization and subsequent pathlength dispersion contributes to the bedload volume within the study reach and compares to surface tracer dispersion. Subsurface and surface pathlength distributions of mobilized recovered tracers were strikingly similar at two of the three reaches especially for the 2019-20 deployment year subject to the extreme flood event with average pathlength distances also very similar. High trapping of subsurface and surface tracers at distinct depositional zones relating to the development and maintenance of morphological features, specifically gravel bars can provide an explanation for the apparent similarities (Mcdowell and Hassan, 2021). Furthermore, surface and subsurface pathlength distributions saw fewer similarities with subsurface tracers travelling shorter distances than surface tracers at the Bar 15 reach. At this reach, the morphological features are less developed and tracer dispersion may be more so governed by flow and grain size, leading to greater spatial and temporal variation of particle deposition which have been recognized as primary controls on overall bedload volumes in riffle-pool channels with more simple morphologies (Vasquez-Tarrio et al., 2021).

To the author's knowledge, no other studies have been done to assess and compare subsurface and surface pathlength distributions in a morphologically complex river system. This is also highlighted by Liebault & Laronne (2008) who used scour chains and painted surface tracers to estimate the bedload volume in the Esconavette Torrent, a small gravel-bed tributary, but highlighted uncertainty due to the underlying assumption that subsurface (scour chains) and surface (painted tracers) dispersion results in similar bedload volumes. Additionally, the only other use of RFID tracers buried in the subsurface is a recent study by Brousse et al. (2018), where active RFID tracers are seeded in a fixed column to survey event-based scour depths, therefore no information on

subsequent pathlength dispersion of subsurface particles can be gathered. Observations of subsurface and surface pathlength distributions in the San Juan River suggest reach-scale differences that are dependent on the morphological complexity of channel features. Results from this study on the San Juan River can provide novel insight for predicting overall bedload volumes using the morphological approach, however further research is required that captures a smaller temporal scale (event-based) and greater spatial variation in the deployment strategy to accurately quantify bedload transport rates in morphologically complex gravel-bed rivers.

6.3 The Active Layer Depth

6.3.1 Burial Depths of Surface Tracers

Burial depths of surface tracers varied spatially, and a large proportion of tracers were found at depths exceeding twice the D_{90}, which aligns with previous findings on the San Juan River (McQueen et al., 2021) and is commonly cited in the literature as the maximum value of the active layer depths in gravel bed rivers (Hassan, 1990). Burial depths of mobilized surface tracers also appear to be governed by flow strength, with greater median burial depths at two of the three study reaches during the 2019-20 deployment year subject to the extreme flood event, with previous findings of positive trends between active layer depths and flow metrics in the literature (Houbrechts et al., 2012; Mao et al., 2016). Furthermore, burial depths varied between study reaches, with significantly smaller median burial depths observed at the Bar 15 reach in both deployment years. Bar 15 is subject to lower rates of annual morphological change to the channel and subsequently experiences less elevation change (scour and fill) on an annual basis (McQueen et al., 2021) which may help to explain the smaller burial depths relative to the other two study reaches. This suggests the reach-scale morphology and complexity of the macro-bedform features may influence burial, with greater burial in more complex river reaches and those with greater elevation changes (scour and fill) during flood events. This observation is supported by a recent meta-analysis, which found that dominant macro-bedforms in riffle-pool channels control the way flow scales to active depths pointing towards an important morphological influence between flow and active layer depths (Vasquez-Tarrio et al., 2021).

The high rate of tracer burial beyond the maximum antenna detection depth (~0.5m) in the San Juan River suggests the current use of $2D_{90}$ as the maximum exchange depth of the active layer may lead to inaccuracies if used to predict overall bedload transport rates in large gravel-bed rivers.

In addition to tracer burial beyond the maximum antenna detection depths, low mobilization as well as a large proportion of tracers depositing in the wetted channel where burial depths cannot be measured were limitations to burial depth analysis for this study, and have also been noted in previous tracer work on the San Juan River (McQueen et al., 2021). Continued studies on the active layer depth, specifically for large dynamic rivers are needed, with promising recent work of passive (Papangelakis et al., 2019) and active RFID tracking (Brousse et al., 2018) methods, which along with increased antenna detection depths can improve the quality of data and therefore minimize the knowledge gap on active layer depths.

6.3.2 Scour and Fill of Buried Tracers

Full scour of all tracers at 10, 20, and 30cm depths occurred at the Bar 7 reach for both deployment years. Only partial or near full scour occurred at the other two seeding sites for both deployment years, highlighting the spatial variation of scour at both the reach scale and at the local scale (seeding site). Interestingly, scour rates at the Bar 6 study reach were greater for the deployment year that saw a more moderate flood event, compared to the previous deployment year that was subject to the extreme flood event where only two tracers were scoured. In summary, with the limited sampling data collected, scour at channel margins near pool tailouts in the San Juan River at the three study reaches appears to be unpredictable beyond the fact that scour up to and greater than 30cm is possible in some locations in any year subject to moderate flood events.

At the local scale, cross-sectional and longitudinal spatio-temporal variability of scour depths has been well documented in the literature (Rennie and Millar, 2000; May et al., 2009; Merideth et al., 2018) and is consistent with results on the San Juan River. In a mountain river in Utah, U.S.A, Meredith et al. (2018) measured 4cm differences in scour depths along a longitudinal gradient. The deployment strategy of longitudinal transects was also used for this study, and differences in scour depths within seeding sites was also observed with only some of the tracers at the same initial burial depths being scoured at 10, 20, and 30cm depths at two of the reaches. Furthermore, variability in net scour and fill depths suggest differences much greater than 4cm reported by Meredith et al., 2018, where maximum differences in net scour or fill of tracers that remained in place were up to 25cm. Rennie & Millar (2001) found no spatial autocorrelation in scour depths at a local (1m) scale, and suggested bed roughness variability and topography as a potential explanation. The complex morphological features attributed to the Bar 6 study reach in the San Juan River, which

contributes to bed roughness and variable topography at the seeding site may also be a potential explanation for the spatial variation in scour depths at this site. Furthermore, a migrating depositional gravel sheet has been identified at the Bar 6 study reach from previous tracer work (McQueen et al., 2021) which has been noted as a likely control on active depths in riffle-pool rivers with high sediment supply (Vasquez-Tarrio et al., 2021) and may explain the minimal scour experienced at this site for the 2019-20 deployment year subject to the most extreme flood event on record.

Peak stream power of the flow event as well as shear stress has been commonly cited in the literature as a control on scour depths (Rennie & Millar, 2000; May et al., 2009; Meredith et al., 2018) and overall scour and fill (active layer) depths (Gottesfeld et al., 2004; Habersack et al., 2008; Mao et al., 2016). However, the influence of flow is less apparent from results on the San Juan River, where greater scour occurred in years of weaker flood events at one of the three reaches suggesting that local bed texture governed by reach-scale channel morphology that varies annually is the primary control on scour depths near pool-tailout locations. However the limited data from only two deployment years with a small number of tracers buried at each site, as well as the larger temporal scale of the study most likely is not sufficient to identify the influence of flow.

Overall, evidence of scour at up to 30cm depths at channel margin locations on the San Juan River does not agree with previous findings in the literature which suggest only limited scour occurs away from the channel centreline (thalweg) (Montgomery et al., 1996; Rennie & Millar, 2000; May et al., 2009 Meredith et al., 2018). Scour depths up to 30cm for some buried tracers and subsequent net fill up to 50cm depths on the San Juan River provide further evidence that the exchange depth of the active layer, and thus the actual bedload volume may exceed previous theorized limits used in sediment transport modelling (Hassan, 1990; Haschenberger, 1999; Hassan & Bradley, 2017) with implications for other large-gravel bed rivers with complex morphology (McQueen et al., 2021). Implications of scour risk for physical salmon habitat will be discussed in section 6.5.

6.4 Tracer Recovery

Overall, recovery rates for surface tracers were high for the two deployment years of this study, and similar to previous recovery results on the San Juan River (McQueen et al., 2021). Recovery rates ranged from 60 – 76% for surface tracers at the three study reaches, with similar recovery

rates seen between years even with the extreme flood event for the 2019-20 deployment that resulted in greater pathlength distances and overall tracer dispersion. Furthermore, there appears to be differences in recovery between grain-size classes, with smaller grain size classes subject to lower recovery rates which was also noted by McQueen et al. (2021) on the San Juan River and other particle tracking studies (Papangelakis, 2015) which can lead to misrepresentation of tracer dispersion data across grain size classes. However, a recent classification system proposed by MacVicar and Papangelakis (2021) provides a potential strategy to be able to accurately infer tracer movement of unrecovered tracers, although this application requires a deployment strategy that monitors tracer positions over multiple events or specified time-intervals, which is not the case for tracer work on the San Juan River.

Although recovery rates were relatively high when compared to previous particle tracking work on large rivers (Rollet et al., 2008; Chapuis et al., 2015), limitations still exist. Tracer burial beyond maximum antenna detection depths as well as the clustering of tracers within the same area leading to signal interference seems to be a plausible limitation on tracer recovery on the San Juan River (McQueen, 2021) and has been noted in the literature (Lamarre et al., 2005; Chapuis et al., 2015; Arnaud et al., 2015). A recently designed synthetic tracer "wobble stone" which ensures the proper vertical orientation of the PIT tag to increase detection reading by the antenna, is a potentially viable solution to increase tracer recovery (Papangelakis et al., 2017). Furthermore, deep pools that are a potential high trapping area especially for smaller grain size classes of tracers (Milan et al., 2013) were searched using a boat towing a large antenna system and is a new recovery strategy used on the San Juan River, which resulted in a significant proportion of tracers recovered. Arnaud et al. (2017) also employed a similar boat surveying strategy which proved to be a successful recovery strategy on the Old Rhine River, and may be a viable recovery strategy for tracer work in large gravel-bed rivers.

The novel deployment strategy of initially buried tracers across longitudinal transects also resulted in high recovery rates, ranging from 69 – 100% for the three study reaches over both deployment years. For the Bar 7 reach where 100% of tracers were subsequently mobilized, recovery rates were lower, and more closely matched to recovery rates of surface tracers. The ~1m spacing of initially seeded buried tracers did not lead to signal interference and recovery remained high when all tracers stayed in place. As well, most tracers that remained in place and were subject to high burial

were also able to be recovered by locating the initial seeding site and digging along the longitudinal transect. Overall the deployment strategy of buried tracers seems to be a viable method to assess scour and fill as well as active layer depths in large gravel bed rivers. A similar, yet more constrained deployment strategy for use of RFID tracer tracking in the subsurface, was proposed by Brousse et al. (2018) by drilling a vertical cylindrical column of active RFID tracers into the subsurface of the bed, which is the only other study that has used RFID tracers, rather than scour chains to study active layer depths. A limitation to this study was the inability to bury tracers closer to the channel thalweg (centre) where spawning activities occur on the San Juan River (Burt and Palfrey, 2011). As particle tracking technology continues to be developed, deployment strategies that allow for unconstrained tracers (tracers that can become mobilized and dispersed) to be buried in the deepest part of the wetted channel should be considered, to further understand the active layer depth and subsequent particle dispersion at the subsurface.

6.5 Implications for Salmon Habitat and Future Restoration Work

The overarching goal of geomorphic investigations on the San Juan River is to provide background information to help improve and restore physical habitat for salmonid species in the river (NHC Ltd, 1994; Burt and Palfrey, 2011). One of the main objectives of this study directly aligns with this goal, which is to examine scour depths at channel margins, adjacent to spawning habitat at pool tailout locations. Furthermore, reach-scale annual channel change was also observed along with individual particle dispersion at the three study reaches which provides useful insight into the overall channel stability of the San Juan River.

During winter high flows, salmon eggs buried in the subsurface at pool tailouts are at risk of bed erosion (scour) and consequent decreased survival rates of embryos (Montgomery et al., 1996; Baxter and Hauer, 2000). Results from this study show that scour can occur at some channel margin locations at up to 0.3m depths during any year subject to moderate flood events, at or above bankfull. Although exact egg burial depths for salmonid species spawning in the San Juan River is unknown, commonly used criteria in the literature suggest egg burial depths begin at 0.1 – 0.15m depths for all five Pacific salmonid species in the San Juan River (Devries, 1997). Therefore, results suggest salmonid eggs in the San Juan River may be at risk of scour on an annual basis. Although scour could not be directly measured at the channel thalweg, where spawning occurs in the San Juan River, scour depths greater than egg burial depths measured at channel margins can be used

as an indication of scour risks, which may be even greater closer to the channel centre which has been a dominant observation in the literature (Montgomery et al., 1996; May et al., 2009; Merideth et al., 2018).

Furthermore, individual tracer dispersion related to high rates of bar development and subsequent erosion of the opposite bank, recognized in annual channel change observations at the three study reaches, suggest the San Juan River may be relatively unstable in some areas. High rates of bank erosion can also lead to increased fine sediment contributed to the river, and may have consequences for physical spawning habitat due to infilling of fines leading to suffocation of buried salmonid eggs (Buxton et al., 2015). At the reach scale, evidence of local variation in sediment entrainment and subsequent deposition associated with the formation of bars and islands, may lead to a decrease in important physical habitat for salmonids such as deep pools and transitional areas (pool tailouts) (Hanrahan, 2007). Overall, particle dispersion, active layer depths, and overall channel change provide evidence of a high sediment supply at the three study reaches on the San Juan River. This may be a consequence of logging activities that occurred during the latter half of the 20th century, although sufficient knowledge on sediment movement through the mainstem channels and tributaries of the San Juan River, make it difficult to accurately identify all factors (NHC, 1994). Individual particle tracking at the surface and subsurface, together with aerial imagery to identify concurrent reach-scale annual channel change, has provided useful insight into the overall channel stability at the three study reaches while also providing important information on the risk of scour at known salmon spawning habitat in the San Juan River.

7 Conclusions

This study involved a two-year dataset of tracked bed particles seeded at the surface and subsurface at three distinct study reaches in the wandering, gravel-bed San Juan River. Results from this particle tracking study show high surface particle mobility at pool tailout locations, with near full mobility experienced, even during moderate flood events. This differs from particle tracking results on smaller streams and rivers, where full mobilization of surface particles only occurs during the most extreme flood events. Average pathlengths of surface tracers ranged from 139m – 394m over the two deployment years, which is similar to previous tracer results on the San Juan River (McQueen et al., 2021). Furthermore, results from the flow analyses that also incorporated particle tracking data from previous tracer work on the San Juan River (McQueen et al., 2021) indicate that the magnitude of the peak flood event seems to be a greater control on expected pathlength distances, rather than flow duration.

Pathlengths of subsurface and surface tracers seeded at the same reach saw similar distributions. As well, less than 10% of tracers travelled farther than one riffle-pool-bar unit even during the 2019-20 deployment year subject to the extreme flood event. This suggests a strong morphological control on individual pathlength dispersion along with the influence of flow. Furthermore, identifiable trapping areas linked to bar development at the bar apex margins saw consistently high tracer deposition year to year, with observations of significant erosion to the opposite bank. This provides key insight into the processes of bar development at the individual particle scale in large wandering gravel-bed rivers, and also provides information on the relative channel stability at the three study reaches.

Grain size did not appear to influence particle mobility. However a significant trend of decreasing pathlength distance with increasing grain size was observed for surface tracers for the 2019-20 deployment year. Results suggest grain size influences may be most apparent during years of more extreme flood events when the majority of morphological work to the channel occurs, especially in relation to size-sorting processes during bar formation. Although all sizes are mobilized, morphologically significant floods allow size sorting on bars with finer particles travelling to the bar tail while coarser particles, although mobile, deposit at the bar head or apex.

Scour of tracers initially seeded in the subsurface varied between study reaches and also had high spatial variation within the study reach. Results indicate that in some locations in the San Juan River, scour may occur up to 0.3m depths, even in years of moderate flood events. Scour and fill results of initially buried tracers, along with observations of surface tracer burial depths, indicate the active layer depth in the San Juan River may be closer to 30cm; which is much greater than the equivalent to $2D_{90}$ (~20cm), commonly used in sediment transport modelling (Hassan et al., 1990). Greater active layer depths in the San Juan River may be in part due to local bed texture, governed by the reach-scale morphology. Scour up to 0.3m depths at pool tailout channel margins, on an annual basis, may mean significant risk for salmon spawning survival, although more research is needed to better understand spawning depths and locations in the San Juan River. Furthermore, significant bank erosion related to overall channel instability at the three study reaches, may also lead to increased infilling of fines at pool tailouts, putting salmon spawning in the San Juan River at an even greater risk of embryo loss.

Overall, particle tracking results from this study provide important field observations to improve our understanding of sediment transport dynamics in large gravel bed rivers with complex morphology. However, due to the difficult nature of field data collection in large dynamic rivers, gaps in knowledge still exist. Future efforts should include computational flow modelling to map details of bed shear stress variation along with greater variability in seeding locations within the reach to better understand the relationship between flow, bed morphology, and subsequent tracer dispersion. Furthermore, if feasible, greater efforts would have been made by the author to map annual elevation change using digital elevation models as well as, using aerial surveys to better capture grain size sorting patterns of the gravel bars.

References

AgiSoft Metashape Professional (Version 1.7.3) (Software). 2021. Retrieved from https://www.agisoft.com/downloads/installer/

Arnaud, F., Piégay, H., Vaudor, L., Bultingaire, L., and Fantino, G. 2015. Technical specifications of low-frequency radio identification bedload tracking from field experiments: Differences in antennas, tags and operators. *Geomorphology*, **238**, 37-46. https://doi.org/10.1016/j.geomorph.2015.02.029

Arnaud, F., Piégay, H., Béal, D., Collery, P., Vaudor, L., and Rollet, A. 2017. Monitoring gravel augmentation in a large regulated river and implications for process-based restoration. *Earth Surface Processes and Landforms*, **42**, 2147-2160. https://doi.org/10.1002/esp.4161

Ashida, K., Michiue, M. 1972. Study on hydraulic resistance and bedload transport rate in alluvial streams. *Transactions, Japan Society of Civil Engineering*, **206**, 59-69.

Ashmore, P. E., & Church, M. 1998. Sediment transport and river morphology: A paradigm for study. In P. C. Klingeman, R. L. Beschta, P. D. Komar, & J. B. Bradley (Eds.), Gravel-bed rivers in the environment (pp. 115–148). Highland Ranch, CO: Water Resources Publications, LLC.

Ashmore, P., Peirce, S., & Leduc, P. 2018. Expanding the "active layer": Discussion of Church and Haschenburger (2017) What is the "active layer?" *Water Resources Research*, **53** (3), 1425-1427. https://doi.org/10.1002/2017WR022438

Ashworth, P. J., Ferguson, R. I. 1989. Size-selective entrainment of bed load in gravel bed streams. *Water Resources Research*, **25**, 627-634.

Baxter, C. V. and Hauer, F. R. 2000. Geomorphology, hyporheic exchange, and selection of spawning habitat by bull trout *(Salvellinus confluentus*). *Canadian Journal of Fisheries and Aquatic Sciences*, **57**, 1470-1481.

Beechie, T. J. 2001. Empirical predictors of annual bed load travel distance, and implications for salmonid habitat restoration and protection. *Earth Surface Processes and Landforms*, **26** , 1025-1034. https://doi.org/10.1002/esp.251

Biomark. 2021. IS1001 Antenna Control Node. Retrieved from: https://www.biomark.com/product_catalog/readers/?ProductID=157

Biron, P. M., Carver, R. B., Carré, D. M. 2012. Sediment transport and flow dynamics around a restored pool in a fish habitat rehabilitation project: field and 3D numerical model- ling experiments. *River Restoration Applications*, **28**, 926-939. https://doi.org/10.1002/rra.1488

Bradley D. N, Tucker G. E. 2012. Measuring gravel transport and dispersion in a mountain river using passive radio tracers. *Earth Surface Processes and Landforms*, **37**, 1034-1045. https://doi.org/10.1002/esp.3223

Bradley, D. N. 2017. Direct observation of heavy-tailed storage times of bed load tracer particles causing anomalous superdiffusion. *Geophysical Research Letters*, **44**, 12,227-12,235. https://doi.org/10.1002/2017GL075045

Brierley, G. J., and Hickin, E. J. 1991. Channel planform as a non-controlling factor in fluvial sedimentology: the

case of the Squamish River Floodplain, British Columbia. *Sedimentary Geology*, **75**, 67-83. https://doi.org/10.1016/0037-0738(91)90051-E

Brousse, G., Liebault, F., Arnaud-Fassetta, G. & Vasquez-Tarrio, D. 2018. Experimental bed active-layer survey with active RFID scour chains: Example of two braided rivers (the Drac and the Veneon) in the French Alps. E3S Web of Conferences, 40.

Buffington, J. M. and Montgomery, D. R. 2013. Geomorphic classification of rivers. In: Shroder, J. and Wohl, E., eds., *Treatise on Geomorphology, Vol. 9, Fluvial Geomorphology*, San Diego, CA: Academic Press, pp. 730–767.

Buffington, J. M., Woodsmith, R. D., Booth, D. B., and Montgomery, D. R. 2003. Fluvial Processes in Puget Sound Rivers and the Pacific Northwest. In D.R. Montgomery, S. Bolton, D.B. Booth, and L. Wall (Eds.) *Restoration of Puget Sound river* (pp. 46-78). University of Washington Press, Seattle.

Burge, L. M. 2005. Wandering Miramichi rivers, New Brunswick, Canada. *Geomorphology*, **69**, 253-274. https://doi.org/10.1016/j.geomorph.2005.01.010

Burt, D. W. and Palfrey, N. 2011. San Juan and Gordon River Watersheds Habitat Status Report. Retrieved from: http://a100.gov.bc.ca/pub/acat/public/viewReport.do?reportId=24086

Cassel, M., Piégay, H., Lavé, J. 2016. Effects of transport and insertion of radio frequency identification (RFID) transponders on resistance and shape of natural and synthetic pebbles: Applications for riverine and coastal bedload tracking. *Earth Surface Processes and* Landforms, **42**, 399–413. https://doi.org/10.1002/esp.3989

Chapuis, M., Bright, C. J., Hufnagel, J., and MacVicar, B. 2014. Detection ranges and uncertainty of passive radio frequency identification (RFID) transponders for sediment tracking in gravel rivers and coastal environments. *Earth Surface Processes and Landforms*, **39**, 2109-2120. https://doi.org/10.1002/esp.3620

Chapuis, M., Dufour, S., Provansal, M., Couvert, B., de Linares, M. 2015. Coupling channel evolution monitoring and RFID tracking in a large, wandering, gravel-bed river: Insights into sediment routing on geomorphic continuity through a riffle-pool sequence. *Geomorphology*, **231**, 258-269. https://doi.org/10.1016/j.geomorph.2014.12.013

Church, M. 1983. Pattern of instability in a wandering gravel bed channel. In J.D. Collinson (Ed.) *Modern and ancient fluvial systems* (pp. 169-180). International Association of Sedimentologists Special Publications, Oxford, UK.

Church, M. 2006. Bed material transport and the morphology of alluvial river channels. *The Annual Review of Earth and Planetary Science*, **34**, 325–354. https://doi.org/10.1146/annurev.earth.33.092203.122721

Church, M. and Jones, D. P. 1982. Channel bars in gravel-bed rivers. In: R.D. Hey, J.C. Bathurst and C.R. Thorne (Editors), Gravel-Bed Rivers: Fluvial Processes, Engineering and Management. Wiley, New York, 291-338.

Church, M., Rice, S. P. 2009. Form and growth of bars in a wandering gravel-bed river. *Earth Surface Processes and Landforms*, **34**, 1422–1432. https://doi.org/10.1002/esp.1831

Cienciala, P., Hassan, M. A. 2013. Linking spatial patterns of bed surface texture, bed mobility , and channel hydraulics in a mountain stream to potential substrate for small resident trout. *Geomorphology*, **197**, 96-107. https://doi.org/10.1016/j.geomorph.2013.04.041

Clayton, J. A. 2010. Local sorting, bend curvature, and particle mobility in meandering gravel bed rivers. *Water Resources Research*, **46**. https://doi.org/10.1029/2008WR007669

Desloges, J. R., and Church, M. 1987. Channel and floodplain facies in a wandering gravel-bed river. In *Recent developments in fluvial sedimentology, 39* (pp. 99-109). Society of Economic Paleontologists and Mineralogists.

DeVries, P. 1997. Riverine salmonid egg burial depths: review of published data and implications for scour studies. *Canadian Journal of Fisheries and Aquatic Sciences*, **54**, 1685-1698. https://doi.org/10.1139/F97-090

Devries, P. E. 2002. Bedload layer thickness and disturbance depth in gravel bed streams. *Journal of Hydraulic Engineering*, **128**. https://doi.org/10.1061/(ASCE)0733-9429(2002)128:11(983)

Dusterhoff, S. R., Sloat, M. R. and Ligon, F. K. 2017. The influence of coarse particle mobility on scour depth in salmonid spawning habitat. *River Resources Applications*, **33**, 1306-1314. https://doi.org/10.1002/rra.3178

East, A. E., Jenkins, K. J., Happe, P.J., Bountry, J. A., Beechie, T. J., Mastin, M. C., Sankey, J. B., Randle, T. J. 2017. Channel-planform evolution in four rivers of Olympic National Park, Washington, USA: the roles of physical drivers and trophic cascades. *Earth Surface Processes and Landforms*, **42,** 1011-1032. https://doi.org/10.1002/esp.4048

Einstein, H. A. 1937. Bedload transport as a probability problem. PhD Thesis, ETH Zurich, English translation by Sayre, W.W., 1972, In H.W. Shen (Ed.), *Sedimentation* (Appendix C). Fort Collins, Colorado: Colorado State University.

Environment and Climate Change Canada. 2021. Canadian Climate Normals 1981-2010 Station Data. Retrieved from: http://climate.weather.gc.ca/climate_normals/results_1981_2010_e.html?stnID=82&autofwd=1

Ferguson, J. I. and Wathen, S. J. 1998. Tracer-pebble movement along a concave river profile: Virtual velocity in relation to grain size and shear stress. *Water Resources Research*, **34**: 2031-2038.

Ferguson, J. I., Bloomer, D. J., Hoey, T.B., Werritty, A. 2002. Mobility of river tracer pebbles over different timescales. *Water Resources Research*, **38**. https://doi.org/10.1029/2001WR000254

Gervasi, A. A., Pasternack, G. B., East, A. E. 2021. Flooding duration and volume more important than peak discharge in explaining 18 years of gravel-cobble river change. *Earth Surface Processes and Landforms.* In Press. https://doi.org/10.1002/esp.5230

Gottesfield, A. S., Hassan, M. A., Tunnicliffe, J. F., Poirier, R.W. 2004. Sediment dispersion in fish bearing streams: the influence of floods and spawning salmon. *Journal of the American Water Resources Association*, **40**, 1071-1086.

Habersack, H., Seitz, H., & Laronne, J. B. 2008. Spatio-temporal variability of bedload transport rate: analysis and 2D modelling approach. *Geodinamica Acta*, **21**, 67-79. https://doi.org/10.3166/ga.21.67-79

Ham, D. G. 2005. Morphodynamics and sediment transport in a wandering gravel-bed channel: Fraser River, British Columbia. University of British Columbia. Retrieved from: https://open.library.ubc.ca/cIRcle/collections/ubctheses/831/items/1.0092264

Hamann, E. J., Kennedy, B. O., Whited, D. C., & Stanford, J. A. 2014. Spatial variability in spawning habitat selection by Chinook salmon (*Oncorhynnchus tshawytscha)* in a wilderness river. *River Research and Applications*, **30**, 1099-1109. https://doi.org/10.1002/rra.2704

Hanrahan, T. P. 2007. Bedform morphology of salmon spawning areas in a large gravel-bed river. *Geomorphology*, **86**, 529-536. https://doi.org/10/1016/j.geomorph.2006.09.017

Harrison, L. R., Bray, E., Overstreet, B., Legleiter, C. J., Brown, R. A., Merz., J. E., Bond, M. R…Dunne, T. 2019. Physical controls on Salmon Redd Site Selection in Restored Reaches of a Regulated Gravel-bed River. *Water Resources Research*, **55**, 8942-8966. https://doi.org/10.1029/2018WR024428

Haschenburger, J. K. 1999. A probability model of scour and fill depths in gravel-bed channels. *Water Resources Research*, **35**, 2857-2869. https://doi.org/10.1029/1999WR900153

Haschenburger, J. K. 2013. Tracing river gravels: Insights into dispersion from a long-term field experiment. *Geomorphology*, **200**, 121-131. https://doi.org/10.1016/j.geomorph.2014.03.033

Haschenburger, J. K., Church, M. 1998. Bed material transport estimated from the virtual velocity of sediment. *Earth Surface Processes and Landforms*. **23**, 791-808.

Haschenburger, J. K., Wilcock, P. R. 2003. Partial transport in a natural gravel bed channel. *Water Resources Research*, **39**. https://doi.org/10.1029/2002WR001532

Hassan, M. A. 1990. Scour, fill, and burial depth of coarse material in gravel bed streams. *Earth Surface Processes and Landforms*, **15**, 341-356.

Hassan, M. A., Bradley, D. N. 2017. Geomorphic controls on tracer particle dispersion in gravel bed rivers. D. Tsutsumi & J.B Laronne (Eds.), Gravel bed rivers: Processes and disasters (Vol. 1, pp. 159-184). Chichester, UK: John Wiley & Sons Ltd.

Hassan, M. A, Church, M., Ashworth P. J. 1992. Virtual rate and mean distance of travel of individual clasts in gravel-bed channels. *Earth Surface Processes and Landforms*, **17**, 617–627. https://doi.org/10.1002/esp.3290170607

Hassan, M. A., Church, M., Schick, A. P. 1991. Distance of movement of coarse particles in gravel bed streams. *Water Resources Research*, **27**, 503-511.

Hassan, M.A., Ferrer-Boix, Cienciala, P., and Chartrand, S. 2017. Sediment Transport and Channel Morphology: Implications for Fish habitat. Chapter in Open Channel Hydraulics, River hydraulic Structures and Fluvial Geomorphology. CRC Press.

Hassan, M. A., and Roy, A. G. 2016. Coarse particle tracking in fluvial geomorphology. In G.M. Kondolf, and H. Piégay (Eds.) *Tools in Fluvial Geomorphology. Second Edition* (pp. 306-323). Chichester, West Sussex England: Wiley Blackwell.

Hicks, M. D., Gomez, B. 2016. Sediment transport. In G.M. Kondolf, and H. Piégay (Eds.) *Tools in Fluvial Geomorphology. Second Edition* (pp. 324-355). Chichester, West Sussex England: Wiley Blackwell.

Hogan, D.L. and Luzi, D. S. 2010. Channel Geomorphology: Fluvial Forms, Processes, and Forest Management Effects. In R.G. Pike, T.E. Redding, R.D. Moore, R.D. Winkler, and K.D. Bladon (Eds.) *Compendium of*

forest hydrology and geomorphology in British Columbia, Land Management Handbook 66 (pp. 331-371). British Columbia Ministry of Forests and Range Forest Science Program.

Kasprak, A., Wheaton, J. M., Ashmore, P. E., Hensleigh, J. W., and Peirce, S. 2015. The relationship between particle travel distance and channel morphology: Results from physical models of braided rivers. *Journal of Geophysical Research: Earth Surface*, **120**, 55–74. https://doi.org/10.1002/2014JF003310

Kondolf, G. M., Piegay, H., Schmitt, L. and Montgomery, D. 2016. Geomorphic classifications of rivers and streams. In *Tools in Fluvial Geomorphology.* John Wiley & Sons Ltd.

Klosch, M., Habersack, H. 2018. Deriving formulas for an unsteady virtual velocity of bedload tracers. *Earth Surface Processes and Landforms*, **43**, 1529-1541. https://doi.org/10.1002/esp.4326

Lamarre, H., MacVicar, B., Roy, A. G. 2005. Using passive integrated transponder (PIT) tags to investigate sediment transport in gravel-bed rivers. *Journal of Sedimentary Research*, **75**, 736-741. https://doi.org/10.2110/jsr.2005.059

Lambert, C. P., & Walling, D. E. 1988. Measurement of channel storage of suspended sediment in a gravel-bed river. *Catena*, **15**, 65–80. https://doi.org/10.1016/0341-8162(88)90017-3

Lapointe, M., Eaton, B., Driscoll, S., and Latulippe, C. 2000. Modelling the probability of salmonid egg pocket scour due to floods. *Canadian Journal of Fisheries and Aquatic Sciences,* **57**, 1120-1130. https://doi.org/10.1139/f00-033.

Lenzi, M. A. 2004. Displacement and transport of marked pebbles, cobbles and boulders during floods in a steep mountain stream. *Hydrological Processes,* **18,** 1899-1914. https://doi.org/10.1002/hyp.1456

Lisenby, P. E., Croke, J., Fryirs, K. A. 2016. Geormophic effectiveness: a linear concept in a non-linear world. *Earth Surface Processes and Landforms,* **43**, 4-20. https://doi.org/10.1002/esp.4096

Leopold, L. B., Emmett, W. W., Myrick, R. M. 1966. Channel and hillslope processes in a semiarid area, New Mexico. *United States Geological Survey Professional Paper*.

Leopold, L. B. and Wolman, M. G. 1957. River Channel Patterns – Braided, Meandering, and Straight. *US Geological Survey Professional Paper,* **282**, 39–85.

Liébault F., Laronne J. B. 2008. Evaluation of bedload yield in gravel-bed rivers using scour chains and painted tracers: the case of the Esconavette Torrent (Southern French Prealps). *Geodinamica Acta*, **21**, 23–34. https://doi.org/10.3166/ga.21.23-34

Liébault, F., Bellot, H., Chapuis, M., Klotz, S., and Deschâtres, M. 2012. Bedload tracing in a high-sediment-load mountain stream. *Earth Surface Processes and Landforms*, **37**, 385–399. https://doi.org/10.1002/esp.2245

Lisle, T. E., Ikeda, H. Iseya, F. 1991. Formation of a stationary alternate bars in a steep channel with mixed size sediment: a flume experiment. *Earth Surface Processes and Landforms*, **16**, 463-469. https://doi.org/10.1002/esp.3290160507

Lorenz, J.M, and Eiler, J. H. 1989. Spawning habitat and redd characteristics of sockeye salmon in the glacial Taku River, British Columbia and Alaska. *Transactions of the American Fisheries Society*, **118**, 495-502.

MacKenzie, L. G., Eaton, B. C., Church, M. 2018. Breaking from the average: Why large grains matter in gravel-bed streams. *Earth Surface Processes and Landforms*, **43**, 3190–3196. https://doi.org/10.1002/esp.4465

MacVicar B. J, Roy A. G. 2011. Sediment mobility in a forced riffle-pool. *Geomorphology*, **125**, 445–456. https://doi.org/10.1002/esp.3395

Mao, L., Picco, L., Lenzi, M. A., Surian, N. 2016. Bed material transport estimate in large gravel-bed rivers using the virtual velocity approach. *Earth Surface Processes and Landforms*, **42**, 595-611. https://doi.org/10.1002/esp.4000

Mao, L. and Surian, N. 2009. Observations on sediment mobility in a large gravel-bed river. *Geomorphology*, **114**, 326-337. https://doi.org/10.1016/j.geomorph.2009.07.015

May, C. L., Pryor, B., Lisle, T. E., and Lang, M. 2009. Coupling hydrodynamic modelling and empirical measures of bed mobility to predict the risk of scour and fill of salmon redds in a large regulated river. *Water Resources Research*, **45**. https://doi.org/10.1029/2007WR006498

McDowell, C., Gaeuman, D., and Hassan, M. A. 2021. Linkages between bedload displacements and topographic change. *Earth Surface Processes and Landforms*, In Press. https://doi.org/10.1002/esp.5221

McKean, J., and Tonina, D. 2013. Bed stability in unconfined gravel bed mountain streams: With implications for salmon spawning viability in future climates. *Journal of Geophysical Research: Earth Surface*, **118**, 1227-1240. https://doi.org/10.1002/jgrf.20092

McQueen, R. 2019. Bed particle displacement in a wandering gravel-bed river. *Electronic Thesis and Dissertation Repository*. Retrieved from: https://ir.lib.uwo.ca/etd/6242

McQueen, R., Ashmore, P. E., Millard, T., and Goeller, N. 2021. Bed particle displacements and morphological development in a wandering gravel-bed river, **57**. https://doi.org/10.1002/essoar.10503023.2

McQueen R., Millard, T., and Goeller, N. 2016. Surface sediment characteristics of the lower San Juan River, British Columbia. Technical report. Prepared for BC Ministry of FLNRO and the San Juan Roundtable committee, 1-42.

Meredith, C. S., Budy, P and Schmidt, J. C. 2018. Scour depths at sites selected for spawning by brown trout (*Salmo trutta)* along a longitudinal gradient of a North American mountain river. *River Restoration Applications,* **34**, 786-796. https://doi.org/10.1002/rra.3321

Middleton, L., Ashmore, P., Leduc, P., and Sjogren, D. 2019. Rates of planimetric change in a proglacial gravel-bed braided river: Field measurement and physical modelling. *Earth Surface Processes and Landforms*, **44**, 752–765. https://doi.org/10.1002/esp.4528

Milan D. J. 2013. Virtual velocity of tracers in a gravel-bed river using size-based 829 competence duration. *Geomorphology*, **198**, 107–114. https://doi.org/10.1016/j.geomorph.2013.05.018

Milan D. J, Heritage G. L, and Large A. R. G. 2002. Tracer pebble entrainment and deposition loci: influence of flow character and implications for riffle-pool maintenance. In Sediment Flux to Basins: Causes, Controls and Consequences, Jones SJ, Frostick L. E (eds). *Geological Society of London Special Publications*, **191**, 133–148.

Moir, H. J., Gibbins, C. N., Soulsby, C., and Webb, J. 2004. Linking geomorphic characteristics to spatial patterns of spawning activity and discharge use by Atlantic salmon (*Salmo salar L.). Geomorphology*, **60**, 21-35. https://doi.org/10.1016/j.geomorph.2003.07.014

Moir, H. J. and Pasternack, G. B. 2008. Relationships between mesoscale morphological units, stream hydraulics and Chinook Salmon (*Oncorhynchus tshawytscha*) spawning habitat on the Lower Yuba River, California. *Geomorphology*, **100**, 527-548. https://doi.org/10.1016/j.geomorph.2008.02.001

Moir, H. J., Soulsby, C., and Youngson, A. F. 2002. Hydraulic and sedimentary controls on the availability and use of Atlantic salmon (*Salmo salar)* spawning habitat in the River Dee system, north-east Scotland. *Geomorphology*, **45**, 291-308. https://doi.org/10.1016/S0169-555X(01)00160-X

Moore, D., Spittlehouse, D. L., Whitfield, P. L., and Stahl, K. 2010. Weather and Climate. *Compendium of forest hydrology and geomorphology in British Columbia, Land Management Handbook 66* (pp. 47-84). British Columbia Ministry of Forests and Range Forest Science Program.

Montgomery, D. R., Beamer, E. M., Pess, G. R., and Quinn, T. P. 1999. Channel type and salmonid spawning distribution and abundance. *Canadian Journal of Fisheries and Aquatic Sciences*, **56**, 377-387. https://doi.org/10.1139/cjfas-56-3-377

Montgomery, D. R., Buffington, J. M., Peterson, N. P., Schuett-Hames, D., and Quinn, T. P. 1996. Stream-bed scour, egg burial depths, and the influence of salmon spawning habitat on bed surface mobility and embryo survival. *Canadian Journal of Fisheries and Aquatic Sciences*, **53**, 1061-1070. https://doi.org/10.1139/f96-028

Neill, C. R. 1971. River bed transport related to meander migration rates. *Journal of the Waterways, Harbours and Coastal Engineering Division, American Society of Civil Engineers*, **97**, 783-786.

Neill, C. R. 1973. Hydraulic and morphologic characteristics of Athabasca River near Assiniboine. Highway and River engineering Division Report, REH/73/3, Alberta Research Council, Edmonton.

Neill, C. R. 1987. Sediment balance considerations linking long-term transport and channel processes. In C.R. Thorne, J.C. Bathurst, and R.D. Hey (Eds.). *Sediment Transport in Gravel-Bed Rivers*, 225-239. John Wiley & Sons Ltd.

Nichols M. 2004. A radio frequency identification system for monitoring coarse sediment particle displacement. *Applied Engineering in Agriculture*, **20**, 783–787. https://doi.org/10.13031/2013.17727

Northwest Hydraulic Consultants Ltd. 1994. Impact of forest harvesting on terrain stability, stream channel morphology and fisheries resources of the San Juan River Watershed, Vancouver Island. Retrieved from: http://a100.gov.bc.ca/pub/acat/public/viewReport.do?reportId=23277

Oregon RFID. 2021. HDX PIT Tags. Retrieved from: https://www.oregonrfid.com/product-category/hdx-pit-tags/

Pacheedaht First Nation Treaty Information. 2020. History and villages. Retrieved from: http://pacheedahtfirstnation.com/pacheedaht-first-nation-history-and-villages/

Papangelakis, E., and Hassan, M. 2016. The role of channel morphology on the mobility and dispersion of bed sediment in a small gravel-bed stream. *Earth Surface Processes and Landforms*, **41**, 2191-2206.

Papangelakis, E., Muirhead, C., Schneider, A., and MacVicar, B. 2019. Synthetic radio frequency identification tracer stones with weighted inner ball for burial depth estimation. *Journal of Hydraulic Engineering*, **145** (12).

Papanicolaou, A.N., Moustakidis, A.G., Tsakiris, C.G., and Wilson, B. 2014. Abban, Iowa. Highway Research Board Final Report, Project TR-617.

Peirce, S. E. K. 2017. Morphological bedload transport in gravel-bed braided rivers (Electronic Thesis and Dissertation Repository, 4595). London, Ontario: Western University. Retrieved from https://ir.lib.uwo.ca/etd/4595

Peirce, S., Ashmore, P., and Leduc, P. 2018. The variability in the morphological active width: Results from physical models of gravel-bed braided rivers. *Earth Surface Processes and Landforms*, **43**, 2371-2383. https://doi.org/10.1002/esp.4400

Pfeiffer, A.M., Finnegan, N.J., and Willebring, J.K. 2017. Sediment supply controls equilibrium channel geometry in gravel rivers. *Proceedings of the National Academy of Sciences*, **114**, 3346-3351.

Phillips C. B, Martin R. L, and Jerolmack D. J. 2013. Impulse framework for unsteady flows reveals superdiffusive bed load transport. *Geophysical Research Letters*, **40**, 1328-1333. https://doi.org/10.1002/grl.50323

Pyrce, R. S., and Ashmore, P. E. 2003a. Particle path length distributions in meandering gravel-bed streams: results from physical models. *Earth Surface Processes and Landforms*, **28**, 951-966. https://doi.org/10.1002/esp.498

Pyrce, R. S., and Ashmore, P. E. 2003b. The relation between particle path length distributions and channel morphology in gravel-bed streams: A synthesis. *Geomorphology*, **56**, 167-187.

Pyrce, R. S. and Ashmore, P.E. 2005. Bedload path length and point bar development in gravel-bed river models. *Sedimentology*, **52** (4), 839-857.

Reibe, C. S., Sklar, L. S., Overstreet, B. T. and Wooster, J. W. 2014. Optimal reproduction in salmon spawning substrates linked to grain size and fish length. *Water Resources Research*, **50**, 898-918. https://doi.org/10.1002/2013WR014231

Rennie, C. D. and Millar, R. G. 2000. Spatial variability of stream bed scour and fill: a comparison of scour depth in chum salmon (*Oncorhynchus keta*) redds and adjacent bed. *Canadian Journal of Fisheries and Aquatic Sciences*, **57**, 928–938. https://doi.org/10.1139/cjfas-57-5-928

Rice, S. P., Johnson, M. F. and Reid, I. 2012. Animals and the Geomorphology of Gravel-Bed Rivers. In: Church, M, Biron, P.M. and Roy, A.G. (eds).

Rollet, A. J., MacVicar, B., Piégay, H., and Roy, A. G. 2008. A comparative study on the use of passive integrated transponders to estimate sediment transport: first results (in French). La Houille Blanche, 4, 110–116.

Shellberg, J. G., Bolton, S. M. and Montgomery, D. R. 2010. Hydrogeomorphic effects on bedload scour in bull char (*Salvenlinus confluentus)* spawning habitat, western Washington, USA. *Canadian Journal of Fisheries and Aquatic Sciences*, **67**, 626-640. https://doi.org/10.1139/F10-007

Schneider J, Hegglin R, Meier S, Turowski J, Nitsche M, and Rickenmann D. 2010. Studying sediment transport in mountain rivers by mobile and stationary RFID antennas. In *Bundesanstalt für Wasserbau*. Braunschweig: Germany.

Schneider, J. M., Turowski, J. M., Rickermann, D., Hegglin, R., Arrigo, S., Mao, L. and Kirchner, J. W. 2014. Scaling relationships between bed load volumes, transport distances, and stream power in steep mountain channels. *Journal of Geophysical Research: Earth Surface*, **119**, 533-549. https://doi.org/10.1002/2013JF002874

Shields, A. 1936. Anwendung der Aehnlickeitsmechaniuknd der Turbu-lenzforschung auf die Geschiebebewegun. Mitteilungen der Preussischen Versuchsanstalt fur Wasserbau und Schiffbau, Berlin. (English translation by W.P. Ott and J.C. van Uchelen), U.S. Department of Agriculture, Soil Conversation Service Cooperative Laboratory, California Institute of Technology, Pasadena, California.

Vasquez-Tarrio, D., Batalla, R. J. 2019. Assessing controls on the displacement of tracers in gravel-bed rivers, *Water*, **11**, 1-21. https://doi.org/10.3390/w11081598

Vasquez-Tarrio, D., Pique, G., Vericat, D., and Batalla R. J. 2021. The active layer in gravel-bed rivers: An empirical appraisal. *Earth surface processes and landforms*, **46**, 323-343. https://doi.org/10.1002/esp.5027

Vázquez-Tarrío, D., Recking, A., Liébault, F., Tal, M., and Menéndez-Duarte, R. 2019. Particle transport in gravel-bed rivers: Revisiting passive tracer data. *Earth Surface Processes and Landforms*, **44**, 112-128. https://doi.org/10.1002/esp.4484

Venditti, J. G., Nelson, P. A., Minear, J. T., Wooster, J., Dietrich, W. E. 2012. Alternate bar response to sediment supply termination. *Journal of Geophysical Research*, **117.** https://doi.org/10.1029/2011JH002254

Vericat, D., Wheaton, J. M., & Brasington, J. 2017. Revisiting the morphological approach. D. Tsutsumi, & J. B. Laronne (Eds.), Gravel bed rivers: Processes and disasters, 1, 121–158. Chichester, UK: John Wiley & Sons Ltd.

Water Survey of Canada. 2021. Monthly discharge data for San Juan River near Port Renfrew (O8HA010) [BC]. Retrieved from: https://wateroffice.ec.gc.ca/report/historical_e.html?stn=08HA010&mode=Table&type=h2oArc&results_type=historical&dataType=Monthly&parameterType=Flow&year=2017&y1Max=1&y1Min=1

Wathens, S. J. Ferguson, R. I. Hoey, T. B., Werritty, A. 1995. Unequal mobility of gravel and sand in weakly bimodal river sediments. *Water Resources Research*, **32**, 2087-2096.

Wheaton, J. M, Brasington, J., Darby, S. E., Kasprak, A., Sear, D., Vericat, D. 2013. Morphodynamic signatures of braiding mechanisms as expressed through change in sediment storage in a gravel-bed river. *Journal of Geophysical Research*, **118**, 759-779. https://doi.org/10.1002/jgrf.20060

Wilcock, P. R., Barta, A. F., Shea, C. C., Kondolf, G. M., Matthews, W. V. G., & Pitlick, J. 1996. Observations of flow and sediment entrainment on a large gravel-bed river. *Water Resources Research*, **32**, 2897-2909.

Wilkinson, S. N. Rutherford, I. D., Keller, R. J. 2008. An experimental test of whether bar instability contributes to the formation, periodicity and maintenance of pool-riffle sequences. *Earth surface processes and landforms* **33**, 1742-1756. https://doi.org/10.1002/esp.1645

Wohl, E., Lane, S. N., and Wilcox, A.C. 2015. The science and practice of river restoration. *Water Resources Research*, **51**, 5974-5997. https://doi.org/10.1002/2014wr016874

Wolman, M.G. 1954. A method of sampling coarse river-bed material. *Transactions, American Geophysical Union*, **35**, 951-956.

Wong, M. Parker, G., DeVries, P. Brown, T. M., and Burges, S. J. 2007. Experiments on dispersion of tracer stones under lower-regime plane-bed equilibrium bed load transport. *Water Resources Research*, **43**. https://doi.org/10.1029/2006WR005172

Yang, C., and Sayre, W. 1971. Stochastic model for sand dispersion. *Journal of the Hydraulics Division*, **97**, 265-288.

Appendix A – UAV Specifications

Table 0.1. Specifications for the DJI Phantom 4 Advanced camera

DJI Phantom 4 Advanced	
Model	FC6310S
Focal length	8.8
F-stop	F/5
ISO	100
Shutter	1/320
35mm focal	24

Table 0.2. GCP coordinates and precision for the Bar 6 study reach for July 2020 drone survey.

GCP	Northing	Easting	Elevation (m)	Standard Deviation Northing (m)	Standard Deviation Easting (m)	Standard Deviation Elevation (m)
6A	5382152.870	409081.196	9.262	0.0159	0.0415	0.0076
6B	5382158.387	409102.328	10.078	0.0103	0.0118	0.0010
6C	5382115.594	409108.336	10.218	0.0055	0.0072	0.0099
6D	5382083.450	409081.784	10.058	0.0210	0.0386	0.0080
6E	5382085.612	409137.080	10.142	0.0266	0.0236	0.0109
6F	5382053.594	409152.733	10.596	0.0193	0.0094	0.0009
6G	5381990.557	409075.262	9.581	0.0401	0.0131	0.0025
6H	5381997.890	409164.952	11.295	0.0222	0.0161	0.0010
6I	5381952.886	409096.171	9.726	0.0057	0.0136	0.0021
6J	5381914.019	409136.673	9.820	0.0179	0.0016	0.0016
6K	5381945.866	409173.405	13.124	0.0085	0.0135	0.0025
6L	5382033.838	409226.927	11.351	0.0380	0.0056	0.0016
6M	5382048.947	409231.466	11.394	0.0179	0.0251	0.0025
6N	5381999.620	409239.445	11.867	0.0529	0.0612	0.0143
6O	5381949.501	409206.388	12.824	0.0007	0.0214	0.0102
6P	5381968.002	409278.644	11.823	0.0189	0.0009	0.0187
6Q	5381885.608	409200.876	10.043	0.0059	0.0075	0.0053
6R	5381891.120	409238.119	9.489	0.0102	0.0203	0.0026
6S	5381923.332	409303.994	10.394	0.0116	0.0147	0.0019

Table 0.3. GCP coordinates and precision for the Bar 7 study reach for July 2020 drone survey.

GCP	Northing	Easting	Elevation (m)	Standard Deviation Northing (m)	Standard Deviation Easting (m)	Standard Deviation Elevation (m)
7A	5382137.559	408666.275	11.478	0.0020	0.0060	0.0019
7B	5382136.604	408683.817	11.779	0.0103	0.0162	0.0022
7C	5382139.788	408708.122	11.680	0.0021	0.0011	0.0024
7D	5382103.451	408724.533	10.489	0.0020	0.0048	0.0028
7E	5382136.491	408728.81	11.994	0.0033	0.0058	0.0026
7F	5382133.358	408758.438	12.005	0.0050	0.0083	0.0021
7G	5382113.725	408778.406	10.815	0.0047	0.0029	0.0028
7H	5382103.948	408815.224	10.589	0.0031	0.0127	0.0044
7I	5382120.911	408877.185	12.438	0.0115	0.0051	0.0013
7J	5382201.26	408480.532	10.535	0.0019	0.0109	0.0054
7K	5382173.478	408503.141	10.621	0.0014	0.0011	0.0003
7L	5382144.11	408528.602	10.377	0.0016	0.0014	0.0018
7M	5382177.618	408533.59	10.797	0.0019	0.0016	0.0005
7N	5382129.836	408558.714	10.680	0.0037	0.0133	0.0023
7O	5382163.866	408562.577	11.022	0.0017	0.0081	0.0013
7P	5382146.481	408596.367	11.282	0.0051	0.0077	0.0022
7Q	5382121.341	408596.508	10.568	0.0178	0.0089	0.0097
7R	5382141.493	408634.554	11.101	0.0037	0.0037	0.0042

Table 0.4. GCP coordinates and precision for the Bar 15 study reach for July 2020 drone survey.

GCP	Northing	Easting	Elevation (m)	Standard Deviation Northing (m)	Standard Deviation Easting (m)	Standard Deviation Elevation (m)
15A	5381470.873	405378.999	8.287	0.0110	0.0001	0.0057
15B	5381410.167	405389.775	5.693	0.0061	0.0049	0.0039
15C	5381431.247	405306.632	5.579	0.0004	0.0187	0.0075
15D	5381479.065	405416.980	8.461	0.0013	0.0002	0.0058
15E	5381473.760	405469.202	9.034	0.0002	0.0100	0.0003
15F	5381466.776	405516.297	8.563	0.0037	0.0108	0.0102
15G	5381406.017	405453.286	5.878	0.0001	0.0119	0.0029
15H	5381479.116	405562.691	9.071	0.0053	0.0102	0.0108
15I	5381489.271	405615.813	10.049	0.0044	0.0068	0.0045
15J	5381576.665	405731.070	5.993	0.0056	0.0070	0.0053
15K	5381525.421	405672.230	8.122	0.0047	0.0067	0.0026
15L	5381407.475	405512.141	5.919	0.0008	0.0085	0.0012
15M	5381417.952	405570.874	5.627	0.0052	0.0011	0.0022
15N	5381444.711	405629.211	5.620	0.0027	0.0083	0.0047
15O	5381484.187	405688.488	5.605	0.0143	0.0021	0.0015
15P	5381464.528	405250.445	5.641	0.0087	0.0210	0.0124
15Q	5381475.911	405326.791	6.246	0.0107	0.0096	0.0124

Curriculum Vita

Name:	Meghan Sauro
Post-secondary Education and Degrees:	University of Western Ontario London, Ontario, Canada 2014-2019 B.Sc Honours Specialization in Environmental Science
	University of Western Ontario London, Ontario, Canada 2019-2021 M.Sc
Honours and Awards:	Michael Troughton Bursary 2019-2020
	Edward G. Pleva Fellowship Award 2019-2020
	Laurene Paterson Estate Scholarship 2018-2019
	Dean's Honour List 2017-2018, 2018-2019
Related Work Experience:	Research Geomorphologist Assistant B.C Ministry of Forests, Lands, Natural Resources and Rural Development 2019-2021
	Teaching Assistant University of Western Ontario 2019-2020
Publications	Marejka, E., **Sauro, M.,** Kroeze, S. (2020). Why is it Vital to Conserve Rivers? *Alternatives Journal*